Numerical study of wind-tide interaction effects on internal wave generation

by

Sorush Omidvar

(Under the Direction of C Brock Woodson)

Abstract

The coastal ocean is a complex region affected by several processes with various spatiotemporal scales such as tidal flows, internal waves (IW)s, along-shore, and cross-shore (XS) winds, buoyancy-driven flows, and surface waves. IWs have important implications for pollutant dispersal, nutrient supply, energy budgets, and ecosystem impacts of climate change in the coastal zone. IWs are generated by the acceleration of the tidal flows over sloped bathymetry, which results in a phase lag between pressure and velocity and effectively converts tidal energy from barotropic to baroclinic. This energy conversion propagates in the system in the form of density perturbations or IWs. The generation of IWs over the continental shelf and their advection into nearshore areas have been studied extensively. Moreover, the modification of coastal dynamics by sea breeze (XS transport by XS wind in the inner-shelf) and regional-scale (upwelling/downwelling by alongshore wind) have received considerable attention in the past few decades. However, the generation of IWs in the nearshore and

how such a generation is affected by winds and other tidal components have received much less attention, even though this is the region where IWs often have the highest impact. In addition, the coupling of XS wind and tidal currents in the inner-shelf where the XS wind is more effective in deriving XS transport (in comparison to the alongshore wind) has been neglected. Therefore, in this dissertation, I 1) develop a robust mathematical formulation to calculate the barotropic to baroclinic energy conversion, which filters the residual conversion, 2) examine the interaction of tidal flows with various periods (i.e., diurnal and semi-diurnal) and parameters that affect such interaction, and 3) elucidate the role of the wind in the energy conversion process for shallow coastal regions.

INDEX WORDS: Internal Waves, Barotropic to Baroclinic Energy Conversion, Coastal Ocean, Numerical Modeling, SUNTANS

Numerical study of wind-tide interaction effects on internal wave generation

by

Sorush Omidvar

B.Sc., Amirkabir University of Technology, Tehran, Iran, 2013

A Dissertation Submitted to the Graduate Faculty
of The University of Georgia in Partial Fulfillment
of the Requirements for the Degree

Doctor of Philosophy

Athens, Georgia

2020

Numerical study of wind-tide interaction effects on internal wave generation

by

Sorush Omidvar

Major Professor:	C Brock Woodson
Committee:	E.W. Bill Tollner David E Stooksbury Renato Castelao Daniela Di Iorio

Electronic Version Approved:

Ron Walcott
Interim Dean of The Graduate School
The University of Georgia
May 2020

Dedication

به نام خداوند جان و خرد — کزین برتر اندیشه برنگذرد
خداوند نام و خداوند جای — خداوند روزی ده رهنمای
خداوند کیوان و گردان سپهر — فروزنده ماه و ناهید و مهر
ز نام و نشان و گمان برترست — نگارنده ی بر شده پیکرست

تقدیم به پدرم رود خروشانم، مادرم شمع سوزانم، همسرم آب روانم و برادر راه جویانم.

تقدیم به پدری که تکیه گاهم بود. تقدیم به پدری که همواره کوشید تا نداشته هایش داشته های من باشد. پدری که هر روز مرا به دبستان برد تا بال پرواز بگشایم. کسی که از حراج اموالش برای اعتلای فرزندانش دریغ نکرد. پدری که بدون او هرگز نمی توانستم به زبان خارجه تسلط پیدا کنم. کسی که معنی کلمه "نمی شود" را در هم می شکست. مردی که هیچ گاه در زندگی کمر خم نکرد ولی در هنگام کوچ من سخت گریست. پدری که با حضورش همه ی مشکلات چاره می شد و خواب راحتی بر چشم من می نشست. ای کاش بودی و پر گرفتن مرا از نزدیک می دیدی. تقدیم به پدرم که فخرش بودم و فخرم بود.

این گوهر گم گشته به دنیا پدرم بود — محبوب همه یار همه تاج سرم بود
هر جا که ز من نام و نشانی طلبیدند — آوازه همه نامش سند معتبرم بود
آن کس که مرا روح و روان بود پدر بود — آن کس که مرا راحت جان بود پدرم بود
افسوس که رفت از سرم آن سایه رحمت — آن کس که برایم نگران بود پدرم بود

تقدیم به مادری که پناهم است. تقدیم به مادری که نه تنها الفبای فارسی بلکه الفبای زندگی را به من آموخت. مادری که پرستار شب های تار و بی ستاره ی کودکیم بود. مادری که کودک به بر از طبیبی به طبیب دیگر در پی چاره بود. مادری که درد من مرگ او بود. زنی

که همچون شمع سوخت و بر زندگی من تابید تا من بالا و بالاتر روم. مادری که فارغ از داشته ها و نداشته هایم به من عشق ورزید و عشق را برایم معنی کرد.

گویند مرا چو زاد مادر — پستان به دهان گرفتن آموخت
شب‌ها بر گاهواره من — بیدار نشست و خفتن آموخت
لبخند نهاد بر لب من — بر غنچه گل شکفتن آموخت
دستم بگرفت و پا به پا برد — تا شیوهٔ راه‌رفتن آموخت
یک حرف و دو حرف بر زبانم — الفاظ نهاد و گفتن آموخت
پس هستی من ز هستی اوست — تا هستم و هست دارمش دوست

تقدیم به همسری که روانم است. تقدیم به همسری که با صبوری بر ناملایمات زندگی لبخند می زند. همسری که در این مسیر پر پیچ و خم همواره با من هم داستان بود و با حضور گرمابخشش مرا آرام می نمود. زنی که چراغ خانه ام را با عشق خود بر افروخت و عطر مهر خود را در خانه بر افشاند. همسری که با حمایت عاطفی و معنویش این دفتر را به سرانجام رساند.

با تو بودن همیشه پرمعناست — بی تو روحم گرفته و تنهاست
با تو یک کاسه آب یک دریاست — بی تو دردم به وسعت صحراست
با تو بودن همیشه پرمعناست — با تو آسان هزار کار خطیر
با تو ممکن جهاد با تقدیر — بی تو با غم برهنه همچون کویر
با تو یک غنچه دشتی از گلهاست — با تو بودن همیشه پرمعناست
ای تو! تعریف ناپذیرترین — بی تو من کوچک و حقیرترین

تقدیم به برادری که هم رای من است. همان وی غم گسار من است. تقدیم به مردی که در غیاب پدر و نبود برادر کمر بر یاری مادر بست. دانشجویی که پای در راه علم نهاد و در آموختن بجنبید راست.

بدو گفت شاه از هنرها چه به ؟ — که گردد بدو مرد جوینده مه
چنین داد پاسخ که دانش به است — که داننده بر مهتران بر مه است
بیاموز دانش تو تا ایدری — که آنجا ز دانش همه برخری
که دانش بشب پاسبان من است — خرد تاج پیدار جان من است

Acknowledgments

I would like to thank my advisor, Dr. C Brock Woodson, for his support, patience, knowledge, and flexibility. My relationship with Dr. Woodson began by knocking on his door as a total stranger and then leaving 30 minutes later as one of his graduate students back in 2014. His support quenched my thirst for learning as he navigated me through an extensive number of courses to learn more about physical oceanography and academic education. His patience and understanding of my emotional and physical distress allowed me to recover from multiple health issues, the grief of losing my father, and being able to marry the love of my life. Dr. Woodson is brilliant and he willingly shared his knowledge to propel me through the arduous task of modeling and data analysis. His flexibility gave me the opportunity to expand my research into directions that allured me.

I would like to express my gratitude to many friends, especially Joel Stiling, and Jeff and Caroline Thompson who are my family in Athens. They shared their lives, helping me feel less like a lonely stranger. They always supported me in every step, particularly during my socio-medical hardship and crisis.

This work was funded by NSF-OCE grant 1416837 to C. Brock Woodson. Any opinions, findings, conclusions, or recommendations expressed in this material are those

of the authors and do not necessarily reflect the view of the NSF.

This study was supported by resources from the Georgia Advanced Computing Resource Center, a partnership between the University of Georgia's Office of the Vice President for Research and Office of the Vice President for Information Technology.

Contents

Acknowledgments **viii**

1 Introduction and Motivation **1**

1.1 Motivation 2

1.2 Research Questions 3

1.3 Hypotheses 4

2 Background and Related Work **6**

2.1 Internal Wave Records & Generation Mechanisms 7

2.2 IW Characteristics 10

2.3 IW Physical Importance 22

2.4 IW Chemical Importance 31

2.5 Biological Importance 33

2.6 Wind Effects on Coastal Dynamics 37

2.7 Monterey Bay 45

3 Theoretical Framework **51**

3.1 Governing Equations & Operators 54
3.2 The hydrostatic (LSY) method 55
3.3 Conversion Rate Using CBD Method 57
3.4 Conversion Rate Using TVBD Method 64

4 Conversion Rate Formulation **67**
4.1 Introduction 68
4.2 Theoretical framework 72
4.3 Numerical Setup 78
4.4 Results and Interpretation 84
4.5 Summary, Conclusion and Future Work 94

5 Tide-Tide Interaction **97**
5.1 Introduction 98
5.2 Theoretical framework 101
5.3 Numerical Setup 105
5.4 Results and Interpretation 111
5.5 Conclusion & Future Work 124
5.6 Acknowledgments 126

6 Wind-Tide Interaction **127**
6.1 Introduction 128
6.2 Theoretical framework 130
6.3 Numerical Setup 132
6.4 Results and Interpretation 136

6.5 Conclusion & Future Work 154
6.6 Acknowledgments 156

7 Conclusion & Future Work **157**

7.1 Contributions 158
7.2 Future Work 161

List of Figures

2.1 The schematic of linear IW propagation in a two-layered system adopted from Woodson [2018]. 7

2.2 The schematic of linear surface wave where Panels a to c show deep, intermediate and shallow water cases Kundu et al. [2012]. 12

2.3 The schematic of phase and group velocity directions for IWs which is adopted from Cushman-Roisin and Beckers [2011]. 14

2.4 The schematic effects of steepness parameter(β_1) and tidal excursion (β_2) on IWs adopted from [St. Laurent and Garrett, 2002] . . 18

2.5 The schematic of wave evolution as it approaches the shoreline adopted from [Woodson, 2018] 20

2.6 Kelvin-Helmholtz instability due to a sheared flow in the atmosphere 22

2.7 Turbulent kinetic energy cascade for different eddy sizes 25

2.8 The top panel is showing the density while the lower one provides the ϵ [Palmer et al., 2015] 28

2.9 The left column shows the backscatter which is a proxy for suspended sediment and the right one provides the TKE dissipation rate (ϵ) [Moum et al., 2007] 29
2.10 The panels show Ri^{-1} (the white counter shows the critical Richardson number of 0.25), ϵ and back-scatter from top to bottom [Shroyer et al., 2010] 30
2.11 The top panel gives the ϵ while the shear velocity squared is shown in the lower panel for the period 1 from Inall et al. [2000] 31
2.12 The schematic of internal bore (panel A to C) and shoreward return flow of the surface layer (panel E to F) adopted from Pineda [1994] for a two-layered system. 35
2.13 The schematic of Ekman surface layer spiral in the northern hemisphere 38
2.14 The schematic of Ekman upwelling and downwelling for AS wind . 39
2.15 The XS velocity at the Chesapeake Bay for a stratified (a,b) and unstratified (c) system [Lentz, 2002]. 40
2.16 The panels show density, near-surface transport and near-bottom XS transport respectively for a profile 26-meters deep at the Chesapeake Bay [Lentz, 2002]. 41
2.17 The salinity profile during a weak downwelling (top panel) and strong upwelling (bottom panel) where the isopycnal became vertical and turbulent mixing is promoted (low Ri number) [Lentz and Largier, 2006] 42

2.18 The efficiency of the AS wind in deriving XS transport for different studies reviewed by Fewings et al. [2008] 44
2.19 The schematic of XS transport in inner to mid-shelf Fewings et al. [2008]. 45
2.20 a) The topography of Monterey bay region [Walter et al., 2012] with the local diurnal sea breeze at Hopkins Marine Station (red arrow) based on [Woodson, 2013]. b) The bathymetry profile is provided along the blue dots [Walter et al., 2012]. 46
2.21 Sea surface temperature and chlorophyll concentration in Monterey Bay [Zhang et al., 2016]. 47
2.22 M-2 surface amplitude (colors) and phase (black contours) are shown in a, while b shows the depth-averaged M_2 tidal current ellipses [Carter, 2010]. 49

3.1 Global energy budget adopted from Munk and Wunsch [1998] . . 53

4.1 Data at X=99.5 km and Z=-50.8 m for a system with flat bathymetry (Case 1). Rows show tidal height, background density, density perturbation, barotropic vertical velocity, barotropic conversion rate and conversion rate from top to bottom. 76
4.2 Ideal ridge bathymetry map (case 4) is shown in a with the maximum and minimum depth of 3000 and 300 meters. The transects at X= 300 km and Y= 50 km are shown in panel b and c respectively. 79

4.3 Background density and Brunt-Vaisala frequency at the beginning of last 3 tidal cycle for a) shallow (cases 1 and 2) and b) deep (cases 3 and 4) 81

4.4 Schematic IW propagation and reflection (dashed lines) from the generation site in a system with subcritical bathymetry 83

4.5 Vertical velocity at time t = 0.4 cycle for a) shallow (case 2) and b) deep (case 3). Green dot show the generation site (Fig 4.6) and purple is a sample of reflection point. 84

4.6 Left panel shows the data at X=130.7 km and Z=-37.4 m for case 2 and right panel is for case 3 at X=330.9 km and Z=-524 m (green dots in Fig 4.5). Rows show background density, perturbation density, barotropic vertical velocity, barotropic conversion rate and conversion rate from top to bottom 85

4.7 Panel a and b show the time-averaged conversion rate ($\langle C \rangle$) using KF and TVBD at the transect Y=50 km. The time-averaged depth-integrated conversion rate ($\langle \bar{C} \rangle$) at the transect Y=50 km for both method can be seen in panel c; while, the components of TVBD are shown in panel d. The time-averaged depth-integrated conversion rate for the whole domain can be seen in panels e and f using KF and TVBD respectively. Bathymetry contours are spaced at -300, -500, -1000, -2000 and 2900 meters in panels e and f. 86

4.8 Data at a IW reflection point. Left panel shows the data at X=89.9 km and Z=-17.8 m for case 2 and right panel is for case 3 at X=203.9 km and Z=-104.8 m (purple dots in Fig 4.5). Rows show background density, perturbation density, vertical velocity (W, w' and $\frac{\partial \delta}{\partial t}$) and conversion rate from top to bottom 87

4.9 Time-averaged conversion rate ($\langle C \rangle$) for case 2 (left column) and case 3 (right column). Top row shows the result of KF method and bottom row is for TVBD. 88

4.10 Time-averaged depth-integrated conversion rate ($\langle \bar{C} \rangle$) for KF, LSY and TVBD methods for case 2 (left column) and case 3 (right column). The top row shows the comparison between two methods and bottom row provides more details about the two terms of TVBD method as well as the LSY method results discarding the bathymetry gradient H_x. 89

4.11 Time-averaged horizontal BT velocity $\langle U \rangle$ (top row) and time-averaged vertical BT velocity $\langle W \rangle$ (bottom row) for case 2 (left column) and case 3 (right column). Reflection points can be seen as the intensification of W in bottom panel 92

5.1 Sea surface height (η), density perturbation (ρ'), BT vertical velocity (W), and conversion rate (C) are shown at $x = 44.5$ km and $z = -9.5$ m for the last four tidal cycle of a system perturbed by M_2 tide. The phase lag between ρ' and W is creating positive net conversion rate. 105

5.2 a) Monterey Bay bathymetry map with contours at 25, 50, 75, 100, 250, 750 and 1000 meters. b) The southern Monterey Bay with the contours at 5, 10, 25, 50 and 75 meters deep, c) The bathymetry profile and its slope along the orange arrow in the panel b which is taken from Walter et al. [2012]. The topography presented in panel c can be used as a representative for the southern Monterey Bay area. d) NOAA tidal gauge 9413450 sea surface height during June 2017. 108

5.3 a) An idealized density stratification for a highly stratified system during the summer with $N_{max} = 0.04$ in the southern Monterey Bay with the pycnocline depth of 5 m. Time-averaged conversion rate $\langle C \rangle$ and time-averaged depth-integrated conversion rate $\langle \overline{C} \rangle$ are shown for one of the cases in panel b and c respectively. . . . 109

5.4 The effects of pycnocline depth on location and the intensity of maximum conversion rate for cases perturbed by M_2K_1 tidal currents. Panel a shows the topography of the nearshore area, while b to h show the $\langle C \rangle$ of the orange box. The time-averaged conversion rate $\langle C \rangle$ for cases with various pycnocline depth of 5, 7.5, 10, 12.5, 15, 17.5 and 20 meters are shown in panels b to h respectively. . . 113

5.5 Sea surface, BT vertical velocity, density perturbation and conversion rate time-series are shown in panel a to d for cases perturbed by M_2 tides with pycnocline at various depths. Panels e, f and g show the vertical structure of BT vertical velocity, density perturbation and conversion rate respectively. All data are reported at the maximum location of $\widehat{\langle \overline{C} \rangle}$ where x =44.688, 44.628, 44.628, 44.588, 44.508 and 44.448 km, z =4.5, 7, 12.5, 13.75, 15 and 19.5 meters and the water column depth is 9.75, 12.5, 12.5, 14.75, 19.5, and 23.5 meters. 115

5.6 The relation between Γ_1, Γ_2 and pycnocline for cases perturbed by M_2 and K_1 is shown in panel a and b respectively. The M_2K_1 data is not plotted as ω and U_0 is not well defined in Γ_1, Γ_2 for a case perturbed by various tidal constituents. The panel a has two different vertical axis to accommodate the high range for K_1 (ω_{K1} is close to f which causes a significant amplification of Γ_1, while its behavior is similar to M_2). The initial phases of the M_2 and K_1 tidal currents are 90° and 144°. The bathymetry slope at the reported locations is increasing with deepening of the pycnocline as 0.0275, 0.0500, 0.0500, 0.0550, 0.0625 and 0.0675 for 5, 7.5, 10, 12.5, 15 and 20 respectively. 117

5.7 The effects of pycnocline depth on $\widehat{\langle \overline{C} \rangle}$ for cases perturbed by M_2K_1, M_2 and K_1. The initial phases of the M_2 and K_1 tidal currents are 90° and 144°. The contribution of M_2, K_1 and NT respective to M_2K_1 is shown in percentage in panel b. 118

5.8 The Fourier decomposition of C at its the maximum location is shown for M_2K_1, K_1 and M_2 cases in the panel a, b and c respectively. Each panel shows the data for various pycnocline depth (5, 7.5, 10, 12.5, 15, 17.5 and 20 meters). The period peaks in the Fourier represent $T_{K1} = 23.9$, $T_{K1}/2 = 11.95$ and $T_{K1}/3 = 7.97$; $T_{M2} = 12.4$, $T_{M2}/2 = 6.2$ and $T_{M2}/3 = 4.13$ for panels b and c. For Panel a, the primary and secondary periods are $T_{M2}/2 = 6.2$, $T_{M2}/3 = 4.13$, $T_{K1} * T_{M2}/(T_{K1} - T_{M2}) = 25.8$ as well as some of the periods which are close together and the the decomposition did not separate them out clearly such as $T_{K1} * T_{M2}/(T_{K1} + T_{M2}) = 8.17$ and $T_{K1} = 23.9$ as well as $T_{M2} = 12.4$ and $T_{K1}/2 = 11.95$. There is an extra peak (4.92 hr) for $M2K1$ which is result of third order (in addition to primary and secondary) interaction between 8.17 and 12.4 (8.17*12.4)/(8.17+12.4). 121

5.9 The time-series of various attributes (sea surface level, BT vertical velocity, density perturbation, and conversion rate) for different tidal constituents (M_2K_1, M_2 and K_1) are provided in panels a to d, while e, f and g are showing the vertical structure (BT vertical velocity, density perturbation and conversion rate) at the location of maximum conversion rate (x=44.648 km, z=9.75 meters and $d = 11.5$ meters) at different times (the blue, red and yellow stars denotes t =416.8, 410.1 and 416.8 hr). 123

5.10 The relation between $\widehat{\overline{\langle C \rangle}}$ and the phase lag for cases with pycnocline at 7.5, 12.5 and 17.5 meters deep which are perturbed by M_2K_1 tidal current where the $\overbrace{M_2, K_1} = Phase_{K1} - Phase_{M2}$ varies from $-54°$ to $124°$. 124

6.1 The figure provides the wind record for HMS during June of 2017. Panels show the oscillation amplitude at the primary frequency (a), 10-minute wind polar histogram (b) and XS-AS wind constituents (c). 135

6.2 The figure provides the horizontal velocity perturbation due to the presence of IWs and XS wind. The left vertical axis in panel a shows the wind speed, while the right one provides the sea surface height. Panels b-c and d-e provide the vertical structure at $x = 37.058$ km (offshore) and $x = 44.668$ km (at the slope) respectively. The system responses during the ebb ($t = 402.8$ hr) and flood ($t = 410$ hr) are shown in b-d and c-e. 138

6.3 The time-series and vertical structure of the nearshore area are shown for cases perturbed only by wind (pycnocline=7.5 meters). The panels a to e are showing the time-series at $x = 44.668$ km and $z = -9$ meters. Panels f to h are showing the vertical structure of density perturbation, horizontal velocity perturbation and ten-times of horizontal mean velocity (dashed lines in panel g) as well as the vertical velocity at various time which are shown with blue, red and yellow stars in panel a. 139

6.4 Similar to Fig 6.3 where $z = -6$ meters and the model is perturbed by M_2 tide and wind (blue, yellow and red curves) as well as only by tide (purple). The wind initial phases are shown in the top panel. Panel f to h shows the vertical structure at the time= 413.25 (blue), 415.25 (yellow) and 417.25 hours (red) when the wind speed is at maximum (the purple corresponds to 415.33 hours) which is shown in panel a by stars. 140

6.5 Horizontal (left panels) and vertical velocity (right panels) for a case perturbed only by the wind with the pycnocline depth of 7.5 meters. The timing of the panels are 379.25, 385.33, 387.42 and 391.33 hours from top to bottom respectively. 141

6.6 Similar to Fig 6.4 where $z = -9.25$ meters and the model is perturbed by K_1 tide and wind (blue, yellow and red curves) as well as only by tide (purple). Panel f to h shows the vertical structure at the time= 40.17 (blue), 413.17 (yellow) and 417.17 hours (red) when the wind speed is at maximum (the purple corresponds to 409.75 hours) which is shown in panel a by stars. 142

6.7 The contribution of XS wind in XS-integrated depth-integrated tidal-averaged conversion rate, $\widehat{\langle \overline{C} \rangle}$, is shown for various cases as the difference with the baseline values (the value printed inside each panel). The columns show the $\widehat{\langle \overline{C} \rangle}$ for M_2K_1, K_1 and M_2 from left to right, while the rows provides the details for pycnocline at 7.5, 12.5 and 17.5 meters. The severe and moderate wind (6 and 3 $m.s^{-1}$) are shown with red and blue curves. The initial phases of M_2 and K_1 tidal currents are 90° and 36°. 145

6.8 Similar to Fig 6.7 where the sensitivity of conversion on wind-tide phase lag is evaluated with a hypothetical tidal constituent with 20 hours period for cases with pycnocline depth of 12.5 meters. The M_2 and K_1 data are plotted in a normalized format (the whole phase lag span is normalized between 0 to 1) for the sake of comparison. 146

6.9 The $\langle C \rangle$ structure in the nearshore area is shown for cases perturbed by M_2K_1 tide and XS wind (with a wind speed of 0, 1.5, 3, 4.5 and 6 $m.s^{-1}$) with pycnocline at 5, 7.5, 10, 12.5, 15, 17.5 and 20 meters deep. The total conversion $\widehat{\langle \overline{C} \rangle}$ values are shown inside each panel. 148

6.10 The wind speed, BT vertical and horizontal velocities, BC horizontal velocity, density perturbation and conversion rate time-series are shown in the nearshore area for cases perturbed by M_2K_1 tide and XS wind (with a wind speed range of 0, 1.5, 3, 4.5 and 6 $m.s^{-1}$) with pycnocline at 12.5 meters deep. The initial phases of M_2, K_1 and wind are 90°, 144° and 157°. 150

6.11 The $\widehat{\langle \overline{C} \rangle}$ values for cases perturbed by K_1 (a), M_2 (b) and M_2K_1 (c) as a function pycnocline depth are shown above. The value of nonlinear tide-tide and tide-wind interactions are shown in green bars and light blue error bar (the center is shown with dot) respectively. The initial M_2 and K_1 phases are 90° and 36°. 152

6.12 The total conversion in the domain as a function of offshore distance is shown in panel a for various cases perturbed by K_1 tidal currents and 6 $m.s^{-1}$ wind with pycnocline at 7.5 meters. Panel b and c show the minimum Richardson number (during the whole process time) for the $\overbrace{\text{wind, tide}} = -48°$ and 72° which has a positive and negative total conversion rate (panel a) respectively. 154

List of Tables

2.1 Main tidal constituents near in the northern (southern) part of Monterey Bay [Petruncio et al., 1998] 49

4.1 Case study details show domain length (L), horizontal and temporal resolution (ΔX and Δt), number of vertical layers (N_k), minimum and maximum layer thickens (Δz_{min} and Δz_{max}), minimum and maximum bathymetry depth (h_0 and H_0), bathymetric shape constants (L_s, X_{mid}), tidal current velocity at the ocean-side boundary (U_0), maximum of the tidal height (η_{max}), sponge layer constants (L_0, L_1, α_0, α_1), horizontal and vertical eddy viscosity (ν_H and ν_V) 80

4.2 Variables and symbols used in the paper 96

Chapter 1

INTRODUCTION AND MOTIVATION

To answer my research questions and test hypotheses, I organized this dissertation as follows. 1) I start by introducing the dissertation motivation, stating the research questions, and discussing the hypothesis briefly. 2) Subsequently, I provide details on the internal wave characteristics, generation mechanisms, mathematical solutions, related dimensionless parameters, and biophysical importance. I continue this chapter by reviewing the impacts of alongshore and cross-shore wind in the coastal regions as well as covering the coastal dynamics of my focal area, Southern Monterey Bay. 3) Next, I review previous studies and current methods to calculate and analyze the energy budget with the focus of energy conversion. 4) I optimize the energy conversion calculation based upon the present formulation to analyze the internal wave generation and energy budget through time more

effectively by filtering the residual conversion induced by barotropic tidal heaving (chapter 4). 5) I explain the interaction of two tidal components (with different periods) and the role of environmental parameters which affect such energy conversion, including the pycnocline depth and their initial phase lag (chapter 5). 6) I examine the cross-shore wind impacts on the conversion rate and its sensitivity to environmental parameters such as pycnocline depth, wind-tide phase lag, and wind speed (chapter 6). 7) I conclude this dissertation by summarizing the problems and highlighting my findings on the efficiency of a new formulation for conversion rate calculation as well as wind-tide and tide-tide energy conversion.

1.1 Motivation

Internal waves are ubiquitous features of the ocean, which affect the biophysical dynamics of coastal seas; therefore, studying internal wave generation and the environmental parameters which affect them are of importance for a variety of fields including oceanography, ecology, and engineering. The generation of internal waves over the continental shelf can be quantified as barotropic to baroclinic energy conversion, which advects in the form of density perturbations in a density stratified media. The generation of internal waves has received considerable attention in the last century. However, under current formulations, there is an ambiguity about the presence of negative conversion away from the generation sites. The presence of such negative conversion can be simply due to not partitioning the baroclinic and barotropic accurately.

Studying the role and interaction of environmental parameters in the energy conversion process is a tortuous task that is still developing and unfolding. Although recent studies have addressed the interactions of semidiurnal tidal flow with the diurnal cross-shore wind-induced flow (by alongshore wind) in the mid-shelf regions, such a mechanism is not an efficient way to derive cross-shore flows in the inner-shelf. In inner-shelf regions, the cross-shore flow is governed by cross-shore wind rather than alongshore wind as the surface and bottom boundary layers interact with each other. Therefore, there is a need to study wind-tide interactions in such locations. Moreover, the interaction of tidal flows with different periods, and its effects on the conversion rate is of interest.

1.2 Research Questions

In this dissertation, I address the three main questions:

- Is the negative conversion (calculated under current formulations) away from the generation sites, an actual baroclinic to baroclinic energy conversion through pressure-work? Or is it the residual constituent of the analytical framework? If so, what is inducing negative conversion? And how can it be removed to allow a more effective study of energy conversion through time?

- The semidiurnal tidal flow creates significant conversion; however, the role of other tidal constituents (i.e., diurnal) in this process is generally dismissed. What is the contribution of K_1 tidal flow in converting barotropic to baroclinic energy? Does the depth of pycnocline affect the energy conversion in

the nearshore area? How do K_1 and M_2 interact with each other? Does linear superposition hold for M_2K_1 interaction?

- Prominent cross-shore diurnal sea breezes are common in coastal regions during the upwelling season. Does the wind affect the energy conversion process in the nearshore area? Does the wind-tide phase lag effect barotropic to baroclinic energy conversion? What are the roles of other environmental factors such as pycnocline depth and wind speed in such a conversion?

1.3 Hypotheses

I hypothesized that it is possible to filter the negative conversion away from generation sites. Negative conversion is generated due to the interaction of internal waves with barotropic tidal heaving (barotropic vertical movements of isopycnals due to surface tides), and it is compensated by the extra positive conversion on the slope. To avoid such interaction and find the net conversion, the barotropic tidal heaving should be removed from the background density by using a time-variant background density (instead of background density, which is constant with time), which discards the barotropic tidal heaving. This allows a more effective analysis of energy conversion through time.

Current studies might underestimate the conversion as they only consider the semidiurnal constituent. Therefore, by including an additional tidal component (K_1), I analyze the conversion value in the nearshore region to examine how much of the conversion is underestimated. I expect to see the validity of linear

superposition for the interaction of M_2 and K_1 as the internal tides observed in the southern Monterey bay are linear. The environmental parameters affect the dimensionless numbers such as tidal excursion and internal wave steepness, which govern the internal wave characteristics; therefore, the conversion is expected to be a function of these numbers rather than be a function of pycnocline depth directly.

I speculate that the presence of cross-shore wind can promote energy conversion in the nearshore area. The role of cross-shore wind in cross-shore transport and flow is more prominent in comparison to the alongshore wind. Such a process intensifies the shear velocity throughout the water column, which results in promoting the density perturbations. Therefore, the intensification of conversion is expected in the presence of cross-shore wind.

Chapter 2

BACKGROUND AND RELATED WORK

IWs, disturbances that propagate through density-stratified media (Fig 2.1), are common features of the coastal ocean where they can affect biological, chemical and physical dynamics. Due to the critical role of IWs in the Earth energy budget and extensive records of their presence, they have received a significant amount of attention with considerable focus on their generation. IW generation generally occurs due to tidal flows over sloped topography and is often characterized as a barotropic-baroclinic conversion rate. The focus of this dissertation is on determining BT-BC conversion rates in shallow water and examining how tides, winds and stratification affect their generation with a specific emphasis on the nearshore region of Monterey Bay. In this chapter, we start with IW characteristics and generation mechanisms and then outline their bio-physical importance. I finish

the chapter with the review of Monterey Bay dynamics as an active site for IW generation.

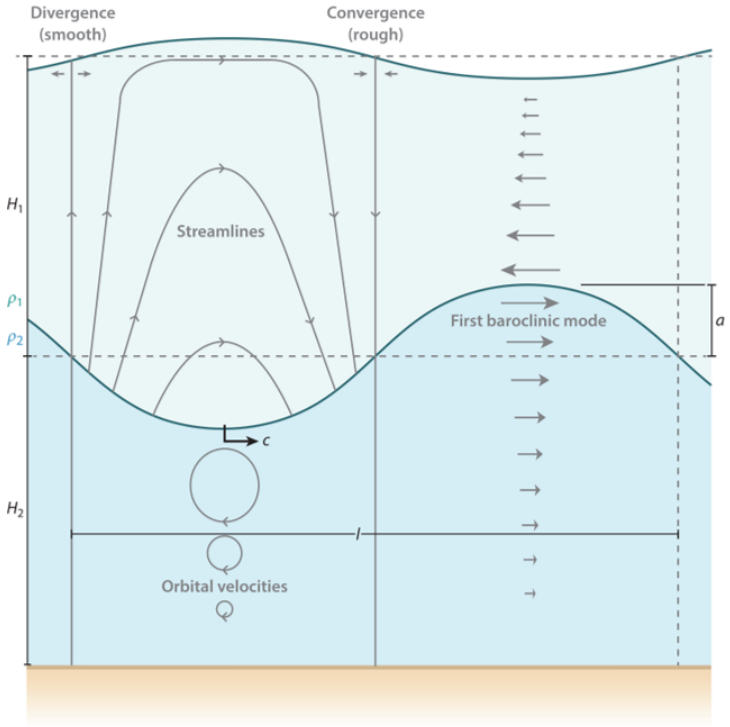

Figure 2.1: The schematic of linear IW propagation in a two-layered system adopted from Woodson [2018].

2.1 Internal Wave Records & Generation Mechanisms

IWs which are a form of gravity wave, have been documented and observed for many years. The first observation of IWs in the coastal ocean was made in 1897 by Fridtjof Nansen in the Arctic ocean [Nansen, 1905]. Nansen named and described

the IWs as "Dead Water" in his exploratory journey as his ship was brought to stop by IWs. Later, Ekman was able to explain and address this mysterious phenomenon analytically. Ekman clarified that the resistance created in the dead water zone is caused by the generated IWs, which are induced by vessel perturbations at the ocean surface in a highly stratified system [Nansen, 1905]. Such resistance is due to the counter-flow created by IWs on the top of IW crests, as observed in Fig 2.1.

Internal tides (IT), IWs with tidal frequency, were initially believed not to exist [Defant, 1932]. However, Defant did not take into account the rotation of the Earth. Haurwitz [1950] corrected Defant's work by adding the Coriolis effect into the equations of motion. Subsequently, several studies were published to characterize IW behaviors through simple analytical models. The effect of friction was added to the Haurwitz model through eddy viscosity for a two-layered system by Rattray Jr. [1957]. In 1960, Rattray Jr. [1960] proposed the first primitive analytical model to characterize the generated IWs over a flat and sloped bottom in a two-layered system. His model was a milestone in the field as the later studies were built upon it. The wave energy transfer between the surface and internal modes over irregular bottoms such as seamounts was studied by Cox and Sandstrom [1962]. Later, the ray theory was proposed by Sandstrom [1969] to address the multi-mode IW generation and propagation in a variable depth waveguide. It was shown through experiments that in the presence of friction, the standing IWs generated over the shelf propagate as progressive waves [Weigand et al., 1969]. The normal-mode solution obtained in the process of IW generation

over a step-like continental shelf suggested that the amplitude for each mode is inversely related to the mode number [Rattray et al., 1969]. The reflection of IWs from a smooth irregular surface results in the back-reflection of part of energy flux as well as the generation of two new rays where the wave-numbers of the new rays are the sum and difference of surface perturbation and incident wave [Baines, 1971b]. Split-reflection and diffraction of IWs tangent to a bumpy surface was proposed by Baines [1971a]. The model proposed by Baines [1973, 1974] was more realistic than previous ones as it took into account simplified continuous density stratification as well as arbitrary topography (the first study is limited to the topographies which are not tangent to IW propagation direction while the second one addressed the tangent topographies). At this point, the analytical models were developed enough to provide a simplified and effective picture of IW generation and BT to BC energy conversion processes in the ocean.

In addition to the IW generation over sloped topography, IWs can be generated by the interaction of river plumes and tidal currents. A strong waterfront and a two-layered system will form at river mouths where the fresh river water sits at the top of the dense oceanic counterpart at the river mouth. The front, which is a density perturbation will propagate with the wave speed of $c = \sqrt{gH_e}$, where g is gravitational acceleration, and H_e is the depth of the surface layer, in the absence of the counter-ward current with the velocity of U_0. At any time when the Fr number ($\frac{U_0}{c}$) is less than 1, the front can propagate offshore freely. Strong tidal currents can provide a situation that results in modulation of the front propagation speed and the formation of IWs. Such IW signature on the

water surface and strong temperature anomalies were observed at Columbia river, which is believed to be induced by IWs generated through the mechanism as mentioned above [Nash and Moum, 2005]. Such a mechanism is well-known in the atmospheric studies as it can create gigantic waves with the amplitude of 500 meters, i.e. "the morning glory" in which undular bores were generated by the frontal motion into a developing nocturnal inversion [Smith et al., 1982].

2.2 IW Characteristics

Gravity waves are repetitive, patterned oscillations in which the restoration force is the gravity (i.e., ocean surface waves). IWs are a form of gravity waves that occur at the interface of two fluids with different densities or in a density-stratified system. Ironically, based on the definition above, ocean surface waves can be considered as IWs as they occur at the sea surface (interface of ocean and atmosphere). In the presence of a substantial density gradient (such as ocean-atmosphere), the sea surface waves are limited to propagate at the interface (horizontally); however, in a density-stratified water column such as the ocean (where the density gradient is much smaller), IWs propagate in all directions (horizontally and vertically) [Cushman-Roisin and Beckers, 2011]. More formally, IWs occur within a single fluid medium that is density stratified.

2.2.1 Surface Wave Dynamics

To better understand the IWs characteristics, we start from the continuity equation and linearized conservation of mass and momentum (discarding the Coriolis effect) equations simplified by the Boussinesq approximation as below.

$$\begin{cases} \frac{\partial u}{\partial x} + \frac{\partial v}{\partial y} + \frac{\partial w}{\partial z} = 0 \\ \frac{\partial \rho}{\partial t} = -w\frac{\partial \rho}{\partial z} = w\frac{\rho_0}{g}N^2 \\ \frac{\partial u}{\partial t} = -\frac{1}{\rho_0}\frac{\partial P}{\partial x} \\ \frac{\partial v}{\partial t} = -\frac{1}{\rho_0}\frac{\partial P}{\partial y} \\ \frac{\partial w}{\partial t} = -\frac{1}{\rho_0}\frac{\partial P}{\partial z} - \frac{\rho}{\rho_0}g \end{cases} \tag{2.1}$$

where ρ_0 and N are reference density and Brunt-Vaisala frequency ($N^2 = -\frac{g}{\rho_0}\frac{\partial \rho}{\partial z}$). Using equation set 2.1 and kinematic-dynamic boundary conditions, we can derive particle, phase, group velocities as well as pressure perturbation and angular frequency for surface waves [Kundu et al., 2012].

$$\begin{cases} u = a\omega\frac{\cosh(k(z+H))}{\sinh(kH)}\cos(kx - \omega t) \\ w = a\omega\frac{\sinh(k(z+H))}{\sinh(kH)}\sin(kx - \omega t) \\ \omega = \sqrt{gk\tanh(kH)} \\ c = \frac{\omega}{k} = \sqrt{\frac{g}{k}\tanh(kH)} \\ P' = \rho g a\omega\frac{\cosh(k(z+H))}{\cosh(kH)}\cos(kx - \omega t) \\ c_g = \frac{\partial \omega}{\partial k} = \frac{c}{2}\left(1 + \frac{2kH}{\sinh(2kH)}\right) \end{cases} \tag{2.2}$$

where a, ω, k, c, c_g, P', λ and H are wave amplitude, angular frequency, wave number, phase velocity, group velocity, pressure perturbation induced by wave, wave length ($\lambda = \frac{2\pi}{\lambda}$), and total water column depth. Equation set 2.2 depends on H; therefore, for shallow water ($\frac{H}{\lambda} \ll 1$) and deep water ($\frac{H}{\lambda} \gg 1$) we can approximate the $\tanh(kH)$ function by kH and 1. Figure 2.2 shows the effect of water column depth on the particle velocity.

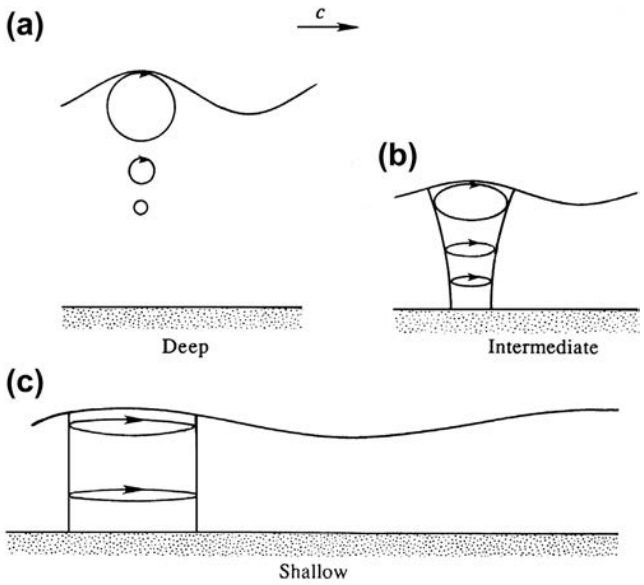

Figure 2.2: The schematic of linear surface wave where Panels a to c show deep, intermediate and shallow water cases Kundu et al. [2012].

In the equations above, without loss of generality, the coordinate axes were rotated so that the surface wave only propagates in x direction.

2.2.2 Internal Wave Dynamics

The surface wave equations are similar to the IW equations; however, IW dynamics depend on density-stratification as well as the Coriolis effect. Therefore, to study IWs, we need to add the Coriolis effect to the momentum equations as:

$$\begin{cases} \frac{\partial u}{\partial x} + \frac{\partial v}{\partial y} + \frac{\partial w}{\partial z} = 0 \\ \frac{\partial \rho}{\partial t} = -w\frac{\partial \rho}{\partial z} = w\frac{\rho_0}{g}N^2 \\ \frac{\partial u}{\partial t} - fv = -\frac{1}{\rho_0}\frac{\partial P}{\partial x} \\ \frac{\partial v}{\partial t} + fu = -\frac{1}{\rho_0}\frac{\partial P}{\partial y} \\ \frac{\partial w}{\partial t} = -\frac{1}{\rho_0}\frac{\partial P}{\partial z} - \frac{\rho}{\rho_0}g \end{cases} \tag{2.3}$$

By adding the Coriolis effect in the momentum equations, we can obtain the wave dispersion relation for IWs [Cushman-Roisin and Beckers, 2011]:

$$\frac{\partial^2}{\partial t^2}\boldsymbol{\nabla}^2 w + N^2\boldsymbol{\nabla}_h^2 w + f^2\frac{\partial^2 w}{\partial z^2} = 0 \rightarrow \omega^2 = \frac{(k^2+l^2)N^2 + m^2f^2}{|\vec{K}|^2} \rightarrow$$
$$\frac{\omega^2 - f^2}{k^2+l^2} = \frac{N^2-f^2}{|\vec{K}|^2} = gH_e \tag{2.4}$$

where $\boldsymbol{\nabla}$ and $\boldsymbol{\nabla}_h$ denote the full and horizontal Laplacian operator and $\vec{K}$ is the wavenumber vector [k , l, m]. The equation above can give the propagation velocity, or the equivalent depth (H_e) as gH_e plays the same role as gH does for surface waves. The whole derivation is only valid if $f < \omega < N$ where N is the maximum frequency of an IW in a system (in the absence of Coriolis, we get $0 < \omega < N$). In highly stratified systems where N is considerably large,

IWs mostly propagate horizontally. The particle motion for any transverse gravity wave such as IWs and surface waves is perpendicular to the phase speed (Fig. 2.3). Although the phase velocity and energy propagation direction for surface waves are the same, this is not the case for IWs as the phase velocity and group velocity (the speed and direction of energy propagation in the system) are perpendicular to each other. The phase and group velocities for IWs can be calculated as [Cushman-Roisin and Beckers, 2011]:

$$\begin{cases} c = \frac{\omega}{\vec{K}} = \frac{\omega}{K^2}(k\vec{e_x} + l\vec{e_y} + m\vec{e_z}) \\ c_g = \frac{\partial\omega}{\partial K} = \frac{(N^2-f^2)m}{\omega K^4}(km\vec{e_x} + lm\vec{e_y} - (k^2+l^2)\vec{e_z}) \end{cases} \tag{2.5}$$

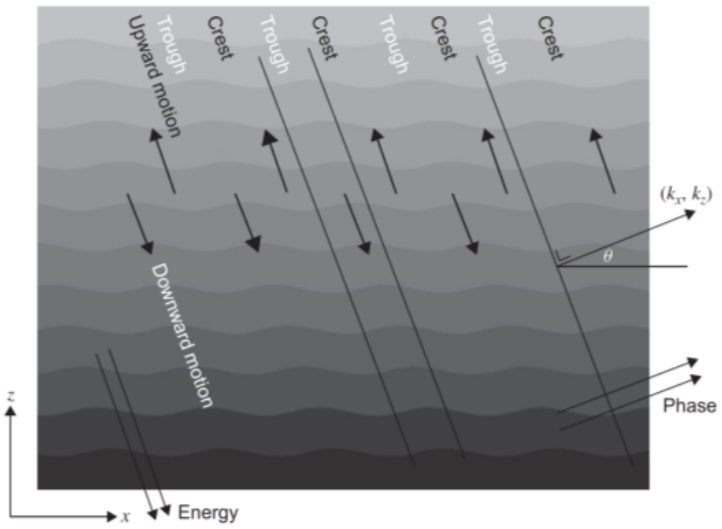

Figure 2.3: The schematic of phase and group velocity directions for IWs which is adopted from Cushman-Roisin and Beckers [2011].

These relations hold for media with almost constant density stratification

(N=const). If N varies slowly over the vertical wavelength, these relations are still valid (WKB approximations)[Kundu et al., 2012]. The angle of the group velocity with horizontal direction is $\theta_{IW} = \frac{\sqrt{k^2+l^2}}{m} = \sqrt{\frac{\omega^2-f^2}{N^2-\omega^2}}$. For $\frac{\omega^2-f^2}{N^2-\omega^2} > 0$, the system response is oscillatory and when it is negative, the oscillations exponentially decay [Cushman-Roisin and Beckers, 2011].

2.2.3 Internal Wave Modal Decomposition

In a density-stratified system, we can decompose the system response into different vertical modes where modes are linearly independent. In this derivation, the hydrostatic pressure assumption and $H < \lambda_z$ were employed. In such a system, we can separate each variable into a horizontal-temporal function (it is shown with the variable name with tilde operator) and vertical functions (ψ, ϕ) where these two functions are orthogonal.

$$\begin{cases} u = \phi(z)\tilde{U}(x,y)e^{-i\omega t} \\ v = \phi(z)\tilde{U}(x,y)e^{-i\omega t} \\ P' = \rho_0\phi(z)\tilde{P}(x,y)e^{-i\omega t} \\ w = i\omega\psi(z)\tilde{P}(x,y)e^{-i\omega t} \\ \rho' = -N^2\frac{\rho_0}{g}\psi(z)\tilde{P}(x,y)e^{-i\omega t} \end{cases} \tag{2.6}$$

where $\tilde{U}$, $\tilde{V}$ and $\tilde{P}$ are only a function of x, y and t; while, ψ and ϕ are only a function of z. Choosing the variables with the general form above automatically satisfy the density equation. Using the equation set above and substituting into

the continuity equation we get:

$$\frac{1}{\tilde{P}}(\frac{\partial \tilde{U}}{\partial x} + \frac{\partial \tilde{V}}{\partial y}) = -i\frac{\omega}{\phi}\frac{\mathrm{d}\psi}{\mathrm{d}z} \tag{2.7}$$

where the equation is possible only when both sides are equal to a constant which we choose to be $\frac{i\omega}{gH_n}$. Using equation 2.6 right side and definitions in equation set 2.5, we can rewrite the continuity equation as below.

$$\frac{\mathrm{d}^2\psi}{\mathrm{d}z^2} + \frac{N^2 - \omega^2}{gH_n}\psi = 0 \tag{2.8}$$

Also, by using the left hand side of equation 2.6 and the continuity equation

$$\frac{\partial \tilde{U}}{\partial x} + \frac{\partial \tilde{V}}{\partial y} = \frac{i\omega}{gH_n}\tilde{P} = 0 \tag{2.9}$$

Considering the similarity of equations 2.7 and 2.8 to surface waves (Poincare waves), the horizontal dispersion relation will be:

$$\omega^2 = f^2 + gH_n(k^2 + l^2) \tag{2.10}$$

By replacing the horizontal structure of the wave (equation 2.9) into equation 2.7, we can eliminate gH_n

$$\frac{\mathrm{d}^2\psi}{\mathrm{d}z^2} + (k^2 + l^2)\frac{N^2 - \omega^2}{\omega^2 - f^2}\psi = 0 \tag{2.11}$$

In this equation, ψ is the eigenfunction, and finite difference technique can be employed to discretize and solve it. By rearranging the discretized version of equation 2.10, we can get the matrix form, $\mathbf{A}(\omega^2)\phi = 0$ where $\mathbf{A}$ is a tridiagonal symmetric matrix of coefficients that depends on ω^2 (ϕ is a an array of vertical modes). Such a situation requires $det(\mathbf{A}) = 0$ for a non-zero ϕ. Finding the eigenvalues of $\mathbf{A}$ gives us the answer for different modes and frequencies [Cushman-Roisin and Beckers, 2011].

2.2.4 Internal Wave Dimensionless Parameters

The steepness number (β_1) and tidal excursion (β_2) are informative dimensionless numbers characterize the reflectivity and periodicity of IWs:

$$\begin{cases} \tan(\theta_B) = \sqrt{(\frac{\partial H}{\partial x})^2 + (\frac{\partial H}{\partial y})^2} \\ \tan(\theta_{IW}) = \sqrt{\frac{\omega^2 - f^2}{N^2 - \omega^2}} \\ \beta_1 = \frac{\tan(\theta_B)}{\tan(\theta_{IW})} \\ \beta_2 = \frac{U_0 k_b}{\omega} \end{cases} \tag{2.12}$$

where U_0 and k_b^{-1} are the maximum BT tidal current velocity and topographic length scale. For IW studies, k_b is estimated as $\frac{\theta_B}{H-d}$ [Garrett and Kunze, 2007, Kang and Fringer, 2012]. In a system with supercritical bathymetry ($\beta_1 > 1$), generated IWs will reflect back offshore while for a subcritical bathymetry ($\beta_1 < 1$), IWs continue their way into the shallower region. A tidal excursion less than one suggests that the IW frequency is similar to the forcing frequency, while $\beta_2 > 1$ gives lee waves [Kang and Fringer, 2012]. Although the tidal excursion does not

directly judge the linearity of a wave, a great amount of turbulence and vorticity are expected along with the Lee waves (which is called rotor in the atmospheric science). Figure 2.4 shows the effects of β_1 and β_2 on generated IWs.

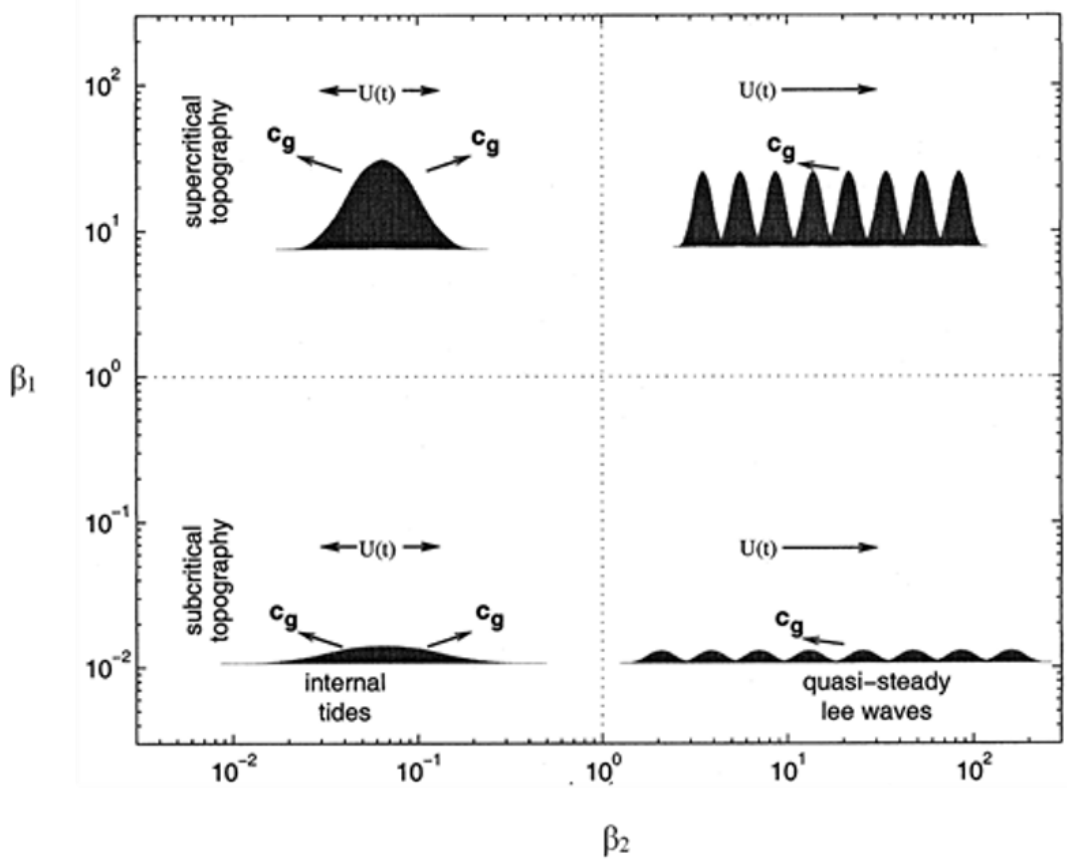

Figure 2.4: The schematic effects of steepness parameter(β_1) and tidal excursion (β_2) on IWs adopted from [St. Laurent and Garrett, 2002]

2.2.5 Nonlinear Waves

Up to this point, I have used linearity to derive and analyze waves; however, the question comes arises "What assumptions did we use to enforce linear waves?

What are the characteristics of linear waves? How to identify nonlinear waves? How do they form? Are they observed in nature?" To answer the first question, we should review the derivation of IW and surface wave formulations in which I discarded the nonlinear advection terms. Therefore, I (and others) assumed that nonlinear advection is negligible in comparison to unsteadiness and pressure gradient terms, and this assumption will be violated when the advection terms become significant. One of the most important characteristics of linear waves is that their amplitude is much smaller than the water column depth and their wavelength. Therefore, the maximum horizontal displacement induced by a linear wave which is equal to $\frac{U_0}{\omega}$ (for a wave of $u = U_0 \sin(kx + ly + mz - \omega t)$) is much smaller than the horizontal wavelength $\frac{2\pi}{(k^2+l^2)^{0.5}}$. Hence, for cases where $\frac{U_0}{\omega} \ll \frac{2\pi}{(k^2+l^2)^{0.5}}$, nonlinearity can be dismissed; otherwise, it should be considered. This ratio can be re-formulated as $U_0 \ll \frac{2\pi N}{(k^2+l^2+m^2)^{0.5}} \leq \frac{2\pi N}{m}$ based on the equation 2.4 (in the absence of Coriolis $\omega^2 = \frac{k^2+l^2}{k^2+l^2+m^2}N^2$) and $\frac{2\pi N}{m} = NH_e$ is the scale of wave speed [Cushman-Roisin and Beckers, 2011]. Hence, effectively, nonlinearity is defined by the Froude number, which is the ratio of current speed over the wave speed $Fr = \frac{U_0}{c}$, which has been used in the literature extensively [Kang and Fringer, 2012, Lai et al., 2010, Lim et al., 2008, Vlasenko et al., 2005, Woodson, 2018].

Waves can become nonlinear in a shallow-water system if the whole wave doesn't propagate at the same speed. The main reason behind such behavior is found in the dependency of wave speed on the water column depth ($c = \sqrt{gH_e}$ where H_e is the equivalent depth). In other words, as waves propagate shore-

ward, the leading edge, which experiences smaller depth, becomes slower than the trailing edge. Such a condition makes the wave steeper, nonlinear, and more asymmetric to the point that it propagates as a bore and finally breaks and dissipates energy (Fig 2.5). Despite the lack of net transport by IWs, internal bores can transport particles XS as they are significantly nonlinear.

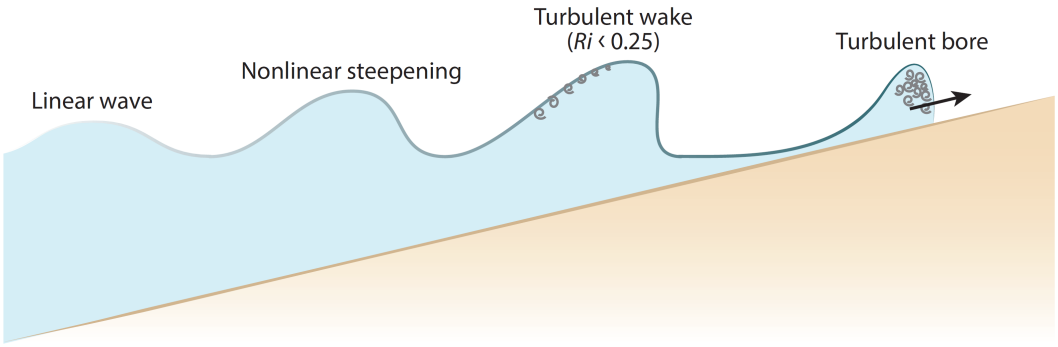

Figure 2.5: The schematic of wave evolution as it approaches the shoreline adopted from [Woodson, 2018]

To become more familiar with the instability and mixing by IWs, I continue the study by analyzing and comparing the energy of an idealized two-layered sheared system after and before complete mixing (where the layer depths are similar, and their velocity and density are different). To make this process possible, the mechanical energy of the system should be smaller after the process in comparison to its initial state. The calculation suggests kinetic energy loss of $\frac{1}{8}\rho_0(U_1 - U_2)^2 H$ where ρ_0 is the reference density disregarding the density difference in the layers and potential gain of $\frac{1}{8}(\rho_2 - \rho_1)gH^2$ in this process, by enforcing the criteria above

yields [Kundu et al., 2012]:

$$\mathrm{KE_{Loss}} \geq \mathrm{PE_{Gain}} \rightarrow \frac{\Delta \mathrm{PE}}{\Delta \mathrm{KE}} \leq 1 \rightarrow \frac{(\rho_2 - \rho_1) g H}{\rho_0 (U_1 - U_2)^2} \leq 1 \tag{2.13}$$

The argument above holds for a sheared flow induced by an IW with the wavenumber of k in a two-layered system. In such a system, the layer surfaces are off-phase by 180°. Also, the particles in the bottom layer move in (against) the direction of the wave under the crest (trough). In contrast, the particle motions are opposite in the upper layer (Fig 2.1). The energy difference before and after the mixing should follow $2\frac{(\rho_2-\rho_1)gH}{\rho_0 k(U_1-U_2)^2} < 1$. Therefore, we can always find a wavelength for which the system becomes fully mixed [Kundu et al., 2012]. Such a phenomenon is known as Kelvin-Helmholtz instability, which occurs widely in the ocean and atmosphere (Fig 2.6) and is accompanied by significant turbulent mixing. As mentioned before, if the potential gain or work done by buoyancy is less than kinetic energy loss or shear work, the system can mix due to overturning. Now, by removing the two-layered system assumption, we can extend our scope and generalize the formulation for more realistic media such as ocean and atmosphere. In such a situation, it can be shown that the system is unstable when $Ri = \frac{N^2}{(\mathrm{d}u/\mathrm{d}z)^2} < \frac{1}{4}$ where Ri is the Richardson number.

Figure 2.6: Kelvin-Helmholtz instability due to a sheared flow in the atmosphere[1].

2.3 IW Physical Importance

Internal bores and IWs significantly affect ocean dynamics by promoting turbulent mixing, energy dissipation, XS transport, and converting energy from BT to BC, which is crucial for global energy budget [Moum et al., 2007, Munk and Wunsch, 1998, Osborn, 1980, Pineda, 1991, Shroyer et al., 2010, Woodson et al., 2011]. In this section, I will review the intensification of mixing and energy dissipation through turbulence followed by the IW XS transport in section 2.5.

[1]The photo is adopted from `https://earthsky.org/earth/kelvin-helmholzt-clouds`

2.3.1 Turbulence

I like to start this section by emphasizing the main characteristics of turbulence as it is hard to define turbulence per se (fluctuation, nonlinearity, vorticity, dissipation-diffusivity). 1) Turbulent flows tend to induce random fluctuation in time-series of the physical flow parameters such as velocity and density. Such perturbations can be filtered or studied by performing time-average decomposition on parameters. To get the turbulent kinetic energy (TKE), I employ the Reynolds Averaged Navier-Stokes (RANS) decomposition. 2) Turbulence is accompanied by nonlinearity when the advection terms in the momentum conservation equation are not negligible; as a matter of fact, for high Reynolds numbers (the ratio of inertial to viscous force) turbulence is expected. 3) Three-dimensional eddies (circular movements of the fluid particles spinning randomly which can be recognized by taking the curl of velocity field) are present in such flows, and I will explain more about the scale of the eddies later on. 4) Finally and most importantly, turbulent flows are effective in mixing and homogenizing the flow and fluid characteristics, including momentum, temperature, density, or any other anomalies present in the fluid. The turbulent mixing in the ocean is so effective that the molecular level is often dismissed in models. The turbulent momentum mixing elevates the energy dissipation in the energy cascade, which eventually leads to the dissipation of energy through molecular viscosity to heat [Kundu et al., 2012].

2.3.2 Energy Cascade

To better understand the scale of eddies, I review the work done by Kolmogorov and Obukhov in 1941, where they found the scale of eddies based on the dimensional analysis. Based on their theory, there are three zones in the energy cascade diagram (TKE energy versus eddy size or length number in Fig 2.7). The biggest size eddies, which are also known as the "integral scale", are the ones producing the TKE; while, the smallest scale ("Kolmogorov scale") is dissipating the energy by converting it into heat. The range between the integral and Kolmogorov is called the "inertial sub-range" which transfers the energy between large eddies to small ones and Kolmogorov hypothesized that in this range, TKE decays exponentially with the slope of $-\frac{5}{3}$ (usually this curve is plotted on a log-log scale in which the relation becomes linear for the inertial sub-range). For the production part, the eddy characteristics (velocity, length, and overturn time) is only a function of TKE and the dissipation rate of TKE; on the other hand, for the destruction part, the eddies attributes depend on the viscosity and dissipation rate of TKE. The inertial sub-range eddies are only controlled by the eddy size and the dissipation rate of TKE. The poem by Richardson summarizes the energy cascade beautifully.

Big whorls have little whorls which feed on their velocity
and little whorls have lesser whorls and so on to viscosity

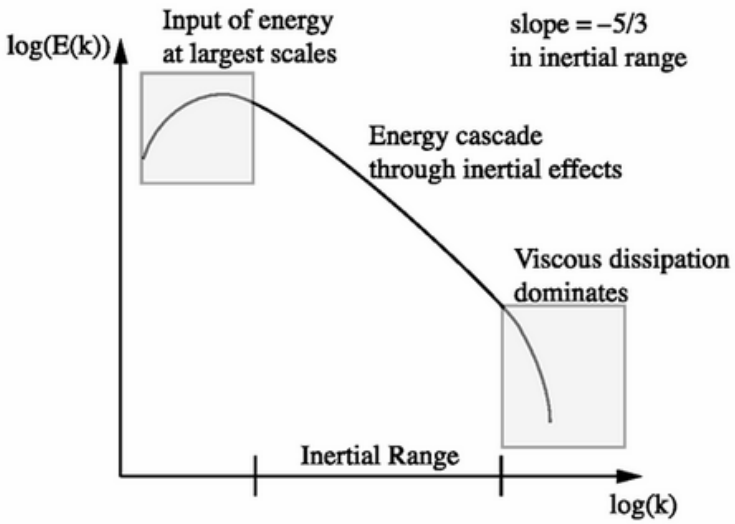

Figure 2.7: Turbulent kinetic energy cascade for different eddy sizes[2].

2.3.3 TKE Dissipation

The total energy of a system that consists of kinetic and potential energy can be lost to viscous dissipation by turbulence. To better understand this, I adopted the mean flow energy (equation 2.14) and TKE budget (equation 2.15) from Kundu et al. [2012] (I skip the derivation and refer the readers to chapter 12).

$$\frac{\partial\langle E\rangle}{\partial t} + U_j\frac{\partial\langle E\rangle}{\partial x_j} = \frac{\partial}{\partial x_j}\left(\frac{-U_jP}{\rho_0} + 2\nu U_i\langle S_{ij}\rangle - \langle u_iu_j\rangle U_i\right) - 2\nu\langle S_{ij}S_{ij}\rangle + \langle u_iu_j\rangle\frac{\partial U_i}{\partial x_j}$$
$$- \frac{g}{\rho_0}\langle\rho\rangle U_3 \tag{2.14}$$

[2]The photo is adopted from `http://ffden-2.phys.uaf.edu/647fall2013_web.dir/j_stroh/tec.html`

where $S_{ij} = 1/2(\partial U_i/\partial x_j + \partial U_j/\partial x_i)$, $\langle E \rangle = 1/2U_i^2$, the angled-bracket operator, small and capital velocities denote the time-average of a parameter, mean and turbulent velocities. Also, the small and capital letter velocities are the mean and perturbation constituents. In equation 2.14, the RHS terms are transport, viscous dissipation (directly convert the mechanical energy to heat), loss to turbulence and loss to potential energy.

$$\frac{\partial \langle e \rangle}{\partial t} + U_j \frac{\partial \langle e \rangle}{\partial x_j} = \frac{\partial}{\partial x_j}\left(\frac{-u_j P}{\rho_0} + 2\nu \langle u_i S'_{ij} \rangle - \frac{1}{2}\langle u_i^2 u_j \rangle U_i\right) - 2\nu \langle S'_{ij} S'_{ij} \rangle - \langle u_i u_j \rangle \frac{\partial U_i}{\partial x_j} + \frac{g}{\rho_0}\langle u_3 \rho' \rangle \tag{2.15}$$

where $S'_{ij} = 1/2(\partial u_i/\partial x_j + \partial u_j/\partial x_i)$, $\langle e \rangle = 1/2u_i^2$. The RHS terms are transport, viscous dissipation rate (dissipation of TKE, which is known as ϵ), gain from the mean flow, and buoyant production. The viscous dissipation in equation 2.14 is negligible as the energy cascade requires the energy transfer from big scale eddies to TKE first. On the other hand, in equation 2.15, the viscous term is significant as the small eddies convert the energy to heat efficiently. In the ocean, we can use the steady-state assumption for the TKE budget [Osborn, 1980]; therefore, we can conclude that Turbulent Production= - Dissipation - Buoyancy Production. The Richardson flux number ($Ri_f = \frac{\text{Buoyancy Production}}{\text{Turbulent Production}}$), which shows the balance between turbulent and buoyancy production should always be less than 1; otherwise, the TKE will decay and will not remain steady [Osborn, 1980]. Businger [1973] and Britter and Simpson [1978] suggested the value of 0.15 for critical Ri_f above which, the TKE will not be steady. The diapycnal eddy diffusivity of K_ρ which

governs the mixing in the ocean and atmosphere, can be found using ϵ, N^2 and buoyancy production by $K_\rho \leq \frac{\text{Buoyancy Production}}{N^2} = \frac{Ri_f \epsilon}{(1-Ri_f)N^2} = \frac{0.15}{0.85}\frac{\epsilon}{N^2} = 0.2\frac{\epsilon}{N^2}$ [Osborn, 1980]. We should note that the value mentioned is the maximum of mixing and diffusivity in the ocean, and not all the system reaches that.

Based on the discussion above, studying ϵ can be beneficial, as it can help to analyze eddy attributes (both in the Kolmogorov scale and sub-inertial), to study the TKE budget for a system as well as to provide the turbulent mixing efficiency coefficient. The turbulent production term exists when the non-zero Reynolds stress is present, which requires $\overline{u_i u_j} \neq 0$ as well as shear in the mean flow ($\partial U_i / \partial x_j$). One of the best examples of such a situation is the presence of IWs where particles move in opposite directions in the top and bottom layers (such as the particle movements shown in Fig 2.1) and turbulent fluctuations are present. The shear stress in the system excites instability and overturning, as mentioned before ($Ri < 0.25$ may induce instability). Therefore, I briefly summarize some of the well-known studies that calculated and measured ϵ for a system perturbed by IWs and internal bores.

Internal bores and IWs can be recognized with a significant temperature drop as they bring up colder deeper water. Such a signature can be seen in the study conducted by Palmer et al. [2015] in the Celtic sea, where the arrival of IWs can be identified by an abrupt density increase, which is accompanied by high values of ϵ (Fig 2.8). Also, IWs can re-suspend the sediments by inducing shear stress at the ocean bottom, which can be seen in Fig 2.9 (left panels). The correlation between the backscatter and elevation of ϵ (Fig 2.9 right panel) suggests that

this is done by IWs. The shear instability ($Ri < 0.25$, which can be seen in Fig 2.10 top panel) induced by the nonlinear IWs train significantly increased the ϵ at pycnocline by several orders of magnitude. The high cross-correlation between ϵ and shear velocity has also been reported by Inall et al. [2000] in the Malin shelf during trains of nonlinear internal tides (Fig 2.11).

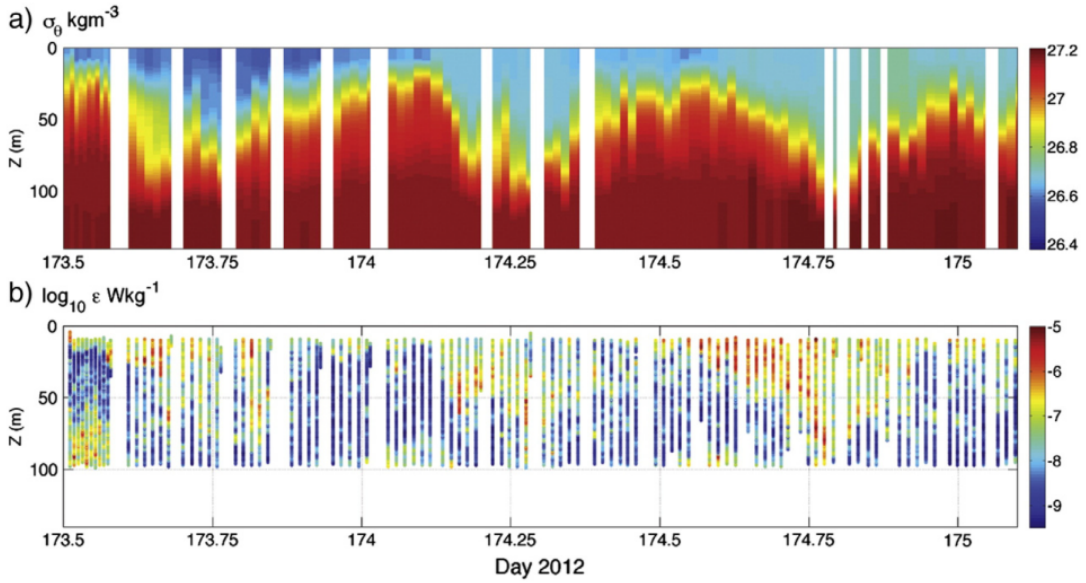

Figure 2.8: The top panel is showing the density while the lower one provides the ϵ [Palmer et al., 2015]

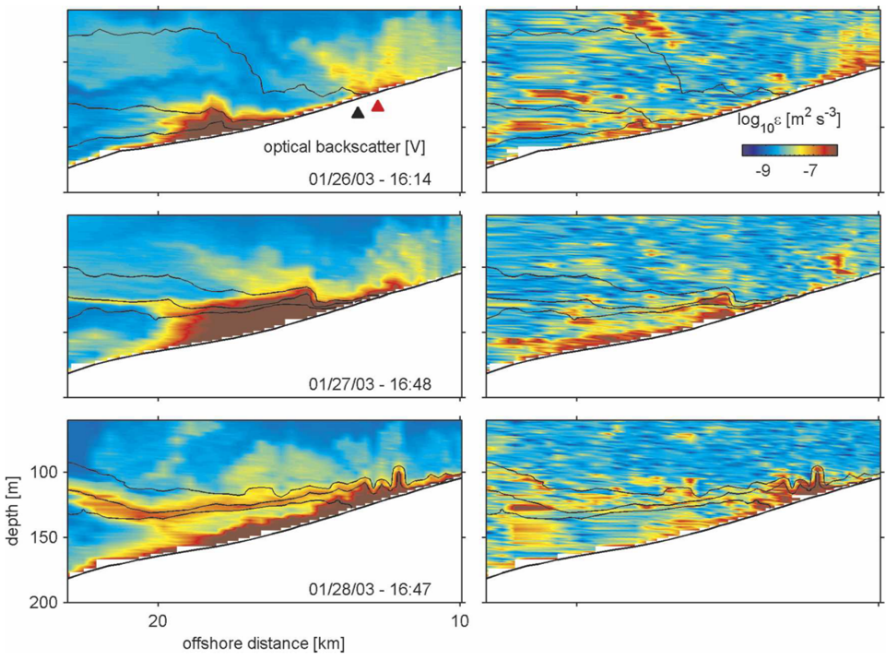

Figure 2.9: The left column shows the backscatter which is a proxy for suspended sediment and the right one provides the TKE dissipation rate (ϵ) [Moum et al., 2007]

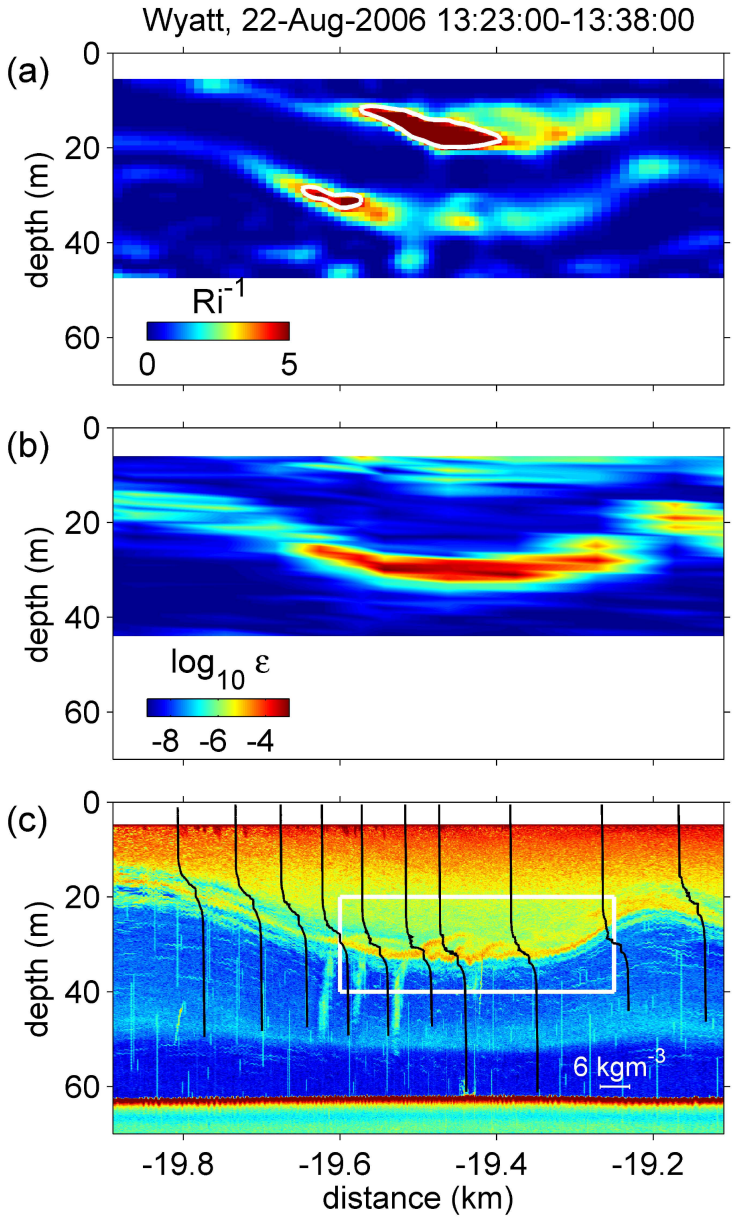

Figure 2.10: The panels show Ri^{-1} (the white counter shows the critical Richardson number of 0.25), ϵ and back-scatter from top to bottom [Shroyer et al., 2010]

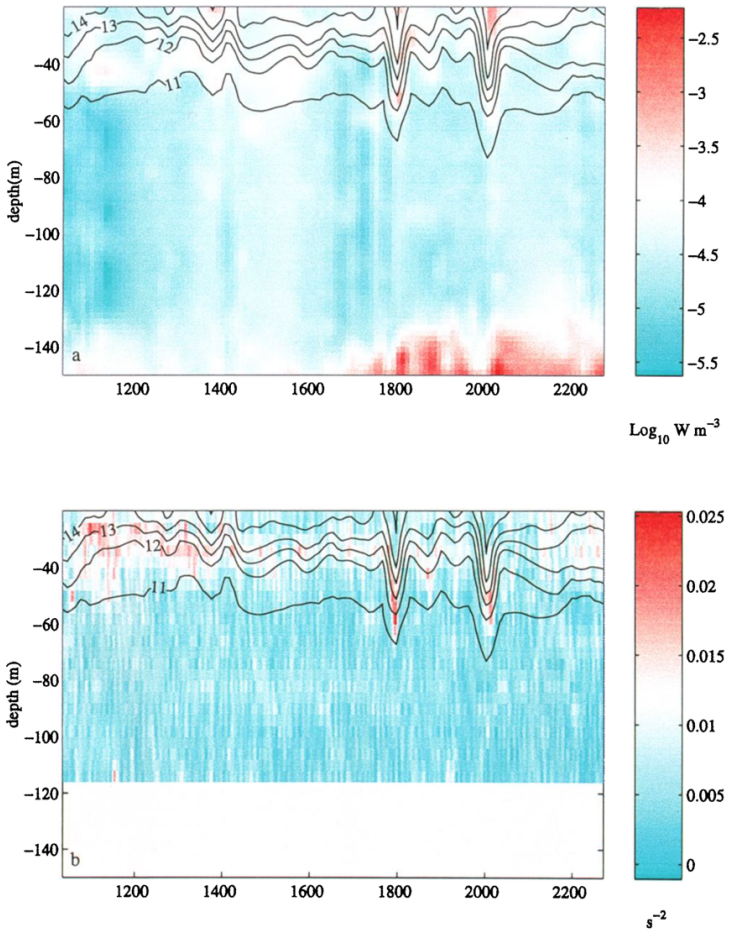

Figure 2.11: The top panel gives the ϵ while the shear velocity squared is shown in the lower panel for the period 1 from Inall et al. [2000]

2.4 IW Chemical Importance

As mentioned, IWs become more nonlinear as they propagate toward the coast, and such non-linearity enables them to transport materials XS [Kundu et al., 2012]. The generation of IWs is promoted in a system with prominent pycnocline, where the top warmer fresh low-nutrient water sits on top of a cold salty high-

nutrient layer. The shoaling IWs which ride on the pycnocline deliver water from the lower layer to the coastal ecosystems. Such a phenomenon provides a chance for coastal ecosystems to experience high-nutrient cold, deeper water. Moreover, the shoaling IWs can increase the likelihood of overturning and turbulent mixing as they increase the velocity shear gradient between layers. Many studies have reported the promotion of nutrient concentration in pelagic zones, kelp forests, and coral reefs by IWs through the aforementioned processes, which I briefly summarized as below.

2.4.1 Pelagic Zone

The presence of large-amplitude IWs was observed in the Bay of Biscay by Holligan et al. [1985] where the nitrate concentration (which regulates the productivity of phytoplankton) was altered (in comparison to other locations in eastern North Atlantic) by IWs during summer periods. The spring-neap variation in the maximum of nitrate and chlorophyll concentration at shelf edge of Celtic Sea where strong ITs are present suggests that the turbulent mixing is induced by ITs [Sharples et al., 2007].

2.4.2 Kelp Forest

The breaking semi-diurnal ITs and bores observed in Monterey Canyon with a large amplitude of 50 to 120 meters are the main contributor of temperature anomalies (20 meters thick lens of warm water), macro-nutrient enrichment and significant amount of (30% of primary productivity in the Northern Monterey

Bay) nutrient transport during the non-upwelling seasons [Shea and Broenkow, 1982]. Measurements conducted in 2001 to 2003 suggested diurnal ITs as the primary mechanism which supplies dissolved inorganic nitrogen to the kelp forest in the inner shelf of the Santa Barbara Channel during the summer when all other mechanisms (storm runoff and upwelling) are inactive[McPhee-Shaw et al., 2007].

2.4.3 Coral Reef

The arrival of IT bores can be recognized as a sudden variation in the temperature and salinity as well as upwelling of high-nutrient cold deep water for four hours. Such a phenomenon results in the promotion of chlorophyll-a during the summer and fall at Conch reef of Florida keys [Leichter et al., 1996]. The experiment conducted on the coral reef at the Conch Reef Florida Keys suggested that the algae growth rate is increased after each episode of IWs [Smith et al., 2004]. Large amplitude IWs cause abrupt temperature drops accompanied by a high concentration of inorganic nutrients and promote the primary productivity of coral reefs at the west of Similan Islands, while such features are absent in the east side [Jantzen et al., 2013].

2.5 Biological Importance

In addition to providing nutrients, IWs can enhance recruitment by transporting larvae onshore, affect the prey-predator dynamics, and increase the fertilization rate. Ecosystem dynamics depend on larval settlement and recruitment, which is

a critical component of invertebrate and fish larvae life and requires shoreward transport. While small larvae are not capable of swimming and they need extended shoreward transport by any means (IWs or other mechanisms), larger ones can swim to some extent, and they need the final push [Woodson, 2018]. There are many ways of onshore transport in coastal oceans, including tidal currents, coastal circulation, IWs, and internal bores. Therefore, it is imaginable to observe a high larval settlement rate during the episodes of IWs and internal bores. Not only can larvae be transported shoreward, but also the discharged effluent and chemical plumes through an offshore ocean outfall can return to the surf zone [Boehm et al., 2002]. IWs can affect prey-predator dynamics in a system as they increase the chance of their encounters as well as relaxing a stressed environment due to lack of oxygen or low PH [Woodson, 2018]. Finally, in the presence of IWs, which promote turbulence mixing temporarily, the fertilization rate grows significantly as the possibility of sperm-egg encounter rises remarkably. Below, I review some of the studies supporting these observations.

2.5.1 Recruitment Rate

The benthic settlement rate can increases significantly through shoreward transport of larvae by nonlinear IWs. Abrupt variations in density stratification and temperature, which can be the indications of bore presence in the system, were accompanied by a significant increase in barnacle settlement rate in several sites (synchronously) in the bay of Todos Santos Northern Baja California [Ladah et al., 2005]. The semi-diurnal predictable significant temperature drops observed in the

Southern California Bight can be attributed to the advection of subsurface cold water induced by internal bores (in the absence of active upwelling during summer), which is synchronized and correlated with the settlement rate of larvae [Pineda, 1991]. In addition to the shoreward transport by internal bores (Fig 2.12 panels A to C), Pineda [1994, 1999] proposed and tested the theory of shoreward advection of larvae by the return flow of surface layer in response to the bores (Fig 2.12 panels E to G).

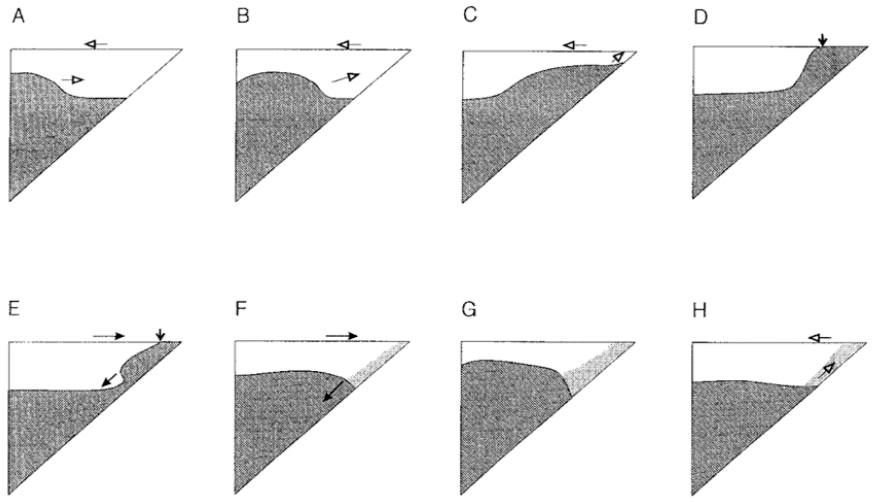

Figure 2.12: The schematic of internal bore (panel A to C) and shoreward return flow of the surface layer (panel E to F) adopted from Pineda [1994] for a two-layered system.

Another mechanism of larvae onshore transport was introduced and tested by L. Shanks and G. Wright [1987], Shanks [1983, 1986] in which he suggested that the larvae which are trapped in the surface slicks (a minimal drop at the sea surface elevation or convergence zone induced by IWs shown in Fig 2.1 where impurities can get stuck in it) can propagate shoreward for significant distances

(more than 1 kilometer).

2.5.2 Predatory-Prey Dynamics

It was recognized that although tidal flow significantly affects the prey-predator confrontation, IWs can promote fish schooling, especially near the water surface over the shallow sea banks [Embling et al., 2013]. The mixing of turbid surface water induced by IWs can alter the light intensity, which in turn causes the vertical migration of fishes (which is significantly higher than diel vertical migration); moreover, such vertical migration increases the chance of successful visual foraging among planktivorous fish [Kaartvedt et al., 2012]. Vertical oscillations induced by breaking IWs mixes and scatter larval fishes accumulated at the water surface in the whole water column, which increases the likelihood of prey-predator encounter [Greer et al., 2014].

2.5.3 Fertilization Rate

Benthic invertebrates reproduce through broadcast spawning during which the eggs and sperms are released concurrently at separate locations, and it is up to the local mixing (through IWs and high-frequency internal bores) and sperm motility to mix them [Crimaldi, 2012]. A numerical study conducted by Crimaldi and Browning [2004] confirms this theory and suggests that the enhancement of turbulent mixing in the water column by IWs results in the promotion of spawning efficiency as IW stirring gives the gametes a better chance to fertilize.

2.6 Wind Effects on Coastal Dynamics

Wind stress and sea breeze can significantly affect the coastal dynamics by causing circulation, mixing, XS, and AS currents. In this section, we briefly review the Ekman phenomena as well as the possibility of XS transport by the XS wind in the shallow regions.

2.6.1 AS Wind & Ekman

In 1905, Ekman [1905] analytically solved the conservation of momentum equations for a system perturbed by wind shear stress where all the advection, unsteadiness and pressure gradient terms were discarded, and the Coriolis force was balanced with the viscous forces ($-fv = \nu_v \partial^2 u/\partial z^2$ and $fu = \nu_v \partial^2 v/\partial z^2$). Solving this equation considering the boundary condition at the surface ($\tau = \rho_0 \nu_v \partial u/\partial z$) results in the emergence of Ekman spiral with the net transport perpendicular to the direction of the wind (to the left of the wind in the southern hemisphere and right in the southern one as shown in Fig 2.13). The Ekman velocity profile suggests a 45° deviation at the water surface and exponential decay with the depth with the net transport of $\frac{\tau}{\rho_0 f}$.

$$\begin{cases} u = \frac{\tau}{\rho_0 \sqrt{f \nu_v}} \exp\left\{\frac{z}{\delta_E}\right\} \cos\left(-\frac{z}{\delta_E} + \frac{\pi}{4}\right) \\ v = -\frac{\tau}{\rho_0 \sqrt{f \nu_v}} \exp\left\{\frac{z}{\delta_E}\right\} \sin\left(-\frac{z}{\delta_E} + \frac{\pi}{4}\right) \end{cases} \tag{2.16}$$

where δ_E is the Ekman layer depth and is equal to $\sqrt{2\nu_v/f}$ in which ν_v is a constant eddy viscosity in an unstratified system. If the turbulent viscosity is

not constant, $\delta_E = 0.4\frac{\sqrt{\tau/\rho_0}}{f}$ Cushman-Roisin and Beckers [2011]. This equation holds for a system where $H \gg \delta_E$, which usually happens on the continental shelf (offshore of the inner-shelf area); otherwise, the spiral does not form completely, and it might create a different regime which I review in the next section.

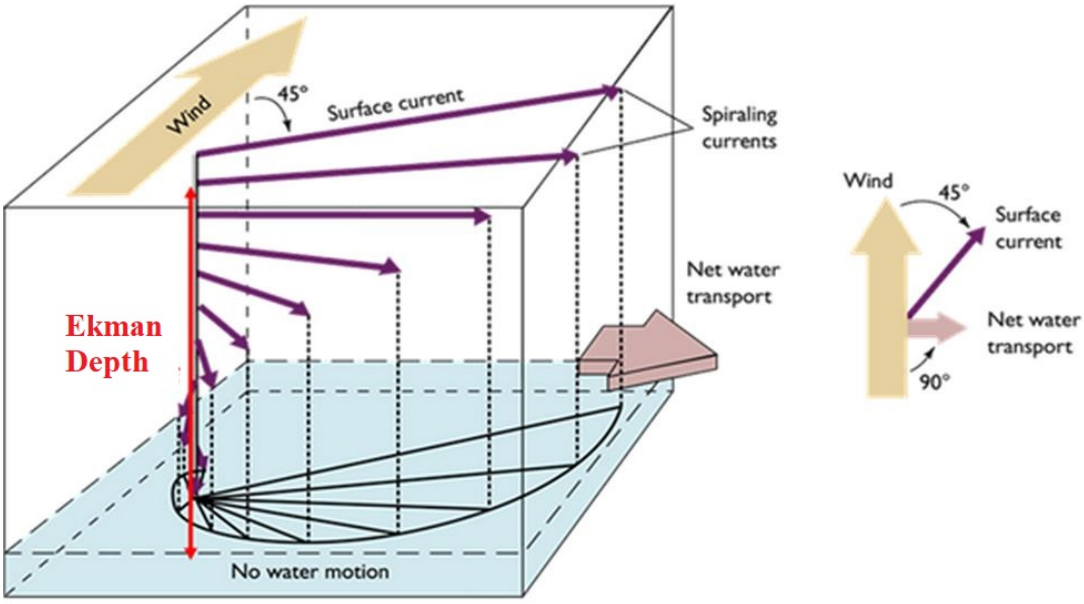

Figure 2.13: The schematic of Ekman surface layer spiral in the northern hemisphere[3].

The same process can happen to the current flowing in the X direction with the depth-averaged velocity of U_0 over the ocean bottom. This creates the Ekman bottom layer in which the net transport is deflected by 45° instead of 90°. The velocity profile of the Ekman bottom layer is close to the Ekman surface layer as they both decaying exponentially with depth, while the flow direction is a bit

[3]The photo is adopted from `https://www.offshoreengineering.com/education/oceanography/ekman-current-upwelling-downwelling`

different (the depth-integral of the equation 2.17 leads to $u = v = 0.5$).

$$\begin{cases} u = U_0\left(1 - \exp\left(\frac{-z}{\delta}\right)\cos\frac{z}{\delta}\right) \\ v = U_0 \exp\left(\frac{-z}{\delta}\right)\sin\frac{z}{\delta} \end{cases} \tag{2.17}$$

Based on the perpendicular net transport, Ekman concluded that AS wind causes upwelling and downwelling if the Ekman spiral forms sufficiently. Such AS wind creates a two-layered shear velocity with a return flow in the bottom layer (Fig 2.14).

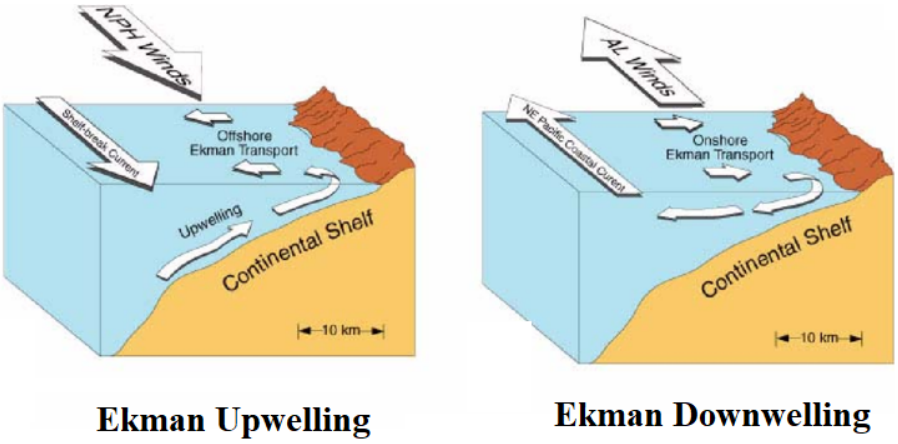

Figure 2.14: The schematic of Ekman upwelling and downwelling for AS wind[4].

Predicting the Ekman upwelling is not a trivial task as the tidal XS currents complicate the dynamic significantly, and current decomposition can be challenging. Moreover, the density stratification can add to the perplexity of the system further as it suppresses the mixing and diffusion in the water column. Lentz [2002]

[4]adopted from https://www.researchgate.net/figure/41-Main-features-of-the-upwelling-favorable-wind-conditions-off-west-coast-of-Vancouver_fig4_228795560

observations suggest a good agreement between the theoretical XS transport (Fig 2.15) and data obtained from the Chesapeake Bay during a stratified period. The flow regime was similar to a typical Ekman layer (Fig 2.16); however, for a weakly stratified case, a discrepancy was observed, which is attributed to $H > \delta_E$.

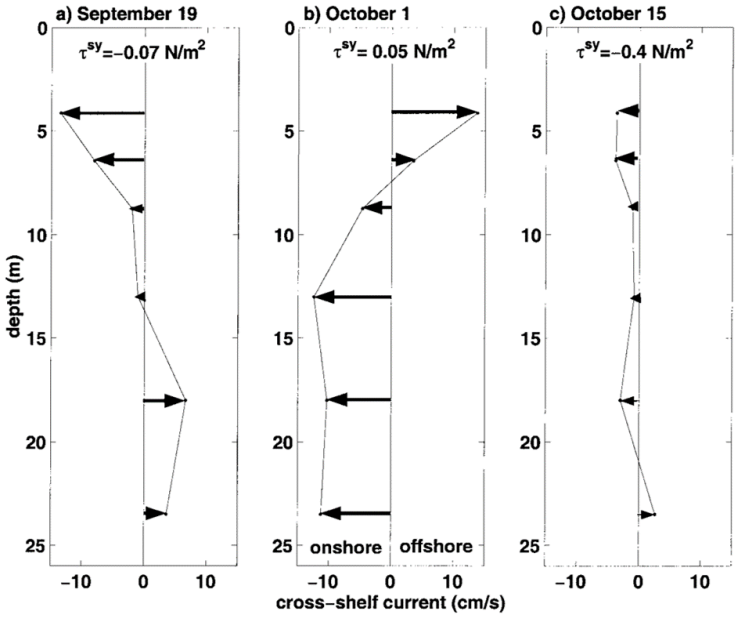

Figure 2.15: The XS velocity at the Chesapeake Bay for a stratified (a,b) and unstratified (c) system [Lentz, 2002].

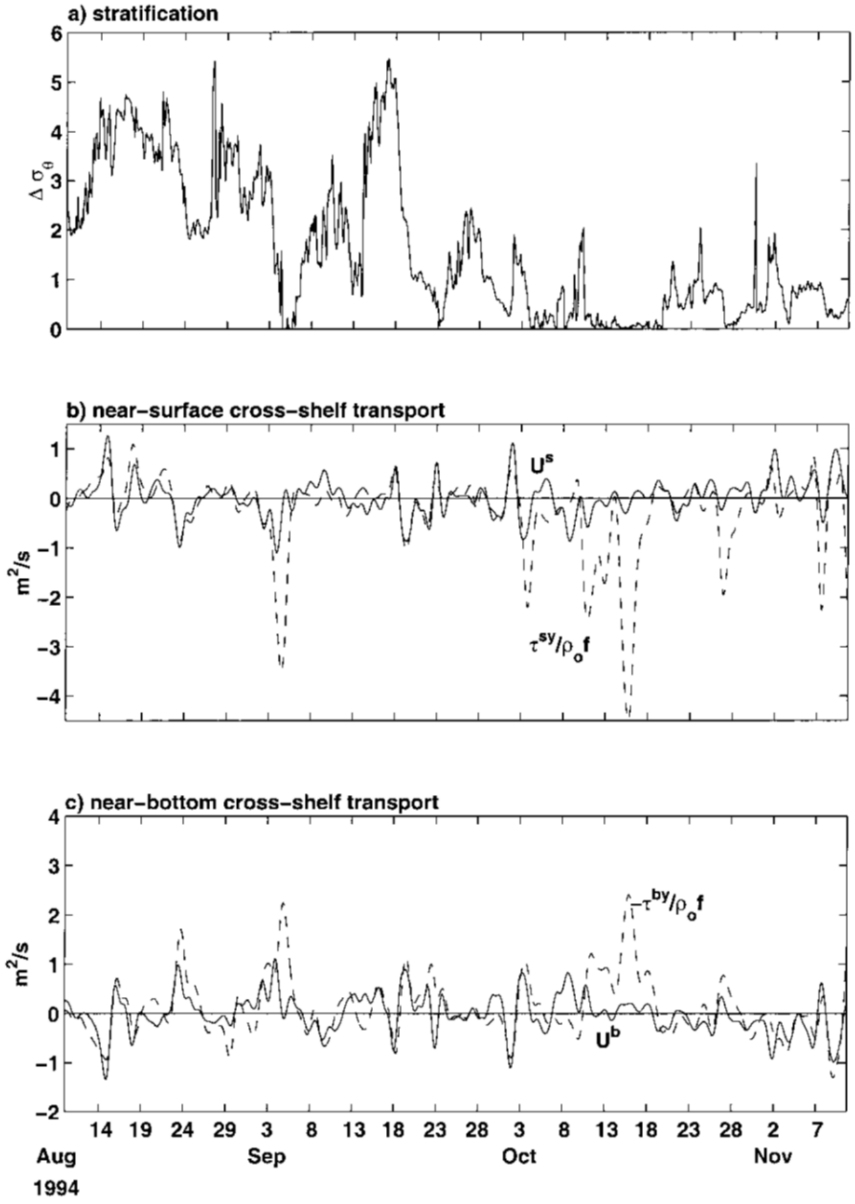

Figure 2.16: The panels show density, near-surface transport and near-bottom XS transport respectively for a profile 26-meters deep at the Chesapeake Bay [Lentz, 2002].

Buoyant particles are good indicators to follow the flow regime closer and more

accurately. The Ekman upwelling/downwelling affects the buoyant plume width, thickness, propagation speed, and its direction as well as the slope of isopycnals. The presence of downwelling wind made the plume thicker, more narrow, and sharpened the isopycnals, while the upwelling wind made the plume wider and flattened the isopycnals, which can be seen in Fig 2.17 [Lentz and Largier, 2006].

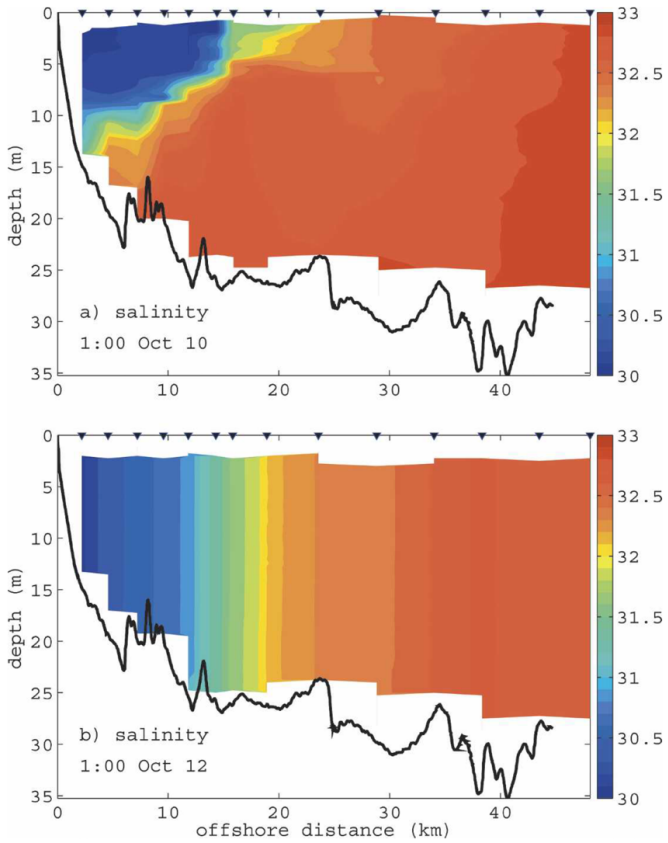

Figure 2.17: The salinity profile during a weak downwelling (top panel) and strong upwelling (bottom panel) where the isopycnal became vertical and turbulent mixing is promoted (low Ri number) [Lentz and Largier, 2006]

Many other studies documented the significance of Ekman transport in the

coastal system as it can act as a nutrient pump bringing up the cold high-nutrient water as well as affecting the energy budget [Hickey et al., 2005, Kirincich et al., 2005, Lentz, 2002, Tilburg, 2003, Woodson, 2013, Woodson et al., 2007].

2.6.2 XS Wind in Shallow water

The AS winds are not the only wind which can create a XS net transport. In the inner-shelf regions, where the bottom and surface Ekman layers overlap, the situation becomes even more complicated. Many observations proposed the inefficiency of AS winds in creating XS transport; instead, XS winds dominate the XS transport [Fewings et al., 2008, Tilburg, 2003]. As shown in Fig 2.18, when the water column depth gets lower than 25 meters, the ratio of AS wind stress to theoretical Ekman transport is high, and the transport is not dominated by the AS wind.

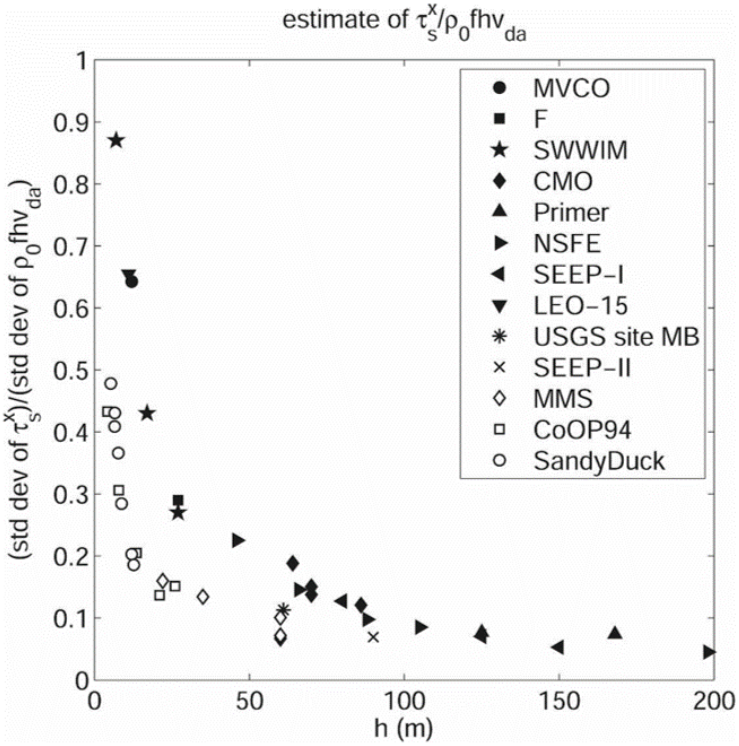

Figure 2.18: The efficiency of the AS wind in deriving XS transport for different studies reviewed by Fewings et al. [2008]

A simple symmetric two-dimensional two-layered model was proposed by Fewings et al. [2008] where the top layer advects in the wind direction, and the bottom layer has a return flow opposite to the surface flow creating a sheared flow system (Fig 2.19). The thickness of the top layer is reported to by one-third of the water column depth [Fewings et al., 2008]. This mechanism is stronger during the summer when the stratification is intensified.

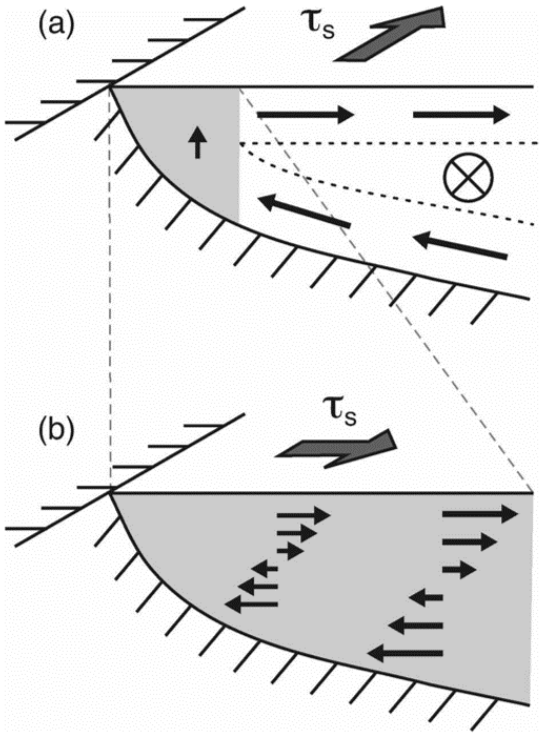

Figure 2.19: The schematic of XS transport in inner to mid-shelf Fewings et al. [2008].

2.7 Monterey Bay

Monterey Bay, a well-known and favorable site for IW generation and breaking bores, is located on the central coast of California. Monterey Bay contains one of the largest nearshore submarine canyons, as well as a great number of supercritical ridges (Fig 2.20). The semi-enclosed geometry of the bay traps water inside the bay and creates warm shallow water lenses that propagate north and south in the bay. Upwelling and the mixing induced by IWs promotes the biological activity

and fishery industry in Monterey Bay. Salinity and temperature anomalies (Fig 2.21) observed in the bay are attributed to the strong IWs generated by the tidal flows over the 1) local coastal region, 2) steep submarine canyon as well as 3) the ones which are remotely generated and propagated towards the shore.

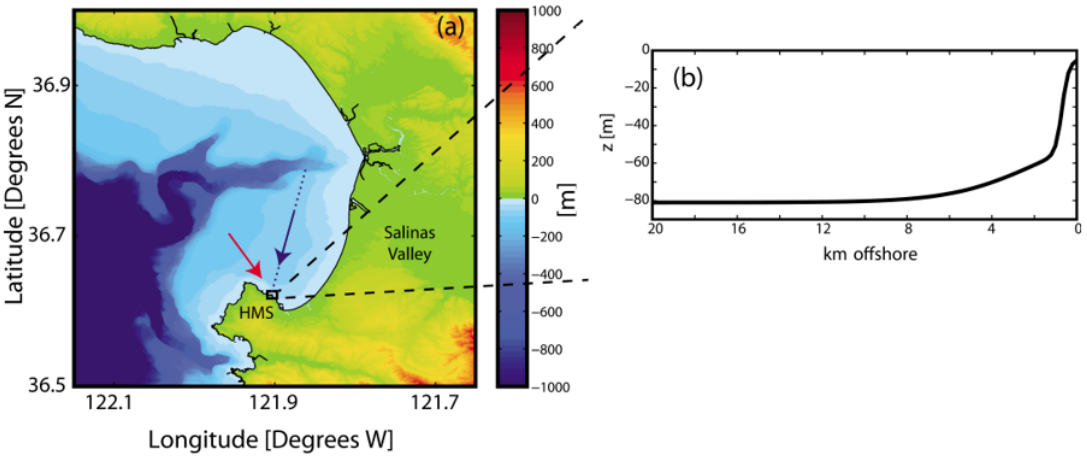

Figure 2.20: a) The topography of Monterey bay region [Walter et al., 2012] with the local diurnal sea breeze at Hopkins Marine Station (red arrow) based on [Woodson, 2013]. b) The bathymetry profile is provided along the blue dots [Walter et al., 2012].

2.7.1 Shallow Warm Water Lenses

Wind-driven upwelling is a dominant feature of the California coast during the late spring till fall (March to August), which affects the dynamics of Monterey Bay significantly. During this time, regional-scale winds from the north Pacific high are to the southeast over the California coast, which cause strong offshore Ekman transport and upwelling [Beardsley et al., 1987]. Cold upwelled water in the north of Monterey Bay (Point Año Nuevo) advects southward and form a

thermal front which traps the water inside the bay [Graham and Largier, 1997, Paduan and Rosenfeld, 1996, Rosenfeld et al., 1994]. The thermal barrier reduces the XS water exchange of the bay and increases the residence time of the water up to 8-17 days [Graham and Largier, 1997, Woodson et al., 2007]. During this time, due to surface heating, the cold trapped water inside the bay warms up and forms shallow warm water lenses with a thickness of 4-7 meters and temperature difference of up to 10 degrees Celsius, as shown in Fig 2.21 [Woodson et al., 2007].

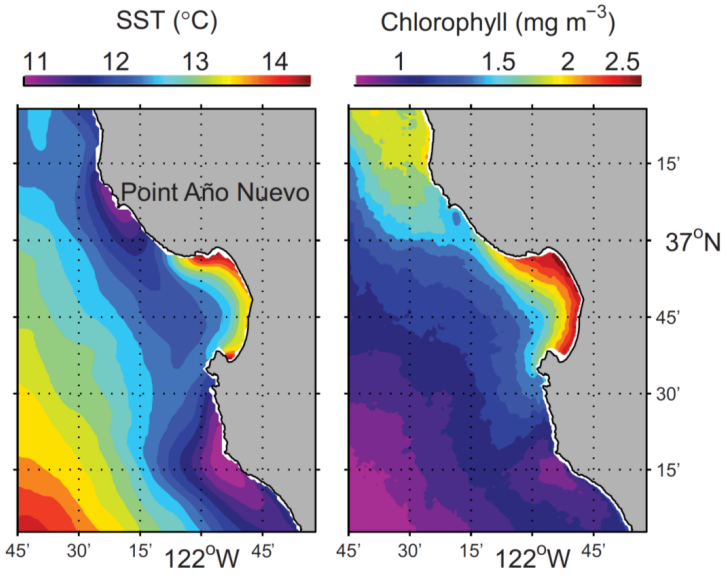

Figure 2.21: Sea surface temperature and chlorophyll concentration in Monterey Bay [Zhang et al., 2016].

2.7.2 Diurnal Sea Breeze

In addition to regional upwelling winds, Monterey Bay is perturbed by the local diurnal sea breeze during the upwelling season. The diurnal sea breeze is due to

the pressure gradient between Salinas Valley (because of significant solar heating) and Monterey Bay water in the afternoon during periods of strong regional scale upwelling [Banta et al., 1993]. These sea breezes are westerly in the northern and central parts of the bay and northwesterly in the southern part of the bay near Hopkins Marine Station (HMS) (the red arrow in Fig 2.20) [Woodson, 2013]. Therefore, the diurnal sea breeze can be counted as XS wind rather than AS.

2.7.3 Tides

Barotropic tides with different frequencies are observed to propagate in Monterey bay freely. The main constituents of barotropic tides in the northern and southern part of the bay are shown in Table 2.1. All parts of the bay experience the same phase for each of the tidal components (the phase lag is less than 1-degree as shown in Table 2.1); therefore, the tides are freely propagating in the bay rather than being trapped. Over the shelf, tidal current ellipses with magnitudes as high as 20 cm/s are mostly aligned toward the canyon head while close to the shore the tidal ellipses are almost parallel to the coast (Fig 2.22) [Carter, 2010, Petruncio et al., 1998].

Table 2.1: Main tidal constituents near in the northern (southern) part of Monterey Bay [Petruncio et al., 1998]

Constituent	Period (hour)	Amplitude (cm)	Greenwich Phase (degree)
M_2	12.42	48.9 (49.5)	181.9 (180.9)
K_1	23.93	36.4 (36.0)	219.5 (220.3)
O_1	25.82	22.8 (22.8)	203.1 (203.9)
S_2	12.00	13.0 (13.1)	180.7 (179.6)
P_1	24.07	11.5 (11.4)	216.4 (218.5)
N_2	12.66	11.2 (11.2)	155.9 (154.2)

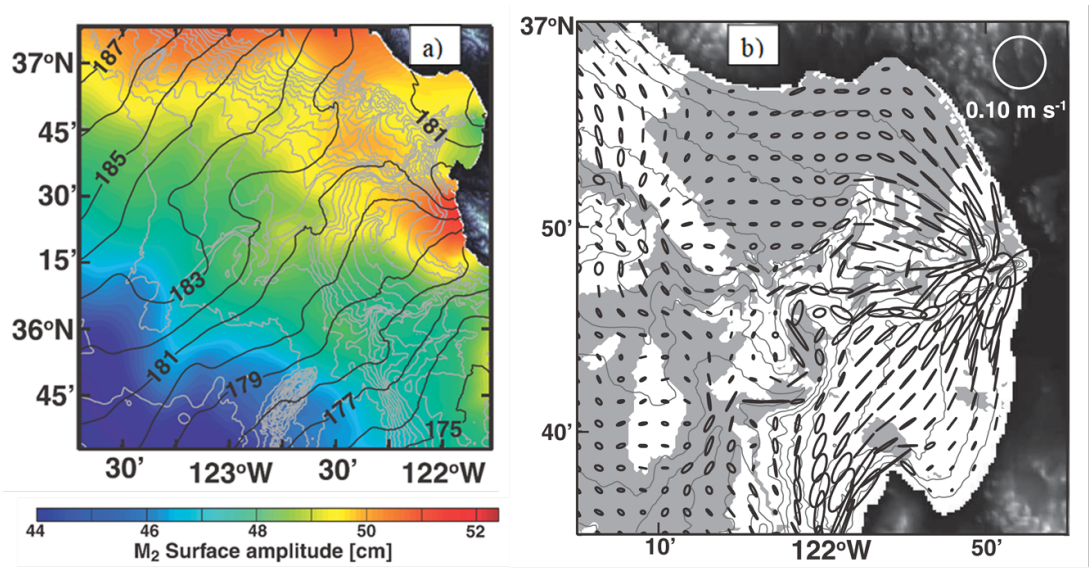

Figure 2.22: M-2 surface amplitude (colors) and phase (black contours) are shown in a, while b shows the depth-averaged M_2 tidal current ellipses [Carter, 2010].

2.7.4 Biological Activity

Monterey Bay has a high biological production due to 1) shallow (less than 80 meters) thermocline (depth at which temperature varies abruptly) and nutricline (steep gradient in nutrient concentration), 2) favorable upwelling-wind which brings up the nutrient from the deeper colder high-nutrient water, and 3) have access to a strong source of iron on the coast which is crucial for phytoplankton [Barber and Chavez, 1983, Chavez et al., 2002, Johnson et al., 1999].

Such characteristics are absent during an El Nino (an event which happens every 3-7 years during which the favorable upwelling-wind shuts down in the west coast of United States) which causes a decline (up to % 70 reported by Chavez et al. [2002]) not only in the phytoplankton biomass but also in the higher trophic elements which are tied to the fishery industry [Barber and Chavez, 1983, Johnson et al., 1999, Zeidberg et al., 2006]. The presence of El Nino can dramatically shift the dynamic of the Monterey Bay ecosystem so that some of the rare species become abundant in the mid-water, while some of the common ones become scarce [Raskoff, 2001].

Chapter 3

THEORETICAL FRAMEWORK

In addition to the biological, chemical, and physical importance of IWs, we should consider their unique role in closing the global energy budget. The ocean has a critical role in the re-distribution and circulation of the solar energy flux absorbed at the ocean surface as it homogenizes the ocean temperature through a mechanism called meridional ocean circulation (MOC). The MOC, which is a large-scale phenomenon driven by winds and density-gradients, promotes a more uniform thermal energy distribution by cooling down (warming up) the equatorial (polar) regions. The temperature of pole-ward currents (induced by winds) declines by surface cooling, while its salinity increases through water evaporation and double diffusion convection (salt fingering) as they get closer to the poles where they sink and form deep water slowly. The pressure gradient between polar and the equatorial regions creates an equator-ward return current. Such a system sinks a great amount of water (30 Sverdrup), which results in a strongly density-stratified

system [Munk and Wunsch, 1998]. Therefore, a process is required to counteract this stratification through mixing as without it, the ocean will become a stagnant pool of water where the mixed warm water sits on the top of a cold salty layer. As discussed in the previous chapter, breaking IWs are one of the processes which amplify diapycnal turbulent mixing. The energy required for abyssal mixing is approximated to be ~ 2 TW by Munk and Wunsch [1998] where half of it is provided by IWs. According to Munk and Wunsch [1998], the received gravitational solar and lunar energy flux is approximated to be 0.5 and 3.2 TW from which 2.5 TW is focused on M_2 semi-diurnal frequency (Fig 3.1). From the 3.7 TW received energy, 3.5 TW of it propagates as surface tides, all of which is dissipated through turbulence and friction in the boundary layers at the coastal or deep ocean. The coastal ocean acquires a significant portion of the dissipated energy (2.5 TW), where the rest (0.9 TW) is spent in the deep ocean and at ridges. The remaining energy required for the deep ocean mixing will be provided by winds through wind-ocean interaction and eddy formation. The 1 TW dissipation of tidal energy in the deep ocean is confirmed by Egbert and Ray [2000] and Egbert and Ray [2001] using the six years of TOPEX/Poseidon satellite altimeter data, while it is not clear what portion is dedicated to IWs. Considering an average value of 0.0025 and 0.03 m/s for C_d and u, the total bottom friction ($C_d \rho u^3$) is equal to 0.03 TW [St. Laurent and Garrett, 2002]. On the other hand, Egbert and Ray [2000] and Egbert and Ray [2001] calculated the energy conversion near the oceanic islands of Micronesia-Melanesia and Hawaii to be about 100 and 20 GW. Therefore, it is of importance to study the BT to BC energy conversion and

its propagation as IWs in the ocean.

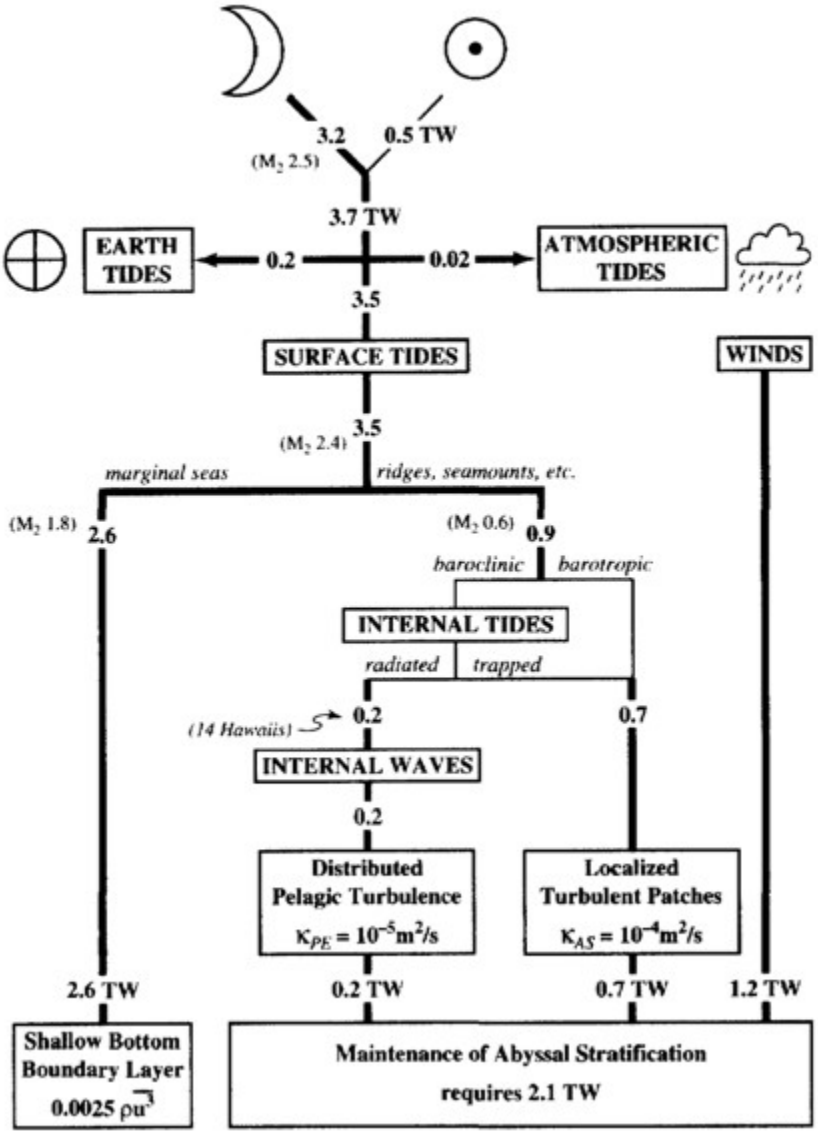

Figure 3.1: Global energy budget adopted from Munk and Wunsch [1998]

3.1 Governing Equations & Operators

I start the derivation by stating the governing equations of ocean as well as the boundary conditions and defining some of the operators which are necessary for the process. The conservation of momentum and continuity equations under the Boussinesq and incompressibility approximations are as below.

$$\begin{cases} \boldsymbol{\nabla}.\mathbf{u} = 0 \\ \frac{\partial u}{\partial t} + (\mathbf{u}.\boldsymbol{\nabla})u - fv = -\frac{1}{\rho_0}\frac{\partial P}{\partial x} + \boldsymbol{\nabla}.(\nu_h \boldsymbol{\nabla}_h u) + \frac{\partial}{\partial z}(\nu_v \frac{\partial u}{\partial z}) \\ \frac{\partial v}{\partial t} + (\mathbf{u}.\boldsymbol{\nabla})v + fu = -\frac{1}{\rho_0}\frac{\partial P}{\partial y} + \boldsymbol{\nabla}.(\nu_h \boldsymbol{\nabla}_h v) + \frac{\partial}{\partial z}(\nu_v \frac{\partial v}{\partial z}) \\ \frac{\partial w}{\partial t} + (\mathbf{u}.\boldsymbol{\nabla})w = -\frac{1}{\rho_0}\frac{\partial P}{\partial z} + \boldsymbol{\nabla}.(\nu_h \boldsymbol{\nabla}_h w) + \frac{\partial}{\partial z}(\nu_v \frac{\partial w}{\partial z}) - g\frac{\rho}{\rho_0} \end{cases} \tag{3.1}$$

where f, ν_h and ν_v are Coriolis parameter, horizontal and vertical eddy viscosities respectively. Note that the ν_h isn't solely due to turbulence and this parameterization does not violate the isotropic turbulence. The approximation of turbulence process in diffusion depends on the scale of the grid; therefore, the ν_h and ν_v are not of equal order of magnitude (as the vertical and horizontal resolution is usually the same in models). Pressure and density are partitioned into reference, background and perturbation components (P_0, P_b, P', ρ_0, ρ_b and ρ'). Also, the velocities are decomposed into BT and BC components:

$$\begin{cases} \rho = \rho_0 + \rho_b + \rho' \\ P = P_0 + P_b + P' = g\int_z^\eta \rho_0 + \rho_b(z') + \rho'(z')\mathrm{d}z' \\ \mathbf{U_h} = \frac{1}{H}\int_{-d}^{\eta} \mathbf{u_h}\mathrm{d}z \rightarrow \mathbf{U_h} = \frac{1}{H}\overline{\mathbf{u_h}} \\ \mathbf{u}' = \mathbf{u} - \mathbf{U} \end{cases} \tag{3.2}$$

where the h subscript denotes the horizontal ($[x, y], [u, v]$), $H = \eta + d$ is the water column depth (η and $-d$ are sea surface height and ocean bottom respectively), the bar operator provides the depth-integrated value of a parameter ($\bar{\phi} = \int_{-d}^{\eta} \phi \mathrm{d}z$) and capital letter velocities (U and V) are the BT components, while the prime velocities (u' and v') are the BC constituents.

3.2 The hydrostatic (LSY) method

In the absence of nonlinear effects and vertical acceleration, the governing equations can be simplified [Llewellyn Smith and Young, 2002] (hereafter the LSY method). Although this method is primitive and simple, it can be useful for many cases as the advection terms are negligible. Moreover, Kelly et al. [2010] uses this formulation along with pressure decomposition to filter the residual conversion; therefore, I review its derivation briefly (for more information refer to Llewellyn Smith and Young [2002], Kelly and Nash [2010] and Kelly et al. [2010]). This method assumptions are as follows: 1) the conservation equations can be simplified to hydrostatic if $\omega \ll N$, 2) the nonlinear advection terms can be dismissed if the tidal excursion parameter $\frac{U_0}{\omega L} \ll 1$, 3) the topography is weak meaning that the scale of topography variation is much less than wave vertical scale, and 4) all

viscous forces are discarded. Using these assumptions, equation set 3.1 becomes:

$$\begin{cases} \boldsymbol{\nabla}.\mathbf{u} = 0 \\ \frac{\partial u}{\partial t} - fv = -\frac{1}{\rho_0}\frac{\partial P}{\partial x} \\ \frac{\partial v}{\partial t} + fu = -\frac{1}{\rho_0}\frac{\partial P}{\partial y} \\ 0 = -\frac{1}{\rho_0}\frac{\partial P}{\partial z} - \frac{\rho}{\rho_0}g \\ \frac{\partial b}{\partial t} + wN^2 = 0 \end{cases} \tag{3.3}$$

where $b = -\frac{\rho}{\rho_0}g$ is the buoyancy. By enforcing the boundary conditions $w(x, y, z = 0, t) = 0$ and $w(x, y, z = -H, t) = \mathbf{U}.\boldsymbol{\nabla}H$, Llewellyn Smith and Young [2002] derived the energy budget equation as below.

$$\frac{\partial E}{\partial t} + \boldsymbol{\nabla}.\mathbf{J} = 0 \tag{3.4}$$

where $E = 1/2\rho_0(u^2 + v^2 + N^2b^2)$ and $J = \rho_0 P(u, v, w)$ are energy density and flux. The tidally-averaged conversion rate can be obtained as below.

$$C \equiv \rho_0\langle P_B\mathbf{U}.\boldsymbol{\nabla}H\rangle \tag{3.5}$$

where P_B is the pressure at the bottom. Kelly et al. [2010] decomposed the conversion induced by incoherent(remotely generated perturbations) and coherent (local ones) using $P' = P - \overline{P}$ instead of P_B. The result of this method is compared with two other methods (described in the following sections) in chapter 4 for several simulations.

3.3 Conversion Rate Using CBD Method

The CBD method, which uses a constant density background (regarding time), is a well-known method to calculate the conversion rate. Here, I briefly derive the formulation and refer the readers for more information to Kang [2010].

To derive the formulation, in addition to the governing equation set 3.1, the boundary conditions are needed. The kinematic boundary condition at the ocean surface and bottom require the water particles to move with the interface (no separation). Therefore, the fluid velocity will be tangent to the interface plane. The no-slip condition requires the velocity to be zero at the ocean bottom. The friction exerted at the ocean bottom should be considered as a dynamic boundary condition (disregarding the wind shear stress for now). The velocity flux condition at the ocean bottom $\iiint_V \boldsymbol{\nabla}.\mathbf{u_h}\mathrm{d}V = \iiint_V -\frac{\partial w}{\partial z}\mathrm{d}V$ is equal to $\oiint \mathbf{n}.\mathbf{u_H}\mathrm{d}S$ using the Gauss's theorem and continuity equation.

$$\begin{cases} \frac{\partial H}{\partial t} + \mathbf{u_H}.\boldsymbol{\nabla_h}\eta = w & \text{at } z = \eta \\ -\mathbf{u_H}.\boldsymbol{\nabla_h}d = w & \text{at } z = -d \\ \nu_v \frac{\partial u}{\partial z} = C_d u|\mathbf{u_h}| & \text{at } z = -d \\ \nu_v \frac{\partial v}{\partial z} = C_d v|\mathbf{u_h}| & \text{at } z = -d \\ \nu_v \frac{\partial w}{\partial z} = C_d w|\mathbf{u_h}| & \text{at } z = -d \end{cases} \tag{3.6}$$

where C_d is the ocean bottom drag coefficient. The BT and BC vertical velocities (W and w') are defined in a way to satisfy the continuity equation as well as

boundary conditions above.

$$\begin{cases} \frac{\partial U}{\partial x} + \frac{\partial V}{\partial y} + \frac{\partial W}{\partial z} = 0 \\ \frac{\partial u'}{\partial x} + \frac{\partial v'}{\partial y} + \frac{\partial w'}{\partial z} = 0 \\ \frac{\partial \eta}{\partial t} + \mathbf{U_h}.\boldsymbol{\nabla_h}\eta = W \qquad \text{at } z = \eta \\ -\mathbf{U_h}.\boldsymbol{\nabla_h} d = W \qquad \text{at } z = -d \\ \mathbf{u'_h}.\boldsymbol{\nabla_h}\eta = w' \qquad \text{at } z = -d \\ -\mathbf{u'_h}.\boldsymbol{\nabla_h} d = w' \qquad \text{at } z = -d \end{cases} \tag{3.7}$$

We can obtain the W and w' by depth-integrating continuity equation and using boundary conditions above.

$$\frac{\partial W}{\partial z} = -\frac{\partial U}{\partial x} - \frac{\partial V}{\partial y} \rightarrow W|_{z'} = \int_{-d}^{z'} \frac{\partial W}{\partial z}\mathrm{d}z + W|_{-d} = \int_{-d}^{z'} -\frac{\partial U}{\partial x} - \frac{\partial V}{\partial y}\mathrm{d}z$$
$$+ W|_{-d} \rightarrow W|_{z'} = -\mathbf{U_h}.\boldsymbol{\nabla_h} d + \int_{-d}^{z'} -\frac{\partial U}{\partial x} - \frac{\partial V}{\partial y}\mathrm{d}z = -\boldsymbol{\nabla}.\Big((z+d)\mathbf{U_h}\Big) \tag{3.8}$$

3.3.1 Kinetic Energy

In this subsection, I briefly review the derivation of kinetic energy equation which is adopted from Kang [2010]. The kinetic energy ($\frac{1}{2}\rho\mathbf{u}.\mathbf{u}$) for a density-stratified system can be partitioned into fully BT (EK_{BT}), fully BC (EK_{BC}) and BT-BC cross-term (EK_{BT-BC}). In this derivation, the density perturbation effect is

dismissed under the Boussinesq approximation.

$$\begin{cases} EK_{BT} = \frac{1}{2}\rho_0(U^2 + V^2) \\ EK_{BC} = \frac{1}{2}\rho_0(u'^2 + v'^2 + w^2) \\ EK_{BT-BC} = \rho_0(Uu' + Vv') \end{cases} \tag{3.9}$$

To derive the total kinetic energy budget, the conservation of momentum equations should be multiplied by $\rho_0\mathbf{u}$.

$$\begin{aligned} &\frac{\partial E_k}{\partial t} + \boldsymbol{\nabla}.(\mathbf{u}E_K) + \mathbf{u_h}.\boldsymbol{\nabla}.(\rho_0 g\eta) + \boldsymbol{\nabla}.(\mathbf{u}P') = -\rho' g w + \boldsymbol{\nabla}_\mathbf{h}.(\nu_h \boldsymbol{\nabla}_\mathbf{h} E_k) \\ &+ \frac{\partial}{\partial z}(\nu_v \frac{\partial E_K}{\partial z}) - \epsilon \\ &\epsilon = \rho_0 \nu_h \boldsymbol{\nabla}_\mathbf{h}\mathbf{u}.\boldsymbol{\nabla}_\mathbf{h}\mathbf{u} + \rho_0 \nu_v \frac{\partial \mathbf{u}}{\partial z}.\frac{\partial \mathbf{u}}{\partial z} \end{aligned} \tag{3.10}$$

The BT kinetic energy can be found by taking depth-average of equation 3.10.

$$\frac{\partial U}{\partial t} + \mathbf{U_h}.\boldsymbol{\nabla}.U + A_x - fV = -g\frac{\partial \eta}{\partial x} - \overline{\frac{1}{\rho_0 H}\frac{\partial P'}{\partial x}} + \nu_h \boldsymbol{\nabla}_\mathbf{h}.\boldsymbol{\nabla}_\mathbf{h} U - F_x - D_x \tag{3.11}$$

$$\begin{aligned} A_x &= \frac{1}{H}\boldsymbol{\nabla}_\mathbf{h}.(\overline{\mathbf{u}'P'}) \\ D_x &= \frac{C_D}{H}|\mathbf{u_h}|u \quad \text{at } z = -d \\ F_x &= \frac{\nu_h}{H}[u'\frac{\partial^2 \eta}{\partial^2 x} + 2\frac{\partial u'}{\partial x}\frac{\partial \eta}{\partial x}]|_\eta + \frac{\nu_h}{H}[u'\frac{\partial^2 \eta}{\partial^2 x} + 2\frac{\partial u'}{\partial x}\frac{\partial \eta}{\partial x}]|_{-d} + \frac{\nu_h}{H}[u'\frac{\partial^2 \eta}{\partial^2 y} + 2\frac{\partial u'}{\partial y}\frac{\partial \eta}{\partial y}]|_\eta \\ &+ \frac{\nu_h}{H}[u'\frac{\partial^2 \eta}{\partial^2 y} + 2\frac{\partial u'}{\partial y}\frac{\partial \eta}{\partial y}]|_{-d} \end{aligned}$$

$$\frac{\partial V}{\partial t} + \mathbf{U_h}.\boldsymbol{\nabla}.V + A_y + fU = -g\frac{\partial \eta}{\partial y} - \overline{\frac{1}{\rho_0 H}\frac{\partial P'}{\partial y}} + \nu_h \boldsymbol{\nabla}_\mathbf{h}.\boldsymbol{\nabla}_\mathbf{h} V - F_y - D_y \tag{3.12}$$

$$A_y = \frac{1}{H}\boldsymbol{\nabla}_\mathbf{h}.(\overline{\mathbf{u}'P'})$$

$$D_y = \frac{C_D}{H}|\mathbf{u_h}|v \quad \text{at } z = -d$$

$$F_y = \frac{\nu_h}{H}[v'\frac{\partial^2 \eta}{\partial^2 x} + 2\frac{\partial v'}{\partial x}\frac{\partial \eta}{\partial x}]|_\eta + \frac{\nu_h}{H}[v'\frac{\partial^2 \eta}{\partial^2 x} + 2\frac{\partial v'}{\partial x}\frac{\partial \eta}{\partial x}]|_{-d} + \frac{\nu_h}{H}[v'\frac{\partial^2 \eta}{\partial^2 y} + 2\frac{\partial v'}{\partial y}\frac{\partial \eta}{\partial y}]|_\eta$$
$$+ \frac{\nu_h}{H}[v'\frac{\partial^2 \eta}{\partial^2 y} + 2\frac{\partial v'}{\partial y}\frac{\partial \eta}{\partial y}]|_{-d}$$

By multiplying $\rho_0 \mathbf{U_h}$ into the equations above we can obtain the BT kinetic energy

$$\frac{\partial EK_{BT}}{\partial t} + \mathbf{U_h}.\boldsymbol{\nabla}.EK_{BT} + \mathbf{U_h}.\boldsymbol{\nabla}_\mathbf{h}(\rho_0 g\eta) + \frac{1}{H}\boldsymbol{\nabla}_\mathbf{h}.(U_h\overline{P'}) = -\frac{1}{H}\overline{\rho' g W} - \epsilon_{BT}$$
$$- \rho_0(UA_x + VA_y + UF_x + VF_Y + UD_x + VD_y) + \boldsymbol{\nabla}.(\nu_h \boldsymbol{\nabla} EK_{BT}) \tag{3.13}$$

$$\epsilon_{BT} = \rho_0 \nu_h(\boldsymbol{\nabla} U_h.\boldsymbol{\nabla} U_h)$$

Also, we can find the BC components of conservation of momentum by removing the equation 3.11 and 3.12 from the equation 3.1.

$$\frac{\partial u'}{\partial t} + \mathbf{u}'.\boldsymbol{\nabla}.u' + \mathbf{u}'_\mathbf{h}.\boldsymbol{\nabla}_\mathbf{h}.U - A_x - fv' + \frac{1}{\rho_0}\frac{\partial P'}{\partial x} = \overline{\frac{1}{\rho_0 H}\frac{\partial P'}{\partial x}} + \nu_h \boldsymbol{\nabla}_\mathbf{h}.\boldsymbol{\nabla}_\mathbf{h} u'$$
$$+ F_x + D_x \tag{3.14}$$

$$\frac{\partial v'}{\partial t} + \mathbf{u}'.\boldsymbol{\nabla}.v' + \mathbf{u}'_{\mathbf{h}}.\boldsymbol{\nabla}_{\mathbf{h}}.V - A_x + fu' + \frac{1}{\rho_0}\frac{\partial P'}{\partial y} = \overline{\frac{1}{\rho_0 H}\frac{\partial P'}{\partial y}} + \nu_h \boldsymbol{\nabla}_{\mathbf{h}}.\boldsymbol{\nabla}_{\mathbf{h}} v'$$
$$+ F_y + D_y \tag{3.15}$$

By multiplying $\rho_0 u'$, $\rho_0 v'$ and $\rho_0 w$ into equation 3.14, 3.15 and conservation of momentum in z direction and depth-integrating it, we get the EK_{BC}.

$$\frac{\partial \overline{EK_{BC}}}{\partial t} + \boldsymbol{\nabla}_{\mathbf{h}}.(\overline{\mathbf{u}_{\mathbf{h}} EK_{BC}}) + \boldsymbol{\nabla}_{\mathbf{h}}.(\overline{\mathbf{u}'_{\mathbf{h}} EK_{BT-BC}}) + \boldsymbol{\nabla}_{\mathbf{h}}.(\overline{\mathbf{u}'_{\mathbf{h}} P'}) = \overline{-\rho' g w'} + A_h$$
$$+ \overline{\boldsymbol{\nabla}_{\mathbf{h}}.(\nu_h \boldsymbol{\nabla}_{\mathbf{h}} EK_{BC})} - D_{BC} - \epsilon_{BC} \tag{3.16}$$
$$D_{BC} = \rho_0 C_d |\mathbf{u}_{\mathbf{h}}|(u'u + v'v + w^2) \quad \text{at } z = -d$$
$$\epsilon_{BC} = \rho_0 \left(\nu_h (\boldsymbol{\nabla}_{\mathbf{h}} \mathbf{u}'_{\mathbf{h}}.\boldsymbol{\nabla}_{\mathbf{h}} \mathbf{u}'_{\mathbf{h}}) + \nu_v (\frac{\partial \mathbf{u}'_{\mathbf{h}}}{\partial z}.\frac{\partial \mathbf{u}'_{\mathbf{h}}}{\partial z}) + \nu_h (\boldsymbol{\nabla}_{\mathbf{h}} w.\boldsymbol{\nabla}_{\mathbf{h}} w) + \nu_v (\frac{\partial w}{\partial z}.\frac{\partial w}{\partial z}) \right)$$
$$A_h = \rho_0 H (U\frac{\partial A}{\partial x} + V\frac{\partial A}{\partial y})$$

It should be noted that EK_{BT-BC} is skipped as $\overline{Uu'} = \overline{Vv'} = 0$.

3.3.2 Potential Energy

For an incompressible density-stratified fluid, the available potential energy (E_A) is equal to the difference between the potential energy of the perturbed water column (E_P) and the minimum energy attainable thorough adiabatic motion (E_B) [Lorenz, 1955, Winters et al., 1995].

$$E_A = E_P - E_B = \int_{z-\delta}^{z} [\rho(z) - \rho_b(z') - \rho_0] \, \mathrm{d}z' \tag{3.17}$$

The E_A budget can be found as below.

$$\frac{DE_A}{Dt} = \frac{\partial E_A}{\partial t} + \frac{\partial (uE_A)}{\partial x} + \frac{\partial (vE_A)}{\partial y} + \frac{\partial (wE_A)}{\partial z} = \frac{\partial E_A}{\partial t} + u\frac{\partial E_A}{\partial x} + v\frac{\partial E_A}{\partial y}$$
$$+ w\frac{\partial E_A}{\partial z} + E_A(\frac{\partial u}{\partial x} + \frac{\partial v}{\partial y} + \frac{\partial w}{\partial z}) \rightarrow$$
$$\frac{DE_A}{Dt} = \frac{\partial E_A}{\partial t} + u\frac{\partial E_A}{\partial x} + v\frac{\partial E_A}{\partial y} + w\frac{\partial E_A}{\partial z} = +\frac{\partial [g\delta(\rho(z) - \rho_0)]}{\partial t}$$
$$- \frac{\partial [g\int_{z-\delta}^{z} \rho_b(z')\mathrm{d}z']}{\partial t} + u\frac{\partial [g\delta(\rho(z) - \rho_0)]}{\partial x} - u\frac{\partial [g\int_{z-\delta}^{z} \rho_b(z')\mathrm{d}z']}{\partial x}$$
$$+ v\frac{\partial [g\delta(\rho(z) - \rho_0)]}{\partial y} - v\frac{\partial [g\int_{z-\delta}^{z} \rho_b(z')\mathrm{d}z']}{\partial y} + w\frac{\partial [g\delta(\rho(z) - \rho_0)]}{\partial z}$$
$$- w\frac{\partial [g\int_{z-\delta}^{z} \rho_b(z')\mathrm{d}z']}{\partial z} \rightarrow \frac{DE_A}{Dt} = g\Bigg[\Big(\rho(z) - \rho_0\Big)\frac{\partial \delta}{\partial t} + \delta\frac{\partial \rho(z)}{\partial t}$$
$$- \Bigg(- \frac{\partial (z-\delta)}{\partial t}\rho_b(z-\delta) + \int_{z-\delta}^{z} \frac{\partial \rho_b(z')}{\partial t}\mathrm{d}z'\Bigg)\Bigg]$$
$$+ gu\Bigg[\Big(\rho(z) - \rho_0\Big)\frac{\partial \delta}{\partial x} + \delta\frac{\partial \rho(z)}{\partial x} - \Bigg(- \frac{\partial (z-\delta)}{\partial x}\rho_b(z-\delta) + \int_{z-\delta}^{z} \frac{\partial \rho_b(z')}{\partial x}\mathrm{d}z'\Bigg)\Bigg]$$
$$+ gv\Bigg[\Big(\rho(z) - \rho_0\Big)\frac{\partial \delta}{\partial y} + \delta\frac{\partial \rho(z)}{\partial y} - \Bigg(- \frac{\partial (z-\delta)}{\partial y}\rho_b(z-\delta) + \int_{z-\delta}^{z} \frac{\partial \rho_b(z')}{\partial y}\mathrm{d}z'\Bigg)\Bigg]$$
$$+ gw\Bigg[\Big(\rho(z) - \rho_0\Big)\frac{\partial \delta}{\partial z} + \delta\frac{\partial \rho(z)}{\partial z} - \Bigg(\frac{\partial z}{\partial z}\rho_b(z) - \frac{\partial (z-\delta)}{\partial z}\rho_b(z-\delta)$$
$$+ \int_{z-\delta}^{z} \frac{\partial \rho_b(z')}{\partial z}\mathrm{d}z'\Bigg)\Bigg] = g\Big(\rho(z) - \rho_0\Big)\Big(\frac{\partial \delta}{\partial t} + u\frac{\partial \delta}{\partial x} + v\frac{\partial \delta}{\partial y} + w\frac{\partial \delta}{\partial z}\Big) + g\delta\Big(\frac{\partial \rho(z)}{\partial t}$$
$$+ u\frac{\partial \rho(z)}{\partial x} + v\frac{\partial \rho(z)}{\partial y} + w\frac{\partial \rho(z)}{\partial z}\Big) - g\rho_b(z-\delta)\Big(\frac{\partial \delta}{\partial t} + u\frac{\partial \delta}{\partial x} + v\frac{\partial \delta}{\partial y} + w\frac{\partial \delta}{\partial z} - w\Big)$$
$$- gw\rho_b - g\int_{z-\delta}^{z} \frac{\partial \rho_b(z')}{\partial t}\mathrm{d}z' - gu\int_{z-\delta}^{z} \frac{\partial \rho_b(z')}{\partial x}\mathrm{d}z' - gv\int_{z-\delta}^{z} \frac{\partial \rho_b(z')}{\partial y}\mathrm{d}z' \qquad (3.18)$$

By discarding the spatiotemporal variation of ρ_b, considering the material derivative (equation 3.19) and density transport (equation 3.20), equation 3.18 can be

simplified even further.

$$\frac{\partial \delta}{\partial t} + u\frac{\partial \delta}{\partial x} + v\frac{\partial \delta}{\partial y} + w\frac{\partial \delta}{\partial z} = w \tag{3.19}$$

$$\frac{\partial \rho}{\partial t} + \vec{u}.\vec{\boldsymbol{\nabla}}\rho = \frac{\partial(\kappa_H \frac{\partial \rho}{\partial x})}{\partial x} + \frac{\partial(\kappa_H \frac{\partial \rho}{\partial y})}{\partial y} + \frac{\partial(\kappa_V \frac{\partial \rho}{\partial z})}{\partial z} \tag{3.20}$$

$$\begin{aligned}
&\frac{DE_A}{Dt} = g\Big(\rho(z) - \rho_0\Big)\left(\frac{\partial \delta}{\partial t} + u\frac{\partial \delta}{\partial x} + v\frac{\partial \delta}{\partial y} + w\frac{\partial \delta}{\partial z}\right) - gw\rho_b(z) \\
&- g\int_{z-\delta}^{z} \frac{\partial \rho_b(z')}{\partial t}\mathrm{d}z' - g\rho_b(z-\delta)\left(\frac{\partial \delta}{\partial t} + u\frac{\partial \delta}{\partial x} + v\frac{\partial \delta}{\partial y} + w\frac{\partial \delta}{\partial z} - w\right) \\
&+ g\delta\left(\frac{\partial(\kappa_H \frac{\partial \rho}{\partial x})}{\partial x} + \frac{\partial(\kappa_H \frac{\partial \rho}{\partial y})}{\partial y} + \frac{\partial(\kappa_V \frac{\partial \rho}{\partial z})}{\partial z}\right) \rightarrow \\
&\frac{DE_A}{Dt} = g\Big(\rho(z) - \rho_0\Big)w - gw\rho_b(z) + g\delta\left(\frac{\partial(\kappa_H \frac{\partial \rho}{\partial x})}{\partial x} + \frac{\partial(\kappa_H \frac{\partial \rho}{\partial y})}{\partial y} + \frac{\partial(\kappa_V \frac{\partial \rho}{\partial z})}{\partial z}\right) \\
&\rightarrow \frac{\partial E_A}{\partial t} + u\frac{\partial E_A}{\partial x} + v\frac{\partial E_A}{\partial y} + w\frac{\partial E_A}{\partial z} = g\rho' w + \text{Diffusion} \\
&\text{Diffusion} = g\delta\left(\frac{\partial(\kappa_H \frac{\partial \rho}{\partial x})}{\partial x} + \frac{\partial(\kappa_H \frac{\partial \rho}{\partial y})}{\partial y} + \frac{\partial(\kappa_V \frac{\partial \rho}{\partial z})}{\partial z}\right)
\end{aligned} \tag{3.21}$$

By depth-integrating the equation 3.21 over the water column depth, we get:

$$\overline{\frac{\partial E_A}{\partial t}} + \overline{u\frac{\partial E_A}{\partial x}} + \overline{v\frac{\partial E_A}{\partial y}} + \overline{w\frac{\partial E_A}{\partial z}} = \overline{gw\rho'(z)} + \overline{\text{Diffusion}} \tag{3.22}$$

Similar to what we did for E'_K, we can tidally-average E_A as below:

$$\left\langle \overline{u\frac{\partial E_A}{\partial x}} \right\rangle + \left\langle \overline{v\frac{\partial E_A}{\partial y}} \right\rangle + \left\langle \overline{w\frac{\partial E_A}{\partial z}} \right\rangle = \left\langle \overline{gw\rho'(z)} \right\rangle + \left\langle \overline{\text{Diffusion}} \right\rangle \tag{3.23}$$

By adding the baroclinic kinetic energy to available potential energy, the conversion term of $\langle \overline{g\rho' w} \rangle - \langle \overline{g\rho' w'} \rangle = \langle \overline{g\rho' W} \rangle$ is obtained.

3.4 Conversion Rate Using TVBD Method

Using a time-variant background density can be beneficial in removing the residual conversion rate throughout the domain. In this section, I adopt a similar derivation for kinetic energy as CBD method, while a different background density function is employed which varies with time and depth (does not vary in AS and XS directions). I start the derivation from equation 3.18 and keep the ρ_b temporal variation ($\frac{\partial \rho_b}{\partial t} \neq 0$). The equation 3.19 doesn't hold any longer as the vertical velocity is modified (in chapter 4 I show that $\delta = w'$ instead of w). I

exploit the definition of APE where $\rho_b(z-\delta)=\rho(z)-\rho_0$ to simplify the TVBD.

$$\frac{DE_A}{Dt}=g\bigg(\rho(z)-\rho_0\bigg)\bigg(\frac{\partial\delta}{\partial t}+u\frac{\partial\delta}{\partial x}+v\frac{\partial\delta}{\partial y}+w\frac{\partial\delta}{\partial z}\bigg)-gw\rho_b(z)-g\int_{z-\delta}^{z}\frac{\partial\rho_b(z')}{\partial t}\mathrm{d}z'$$
$$-g\rho_b(z-\delta)\bigg(\frac{\partial\delta}{\partial t}+u\frac{\partial\delta}{\partial x}+v\frac{\partial\delta}{\partial y}+w\frac{\partial\delta}{\partial z}-w\bigg)+\text{Diffusion}\rightarrow$$
$$\frac{DE_A}{Dt}=g\bigg(\rho(z)-\rho_0\bigg)\bigg(\frac{\partial\delta}{\partial t}+u\frac{\partial\delta}{\partial x}+v\frac{\partial\delta}{\partial y}+w\frac{\partial\delta}{\partial z}\bigg)-gw\rho_b(z)-g\int_{z-\delta}^{z}\frac{\partial\rho_b(z')}{\partial t}\mathrm{d}z'$$
$$-g\bigg(\rho(z)-\rho_0\bigg)\bigg(\frac{\partial\delta}{\partial t}+u\frac{\partial\delta}{\partial x}+v\frac{\partial\delta}{\partial y}+w\frac{\partial\delta}{\partial z}-w\bigg)+\text{Diffusion}\rightarrow$$
$$\frac{DE_A}{Dt}=g\bigg(\rho(z)-\rho_0\bigg)w-g\rho_b(z)w-g\int_{z-\delta}^{z}\frac{\partial\rho_b(z')}{\partial t}\mathrm{d}z'+\text{Diffusion}$$
$$\frac{DE_A}{Dt}=g\rho' w-g\int_{z-\delta}^{z}\frac{\partial\rho_b(z')}{\partial t}\mathrm{d}z'+\text{Diffusion} \tag{3.24}$$

Similar to CBD, we need to tidally-average and depth-integrate the equation 3.24.

$$\bigg\langle\overline{u\frac{\partial E_A}{\partial x}}\bigg\rangle+\bigg\langle\overline{v\frac{\partial E_A}{\partial y}}\bigg\rangle+\bigg\langle\overline{w\frac{\partial E_A}{\partial z}}\bigg\rangle=\bigg\langle\overline{gw\rho'(z)}\bigg\rangle-\bigg\langle\overline{g\int_{z-\delta}^{z}\frac{\partial\rho_b(z')}{\partial t}\mathrm{d}z'}\bigg\rangle$$
$$+\bigg\langle\overline{\text{Diffusion}}\bigg\rangle \tag{3.25}$$

By adding the BC kinetic energy to available potential energy, the conversion term is obtained $\langle\overline{g\rho' w}\rangle-\langle\overline{g\rho' w'}\rangle-\langle\overline{g\int_{z-\delta}^{z}\frac{\partial\rho_b(z')}{\partial t}\mathrm{d}z'}\rangle=\langle\overline{g\rho' W}\rangle-\langle\overline{g\int_{z-\delta}^{z}\frac{\partial\rho_b(z')}{\partial t}\mathrm{d}z'}\rangle$.

To derive equation 3.25, no specific assumption was made regarding the variation of background density ρ_b with time nor depth (any arbitrary function of z and t can be assigned to it). To remove the barotropic tidal heaving (BTH), $\rho_b(z-\gamma)$ should be used instead of $\rho_b(z)$ in which $\gamma(x,y,z,t)$ is the barotropic

vertical displacement in a system with flat bathymetry as:

$$\frac{\partial U}{\partial x}+\frac{\partial V}{\partial y}+\frac{\partial W}{\partial z}=0\rightarrow\int_{-d}^{z}\frac{\partial U}{\partial x}+\frac{\partial V}{\partial y}\mathrm{d}z=-\int_{-d}^{z}\frac{\partial W}{\partial z}\mathrm{d}z\rightarrow$$

$$(z+d)(\frac{\partial U}{\partial x}+\frac{\partial V}{\partial y})=W_{bottom}-W=-\mathbf{U_h}.\boldsymbol{\nabla}.d-W=-W$$

$$\text{if } z=\eta\rightarrow-H(\boldsymbol{\nabla}_\mathbf{h}.\mathbf{U_h})=-W_{surface}=-\frac{\partial\eta}{\partial t}\rightarrow\frac{W}{\frac{\partial\eta(x,y,t)}{\partial t}}=\frac{H-z}{H}\rightarrow$$

$$\gamma(x,y,z,t)=\eta(1-\frac{z}{H}) \tag{3.26}$$

Chapter 4

CONVERSION RATE CALCULATION USING TVBD METHOD[1]

Chapter Overview

Internal wave (IW) generation is fundamentally the conversion (C) of barotropic (BT) to baroclinic energy (BC) that often occurs due to vertical acceleration of stratified flows over topographic features. This acceleration results in a phase lag between density (or pressure) perturbation and BT velocity. To estimate C, the density perturbation is typically calculated using a constant background den-

[1]S. Omidvar, M. Davoodi, and C.B. Woodson. Accounting for Residual Barotropic to Baroclinic Energy Conversion Using A Time-Varying Background Density. To be submitted to *Journal of Fluid Mechanics*.

sity (CBD). However, isopycnals move up and down with tides through BT tidal heaving (BTH). The failure of CBD to account for BTH leads to 1) presence of residual elements in the conversion time-series with a tidal average of zero, 2) non-zero conversion over flat bottoms, and 3) an overestimation of C at the sloped topography which is compensated by negative conversion away from the generation site. Such issues impair the efficiency of a detailed investigation of C and IW generation through time. Several studies attempted to decompose and filter the incoherent residual conversion. However, decomposition of pressure perturbation is not trivial. Here, I offer a new analytical approach to calculate the conversion rate based on a time-varying background density (TVBD) formulation to remove BTH. I show that the TVBD method results are in good agreement with the previous methods for all cases, and the tidally-averaged domain-integrated value of C is similar for all methods. This spatiotemporal comparison demonstrates the utility of TVBD over previous methods as it removes the residual conversion directly. Moreover, unlike some previous formulations, the TVBD method is not limited to linear hydrostatic inviscid IWs.

4.1 Introduction

IWs are ubiquitous features of the ocean that can affect circulation and biology by dissipating tidal energy in the deep ocean, increasing nutrient concentrations in the shallow coastal ocean, delivering larval to shore, and dispersing chemicals [Boehm et al., 2002, Garrett and Munk, 1979, L. Shanks and G. Wright, 1987,

Leichter et al., 1996, Munk and Wunsch, 1998, Pineda, 1991, Woodson, 2018]. IWs, particularly internal tides, are often generated through the vertical acceleration of tidal currents over sloping bathymetry (i.e., ridges or continental shelf breaks) causing vertical displacements of isopycnals [Baines, 1974, Bell, 1975, Holloway and Merrifield, 1999, Klymak et al., 2006, Merrifield and Holloway, 2002, Rattray Jr., 1960]. Movements of isopycnals in the form of IWs are known throughout the world's oceans and are suspected to be the major contributors to ocean energy budgets [Egbert and Ray, 2000, Munk and Wunsch, 1998]. IWs can balance ocean energy budgets by dissipating up to 30% of tidal energy in the deep ocean [Egbert and Ray, 2001, Munk and Wunsch, 1998]. Consequently, the dynamics behind IW generation and propagation have received considerable focus over the past several decades [Baines, 1982, Bell, 1975, Rattray Jr., 1960].

To quantify IW generation, the conversion rate of BT to BC energy is often used as a proxy [Kang and Fringer, 2010, 2012, Lamb, 2007, Lien et al., 2014, Merrifield et al., 2001, Moum et al., 2007, Palmer et al., 2015, Venayagamoorthy and Fringer, 2005]. The conversion rate depends on the pressure (or density) perturbation, BT velocity, and the bathymetric slope. In the absence of a sloped ocean bottom, BT tidal currents can still affect the density structure through barotropic tidal heaving (BTH) without converting any energy (Fig 4.1) [Lu et al., 2001]. Although taking a time-average of C over a tidal cycle can remove such an effect and is efficient in studying the energy budget [Kang and Fringer, 2012, Müller, 2013]; it fails to provide any insight on the evolution of BT to BC energy conversion through time. Moreover, reflected IWs from ocean bottom and surface

can propagate toward coastal oceans. The observations confirm the presence of remotely incoherent IWs in coastal regions accompanied by the ones generated locally [Kelly and Nash, 2010, Nash et al., 2012, Nash, J.D., E.L. Shroyer, S.M. Kelly, M.E. Inall, T.F. Duda, M.D. Levine, N.L. Jones and Musgrave, 2012, Pickering et al., 2015, Zilberman et al., 2011]. In addition to conversion observed by local IWs, the interaction of incoherent IWs with BTH can create positive and negative conversion. If remotely generated IWs are phase-locked to the surface tides, they affect the time-averaged conversion, while ones with a random phase (in comparison to surface tides) only alter the instantaneous IW generation and energy budget [Kelly and Nash, 2010]. This interaction can also occur at the generation site, which results in overestimation or underestimation of energy conversion. To remedy these issues, I chose to account for the effect of BTH in density perturbation, while Kelly et al. [2010] recognizes and decomposes the incoherent part. Therefore, it is of importance to recognize and partition the density and pressure perturbation effectively to remove the unwanted conversion induced by remotely generated IWs. I call such unwanted conversion elements (overestimation-underestimation at the generation site, non-zero conversion away from the generation site and extra negative-positive constituents in the conversion time-series with the time-average value of zero) "residual" as they are residual to the main conversion.

To calculate BT to BC energy conversion, Llewellyn Smith and Young [2002] discarded the nonlinear advection and dissipation terms in the Boussinesq momentum equations which resulted in $C = \vec{\nabla} H.Up'|_{z=-H}$ (hereinafter the LSY

method). The LSY method is well-known and has been widely used in the literature [Carter et al., 2008, Gerkema et al., 2004, Kelly and Nash, 2010, Kelly et al., 2010, Kurapov et al., 2003, Pickering et al., 2015]. To filter the residual conversion, Lu et al. [2001], Kunze et al. [2002], and Zilberman et al. [2011] used an approximation for linear IW potential energy and removed the BT vertical displacement caused by surface tides over a sloped topography as approximated by Baines [1982]. In another effort, Pollmann et al. [2019] proposed a semi-analytical method that gives a positive definite conversion field for linear IWs over a subcritical bathymetry through spatial smoothing.

In all of these efforts to decompose and filter the residual component of C, the nonlinear advection terms are disregarded (in some cases, diffusion-dissipation is also neglected), which limits the scope to linear IWs. Moreover, filtering the isopycnal vertical displacement creates an extra cross-term in the potential energy budget, which should be considered. Here, I improve the formulation offered by Kang and Fringer [2012] $C = \rho' g W$ (hereinafter the KF method) by decomposing and removing the BTH effects using a time-variant background density (TVBD) instead of a constant background density (CBD). Unlike the LSY formulation, which is limited to inviscid linear IWs, this method takes into account the nonlinear advection and dissipation terms as well as the non-hydrostatic pressure [Kang and Fringer, 2012]. This implementation results in removing the negative conversion rate by discarding the BTH contribution as well as removing the effect of IW reflection (from ocean bottom and surface) on the conversion rate. The concept of TVBD has been previously applied to study mixing [Dossmann et al., 2017, Mac-

Cready and Giddings, 2016], but has not been used to study the IW conversion and filter barotropic tidal heaving (BTH) of isopycnals. I develop the theoretical framework (section 2), outline the numerical model setup (section 3), discuss the application of the theoretical framework and interpret the results (section 4), and conclude the paper with a summary (section 5).

4.2 Theoretical framework

I start our derivation from conservation of mass and momentum:

$$\begin{cases} \boldsymbol{\nabla}.\mathbf{u} = 0 \\ \frac{\partial u}{\partial t} + (\mathbf{u}.\boldsymbol{\nabla})u - fv = -\frac{1}{\rho_0}\frac{\partial P}{\partial x} + \boldsymbol{\nabla}.(\nu_h \boldsymbol{\nabla}_h u) + \frac{\partial}{\partial z}(\nu_v \frac{\partial u}{\partial z}) \\ \frac{\partial v}{\partial t} + (\mathbf{u}.\boldsymbol{\nabla})v + fu = -\frac{1}{\rho_0}\frac{\partial P}{\partial y} + \boldsymbol{\nabla}.(\nu_h \boldsymbol{\nabla}_h v) + \frac{\partial}{\partial z}(\nu_v \frac{\partial v}{\partial z}) \\ \frac{\partial w}{\partial t} + (\mathbf{u}.\boldsymbol{\nabla})w = -\frac{1}{\rho_0}\frac{\partial P}{\partial z} + \boldsymbol{\nabla}.(\nu_h \boldsymbol{\nabla}_h w) + \frac{\partial}{\partial z}(\nu_v \frac{\partial w}{\partial z}) - g\frac{\rho}{\rho_0} \end{cases} \tag{4.1}$$

where f, ν_h and ν_v are Coriolis parameter, and the horizontal and vertical eddy viscosities respectively. Pressure and density are partitioned into reference, background and perturbation components (P_0, P_b, P', ρ_0, ρ_b and ρ'). Also, the veloc-

ities are decomposed into BT and BC components:

$$\begin{cases} \rho = \rho_0 + \rho_b + \rho' \\ P = P_0 + P_b + P' = g\int_z^\eta \rho_0 + \rho_b(z') + \rho'(z')\mathrm{d}z' \\ \mathbf{U_h} = \frac{1}{H}\int_{-d}^{\eta} \mathbf{u_h}\mathrm{d}z \rightarrow \mathbf{U_h} = \frac{1}{H}\overline{\mathbf{u_h}} \\ \mathbf{u'} = \mathbf{u} - \mathbf{U} \\ \boldsymbol{\nabla}.\mathbf{U} = 0 \\ \boldsymbol{\nabla}.\mathbf{u'} = 0 \end{cases} \tag{4.2}$$

where the h subscript denotes the horizontal ($[x, y], [u, v]$), $H = \eta + d$ is the water column depth (η and $-d$ are sea surface height and ocean bottom respectively), the bar operator provides the depth-integrated value of a parameter ($\bar{\phi} = \int_{-d}^{\eta} \phi \mathrm{d}z$) and capital letter velocities (U and V) are the BT components, while the prime velocities (u' and v') are the BC constituents. I define BT and BC vertical velocities to satisfy the conservation of mass $W = -\boldsymbol{\nabla}_h.[\mathbf{U}_h(d + z)]$ and $W + w' = w$.

By using the momentum equations and applying boundary conditions (full derivation is provided in Kang [2010]), we get the depth-integrated BC kinetic energy (E'_K) budget:

$$\begin{aligned} &\frac{\partial \overline{E'_K}}{\partial t} + \boldsymbol{\nabla}_\mathbf{h}.(\overline{\mathbf{u_h} E'_k}) + \boldsymbol{\nabla}_\mathbf{h}.(\overline{\mathbf{u'_h} EK_{BT-BC}}) = -\boldsymbol{\nabla}_\mathbf{h}.(\overline{\mathbf{u'_h} P'}) - \overline{\rho' g w'} + A_h \\ &+ \overline{\boldsymbol{\nabla}_\mathbf{h}.(\nu_H \boldsymbol{\nabla}_\mathbf{h} E'_K)} - D' - \overline{\epsilon_K} \end{aligned} \tag{4.3}$$

For an incompressible density-stratified fluid, the available potential energy (E_A) is equal to the difference between the potential energy of the perturbed water

column (E_P) and the minimum energy attainable thorough adiabatic motion (E_B) [Lorenz, 1955, Winters et al., 1995]. The concept of E_A has been widely used to study energy budgets in both deep and shallow water systems [Kang and Fringer, 2010, 2012, Klymak et al., 2006, Scotti et al., 2006, Venayagamoorthy and Fringer, 2005]. For any arbitrary density stratification, E_A can be found from [Kang and Fringer, 2010, 2012]:

$$E_A = E_P - E_B = \int_{z-\delta}^{z} [\rho(z) - \rho_b(z') - \rho_0] \, \mathrm{d}z' \tag{4.4}$$

For linear IWs in a linear density-stratified media E_A can further be approximated as [Gill, 1982, Lamb, 2007, Scotti et al., 2006]:

$$E_A = \frac{\rho_0}{2} N^2 \delta^2 = \frac{g^2 \rho'^2}{2\rho_0 N^2} \tag{4.5}$$

The E_A inside a system can be dissipated, advected or converted to kinetic energy (disregarding the spatiotemporal background density variation $\frac{\partial \rho_b}{\partial x}, \frac{\partial \rho_b}{\partial y}, \frac{\partial \rho_b}{\partial t} \approx 0$):

$$\overline{\frac{\partial E_A}{\partial t}} + \overline{\mathbf{u}.\boldsymbol{\nabla} E_A} = \overline{gw\rho'(z)} + \overline{\epsilon_A} \tag{4.6}$$

By adding 4.3 and 4.6 and tidally-averaging, we get:

$$\boldsymbol{\nabla}_\mathbf{h}.\left\langle \overline{\mathbf{u}.\boldsymbol{\nabla} E_A} + \overline{\mathbf{u_h} E'_k} + \overline{\mathbf{u'_h} EK_{BT-BC}} + \overline{\mathbf{u'_h} P'} - \overline{\nu_H \boldsymbol{\nabla}_\mathbf{h} E'_K} \right\rangle = \langle \overline{\rho' g w} - \overline{\rho' g w'} \rangle$$
$$+ \langle A_h \rangle - \langle D' \rangle + \langle \overline{\epsilon_A - \epsilon_K} \rangle \tag{4.7}$$

where the angled bracket operator provides the tidal-averaged value of a parameter ($\langle\phi\rangle = \frac{1}{T}\int_0^T \phi \mathrm{d}t$). Therefore, the total conversion from BT to BC energy is equal to $\langle \mathrm{Conversion}_{\mathrm{Potential}}\rangle + \langle \mathrm{Conversion}_{\mathrm{Kinetic}}\rangle = \langle\overline{g\rho' w}\rangle - \langle\overline{g\rho' w'}\rangle = \langle\overline{g\rho' W}\rangle = \langle\overline{C}\rangle$ [Kang and Fringer, 2012], where C consists of actual and residual conversion. BTH of isopycnals alone (without the presence of a sloped bottom) does not generate IWs nor convert energy from BT to BC; yet, the vertical acceleration over sloped bathymetry causes a phase lag between the density perturbation and the vertical velocity ($\overbrace{\rho', W}$ where the over-brace operator denotes the phase difference). The conversion by such a phase lag can be understood considering two idealized sinusoidal functions assigned to ρ' and W with period, amplitude and initial-phase of ω, a, b:

$$\langle C\rangle = \langle \rho' g W\rangle = g\left\langle a_i \sin(\omega t + b_i) a_j \sin(\omega t + b_j)\right\rangle = g\frac{a_i a_j}{2}\cos\left(\overbrace{b_i, b_j}\right) \tag{4.8}$$

Equation 4.8 leads to positive conversion rates for phase differences less than 90°, while for values greater than 90°, a negative conversion rate is observed [Zilberman et al., 2009].

To better understand the role of BTH in conversion, assume a system governed by tidal flows with a flat bathymetry in which isopycnals heave up (down) during flood (ebb) tides. In such a system, although no IW is generated, there are non-zero density perturbations and BT vertical velocities through time (red curves in Fig 4.1-c and d). Therefore, due to the failure of BTH filtering we get a non-zero C with a zero tidal-averaged value (red curve in Fig 4.1-f) which is fully BT (Fig 4.1-e) and have $\overbrace{W, \rho'} = 90°$. By applying a proper time-varying ρ_b, the BT

displacement of the background density can be removed (blue curve in Fig 4.1-f).

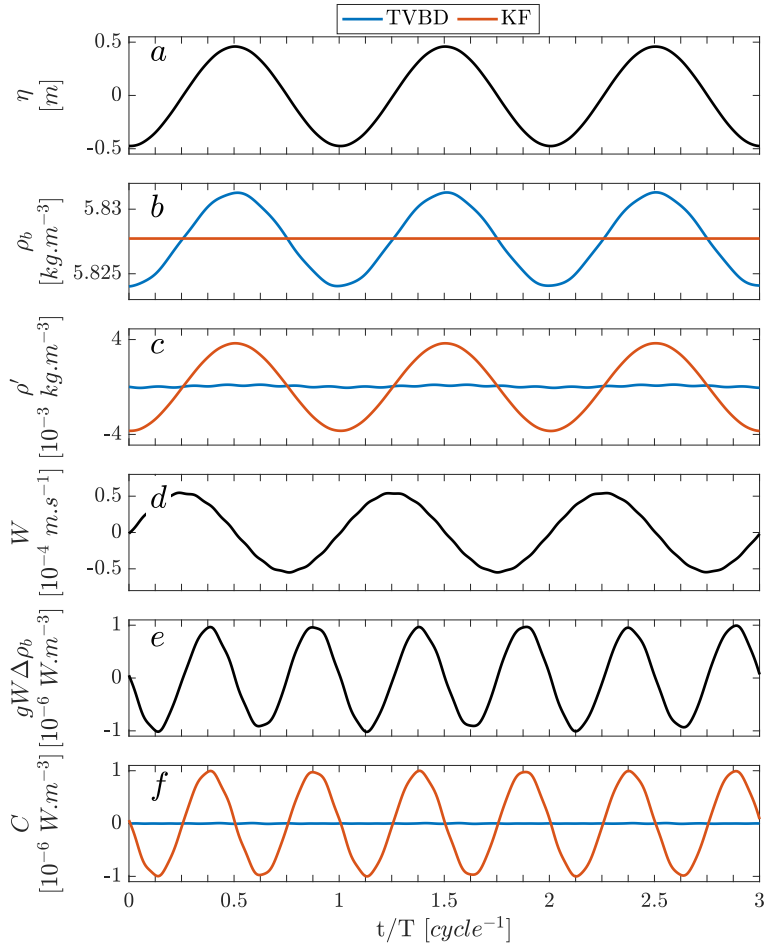

Figure 4.1: Data at X=99.5 km and Z=-50.8 m for a system with flat bathymetry (Case 1). Rows show tidal height, background density, density perturbation, barotropic vertical velocity, barotropic conversion rate and conversion rate from top to bottom.

In CBD methods (both LSY and KF), ρ_b is only a function of z; while in TVBD, ρ_b is a function of z and t. The temporal dependency of ρ_b creates a new cross-term in the E_A budget which can be beneficial in removing any arbitrary chosen vertical displacement (similar methodology used by Kunze et al. [2002], Lu

et al. [2001], Zilberman et al. [2011]). By removing the barotropic displacement at any depth we can filter the effects of BTH. To do so, I removed the barotropic displacement of isopycnals due solely to BTH $\gamma(x,y,z,t) = \eta(1-\frac{z}{H})$; while, Lu et al. [2001] removed the effect of flow acceleration over a slopped bottom as well (refer to equation 3.26 for the complete derivation). As it is discussed in section 4 (interpretation), this temporal cross-term is a critical component that can remove the interaction of IWs and BTH; therefore, I call it $IW \times BTH$ where $\times$ represents the interaction. It should be noted that the presence of nonlinear advection terms in the E_A budget is necessary and their pivotal contribution in the formation of $\rho' g W$ is acknowledged by Kang and Fringer [2012]. The E_A budget in the TVBD method is shown as below:

$$\overline{\frac{\partial E_A}{\partial t}} + \overline{\mathbf{u}.\boldsymbol{\nabla} E'_K} = \overline{\rho' g w} - \overline{g \int_{z-\delta}^{z} \frac{\partial \rho_b(z',t)}{\partial t} \mathrm{d}z'} + \overline{\epsilon_A} \tag{4.9}$$

The total energy budget (kinetic+potential), where $\left\langle \overline{\rho' g W - g \int_{z-\delta}^{z} \frac{\partial \rho_b(z',t)}{\partial t} \mathrm{d}z'} \right\rangle$ is the modified conversion, then becomes:

$$\begin{aligned} &\boldsymbol{\nabla}_{\mathbf{h}}.\left\langle \overline{\mathbf{u}.\boldsymbol{\nabla} E_A} + \overline{\mathbf{u}_{\mathbf{h}} E'_k} + \overline{\mathbf{u}'_{\mathbf{h}} E K_{BT-BC}} + \overline{\mathbf{u}'_{\mathbf{h}} P'} - \overline{\nu_H \boldsymbol{\nabla}_{\mathbf{h}} E'_K} \right\rangle = \\ &\left\langle \overline{\rho' g W - g \int_{z-\delta}^{z} \frac{\partial \rho_b(z',t)}{\partial t} \mathrm{d}z'} \right\rangle + \langle A_h \rangle - \langle D' \rangle + \langle \overline{\epsilon_A - \epsilon_K} \rangle \end{aligned} \tag{4.10}$$

This formulation is similar to the KF method with the addition of the $IW \times BTH$ cross-term.

4.3 Numerical Setup

To test the efficiency and validity of TVBD and the its effects on C, I simulated and analyzed IW generation on two 2-dimensional shelf slopes (Fig 4.5) as well as a three-dimensional ridge (Fig 4.2). For numerical simulations, I employed SUNTANS (Stanford Unstructured Non-hydrostatic Terrain following Averaged Navier-Stokes Simulator). SUNTANS is a finite volume model that solves three-dimensional non-hydrostatic, nonlinear Navier-Stokes equations and supports unstructured-triangular horizontal grids and z-level vertical layers [Fringer et al., 2006]. SUNTANS has been wildly used to study non-hydrostatic nonlinear phenomena such as IWs and circulation in shallow coastal systems and estuaries [Jachec et al., 2007, Kang and Fringer, 2012, Nelko et al., 2014, Xu and Chua, 2016, Zhang et al., 2011]. Realistic geographical features can cause complex circulation, currents and waves, which complicate the analysis. To avoid such complications, I started our analysis with two idealized 2-dimensional cases with high spatiotemporal resolution. Moreover, to validate the formulation in a more realistic setup, I compared the results for an idealized 3-dimensional ridge.

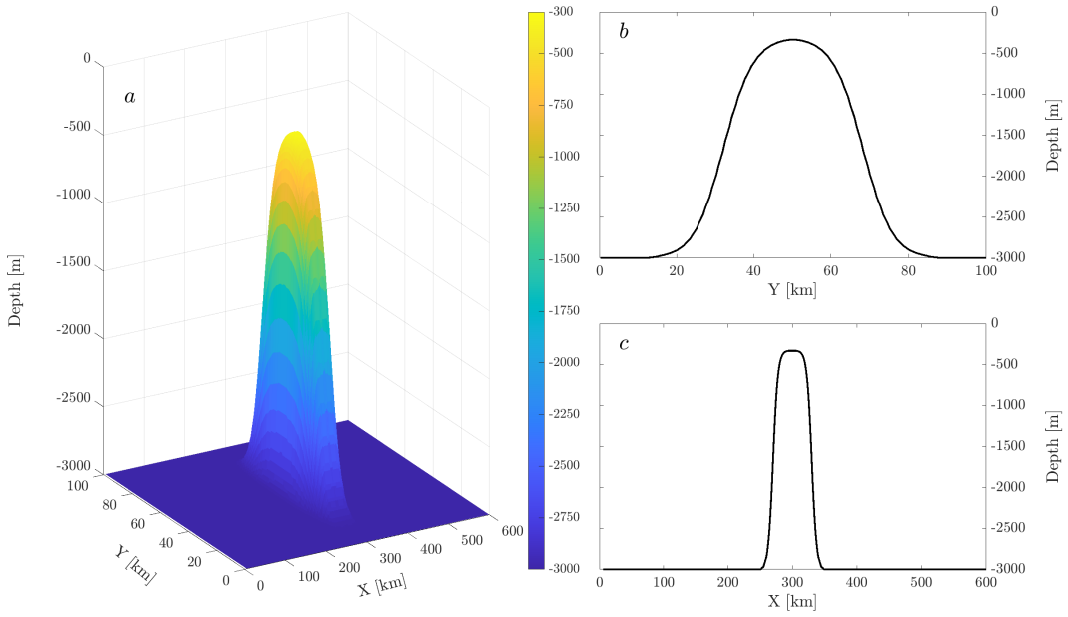

Figure 4.2: Ideal ridge bathymetry map (case 4) is shown in a with the maximum and minimum depth of 3000 and 300 meters. The transects at X= 300 km and Y= 50 km are shown in panel b and c respectively.

A bottom drag coefficient of 0.005 is used to simulate the effect of bottom friction. To avoid numerical oscillations, background values for ν_H and ν_V were applied (Table. 4.1) in addition to Mellor-Yamada 2.5 turbulence closure scheme. To analyze the effect of depth (shallow vs deep) on C, I used idealized density stratification functions (Fig 4.3) and bathymetries:

$$d = H - 0.5(H_0 - h_0)\left[1 + \tanh\left(\frac{x - X_{mid}}{L_s}\right)\right] \tag{4.11}$$

where h_0 and H_0 are minimum and maximum depth in the domain, d is the depth at any specific point, X_{mid} and L_s are bathymetric shape parameters (Table 4.1).

Table 4.1: Case study details show domain length (L), horizontal and temporal resolution (ΔX and Δt), number of vertical layers (N_k), minimum and maximum layer thickens (Δz_{min} and Δz_{max}), minimum and maximum bathymetry depth (h_0 and H_0), bathymetric shape constants (L_s, X_{mid}), tidal current velocity at the ocean-side boundary (U_0), maximum of the tidal height (η_{max}), sponge layer constants (L_0, L_1, α_0, α_1), horizontal and vertical eddy viscosity (ν_H and ν_V)

Case	**1**	**2**	**3**
$\boldsymbol{L}$ $[\boldsymbol{km}]$	150	400	600
$\boldsymbol{\Delta x}$ $[\boldsymbol{m}]$	30	160	300-1500
$\boldsymbol{\Delta t}$ $[\boldsymbol{s}]$	15	15	15
$\boldsymbol{N_k}$	200	400	400
$\boldsymbol{\Delta z_{min}}$, $\boldsymbol{\Delta z_{max}}$ $[\boldsymbol{m}]$	0.76, 2.6	1.7, 20.2	1.7, 20.2
$\boldsymbol{h_0}$, $\boldsymbol{H_0}$ $[\boldsymbol{m}]$	30, 300	300, 3000	300, 3000
$\boldsymbol{L_s}$ $[\boldsymbol{m}]$, $\boldsymbol{x_{mid}}$ $[\boldsymbol{km}]$	7500, 130	750, 325	750, 300
$\boldsymbol{U_0}[\frac{\boldsymbol{m}}{\boldsymbol{s}}]$	0.04	0.03	0.04
$\boldsymbol{\eta_{max}}[\boldsymbol{m}]$	0.5	1.5	1.5
$\boldsymbol{L_0}$, $\boldsymbol{L_1}$ $[\boldsymbol{km}]$	10, 5	25, 30	30, 30
$\boldsymbol{\alpha_0}$, $\boldsymbol{\alpha_1}$ $[\boldsymbol{km}]$	3.2, 0.8	4.2, 0.8	0.8, 0.8
$\boldsymbol{\nu_H}$, $\boldsymbol{\nu_V}$ $[\frac{\boldsymbol{m^2}}{\boldsymbol{s}}]$	1, 10^{-3}	1, 10^{-1}	1, 10^{-1}
$\boldsymbol{\theta_B}$, $\boldsymbol{\theta_{IW}}$	0.17, 0.021	0.12, 0.046	0.18, 0.070
$\boldsymbol{\beta_1}$	8	2.6	2.58
Peak Location X[km], Z[m]	130, 156.6	330,787	269, 1699

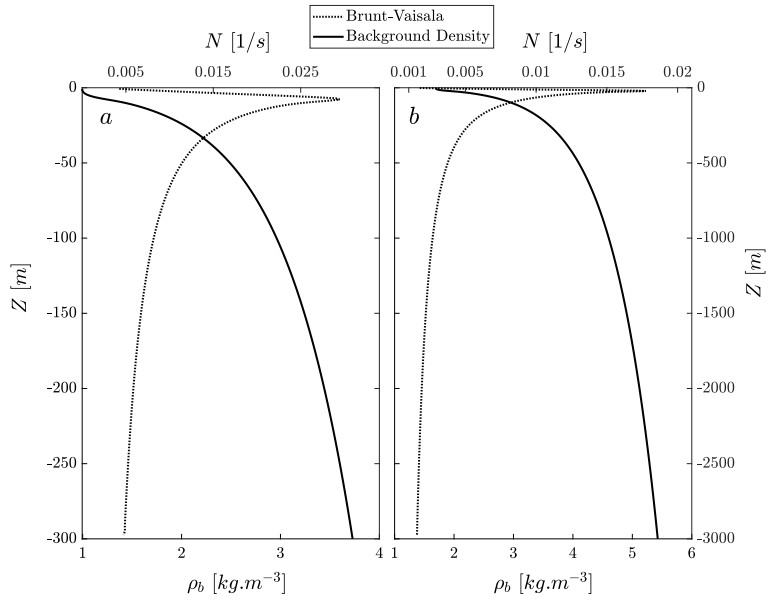

Figure 4.3: Background density and Brunt-Vaisala frequency at the beginning of last 3 tidal cycle for a) shallow (cases 1 and 2) and b) deep (cases 3 and 4)

For all cases, M2 tidal currents ($u = U_0 \sin(\omega t)$) were applied at the ocean-side boundary and the shore-side boundary was set to closed. To avoid IW reflection at boundaries, BC velocity (u') was relaxed both at the ocean-side and shore-side boundaries using a sponge layer as:

$$\begin{cases} x \geq L_0 : u = u - 0.5 * \exp\Big(-\frac{x-L_0}{\alpha_0}\Big)(u - U) \\ x < L_1 : u = u - 0.5 * \exp\Big(-\frac{L_1-x}{\alpha_1}\Big)(u - U) \end{cases} \tag{4.12}$$

where L_0, L_1, α_0 and α_1 are the sponge constants. The spatiotemporal resolution, bathymetry and sponge layer details for each case are given in Table 4.1.

I examined three case scenarios with different physical (tidal current velocity, bathymetry, eddy viscosity) and environmental parameters (domain size and spa-

tiotemporal resolution) as summarized in Table 4.1. The models ran for 15 tidal cycles and all of the analyses were performed on the last three cycles. Model setup files and analysis scripts are also available on `http://github.com/somidvar/suntans/tree/master/TVBDPaperSourceCode`.

The steepness number (β_1) and tidal excursion (β_2) are informative dimensionless numbers characterize the reflectivity and linearity of IWs:

$$\begin{cases} \tan(\theta_B) = \sqrt{(\frac{\partial d}{\partial x})^2 + (\frac{\partial d}{\partial y})^2} \\ \tan(\theta_{IW}) = \sqrt{\frac{\omega^2 - f^2}{N^2 - \omega^2}} \\ \beta_1 = \frac{\tan(\theta_B)}{\tan(\theta_{IW})} \\ \beta_2 = \frac{U_0 k_b}{\omega} \end{cases} \tag{4.13}$$

where U_0 and k_b^{-1} are the maximum BT tidal current velocity and topographic length scale. For IW studies, the k_b is estimated as $\frac{\theta_B}{H-d}$ [Garrett and Kunze, 2007, Kang and Fringer, 2012]. In a system with supercritical bathymetry ($\beta_1 > 1$), the generated IWs will reflect back offshore while for a subcritical bathymetry ($\beta_1 < 1$), the IWs continue their way into the shallower region (Fig 4.4). A tidal excursion less than one suggests that the IW frequency is similar to the forcing frequency, while $\beta_2 > 1$ gives lee waves [Kang and Fringer, 2012]. For this study, all the cases have supercritical topography ($\beta_1 > 1$) and responded mainly with the perturbation frequency ($\beta_2 < 1$). To assure a significant amount of conversion, I set our cases (Table 4.1) with $1 < \beta_1 < 5$ [Kang and Fringer, 2012]. Therefore, I expect to see the most of generated IWs reflected back offshore as IW beams. The generated IWs can clearly be seen as elevation and depression rays as they

bounce from the ocean bottom and surface (Fig 4.5).

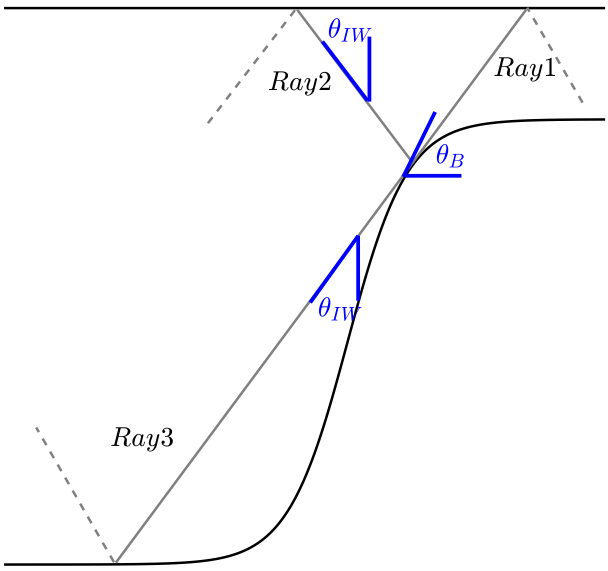

Figure 4.4: Schematic IW propagation and reflection (dashed lines) from the generation site in a system with subcritical bathymetry

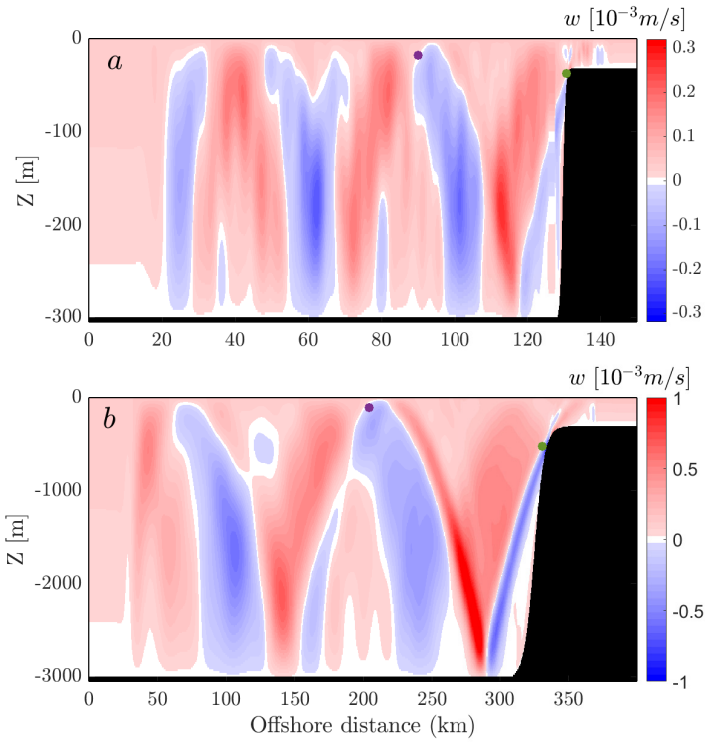

Figure 4.5: Vertical velocity at time t = 0.4 cycle for a) shallow (case 2) and b) deep (case 3). Green dot show the generation site (Fig 4.6) and purple is a sample of reflection point.

4.4 Results and Interpretation

IW generation and BT to BC conversion can be seen in Fig 4.6 to 4.7. In this part, I compare the results of the LSY and KF methods to the TVBD method and show how TVBD provides an improvement over the others by addressing the issues mentioned in section 1. To study C effectively, the residual conversion should be filtered because the residual conversion is observable as 1) the negative conversion in C time-series which is compensated by part of the positive conversion (Fig 4.8-

d, e, i and j), 2) non-zero $\langle\overline{C}\rangle$ at the flat bottom part of domain due to incoherent remotely generated IWs (Fig 4.9-a, 4.9-c and 4.7-e), and 3) the overestimation of C at generation sites (the peak of $\langle\overline{C}\rangle$ in Fig 4.10-a and c).

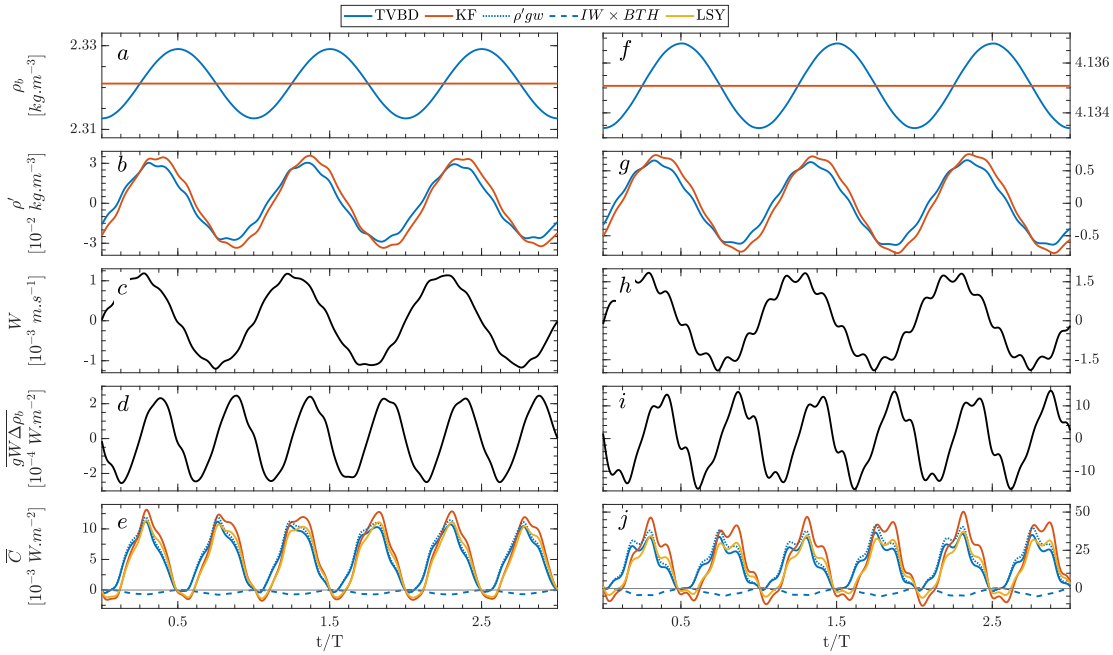

Figure 4.6: Left panel shows the data at X=130.7 km and Z=-37.4 m for case 2 and right panel is for case 3 at X=330.9 km and Z=-524 m (green dots in Fig 4.5). Rows show background density, perturbation density, barotropic vertical velocity, barotropic conversion rate and conversion rate from top to bottom

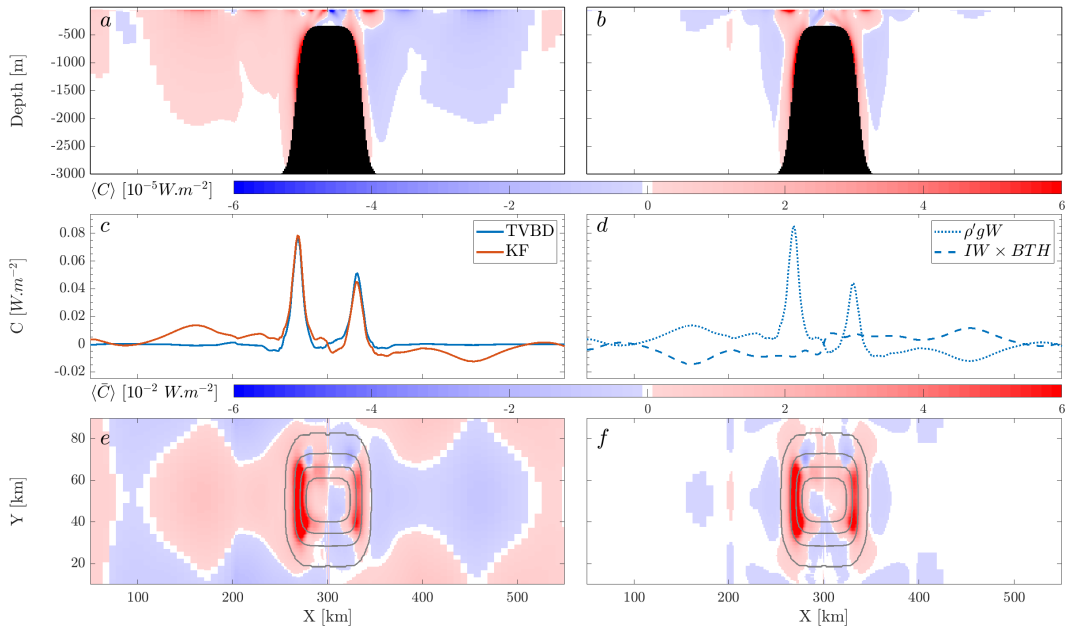

Figure 4.7: Panel a and b show the time-averaged conversion rate ($\langle C \rangle$) using KF and TVBD at the transect Y=50 km. The time-averaged depth-integrated conversion rate ($\langle \bar{C} \rangle$) at the transect Y=50 km for both method can be seen in panel c; while, the components of TVBD are shown in panel d. The time-averaged depth-integrated conversion rate for the whole domain can be seen in panels e and f using KF and TVBD respectively. Bathymetry contours are spaced at -300, -500, -1000, -2000 and 2900 meters in panels e and f.

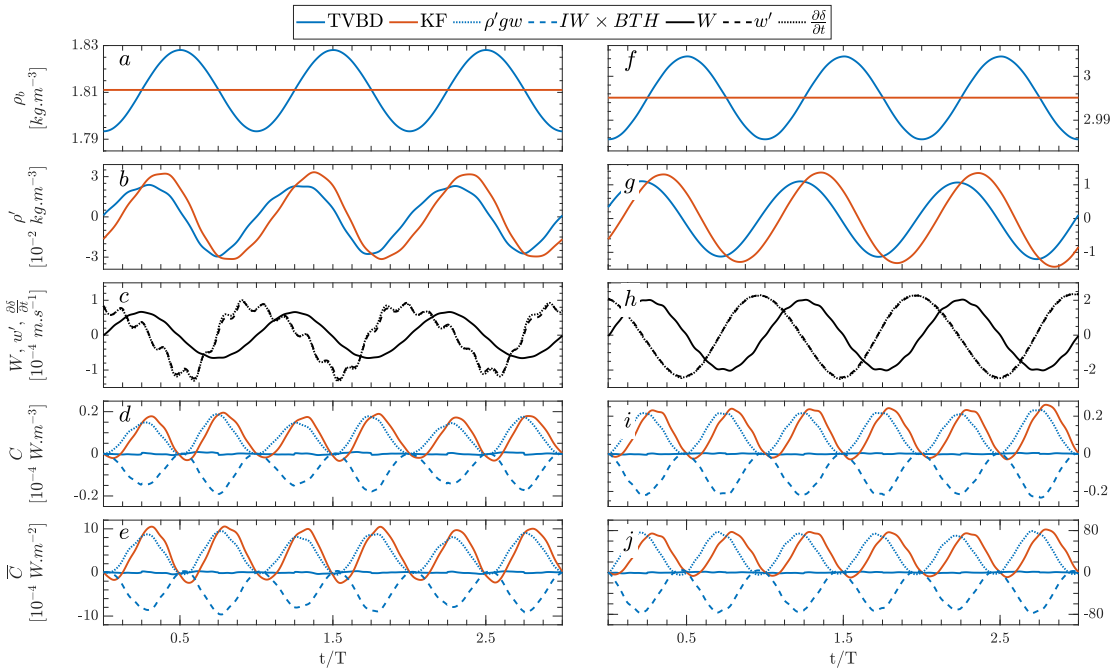

Figure 4.8: Data at a IW reflection point. Left panel shows the data at X=89.9 km and Z=-17.8 m for case 2 and right panel is for case 3 at X=203.9 km and Z=-104.8 m (purple dots in Fig 4.5). Rows show background density, perturbation density, vertical velocity (W, w' and $\frac{\partial \delta}{\partial t}$) and conversion rate from top to bottom

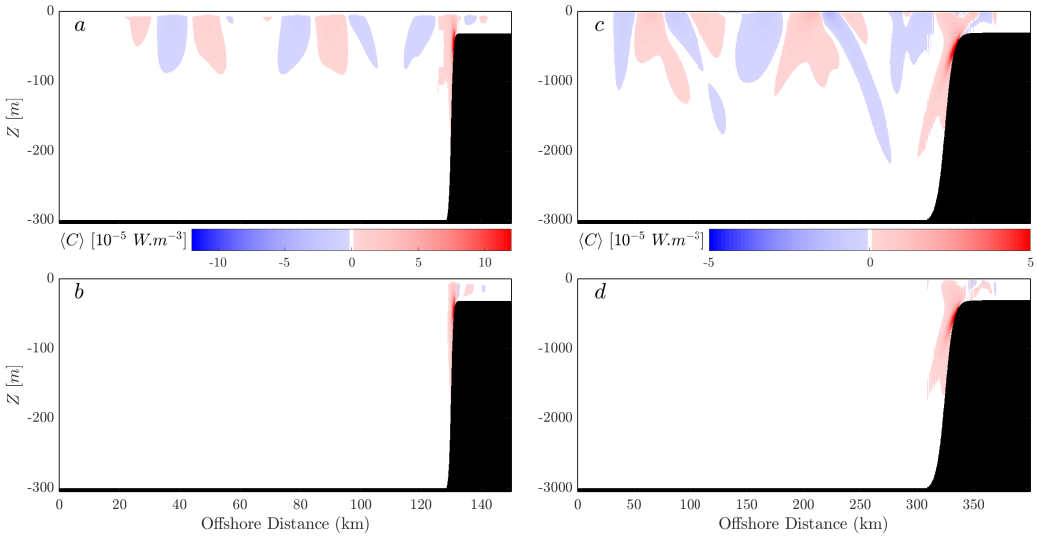

Figure 4.9: Time-averaged conversion rate ($\langle C \rangle$) for case 2 (left column) and case 3 (right column). Top row shows the result of KF method and bottom row is for TVBD.

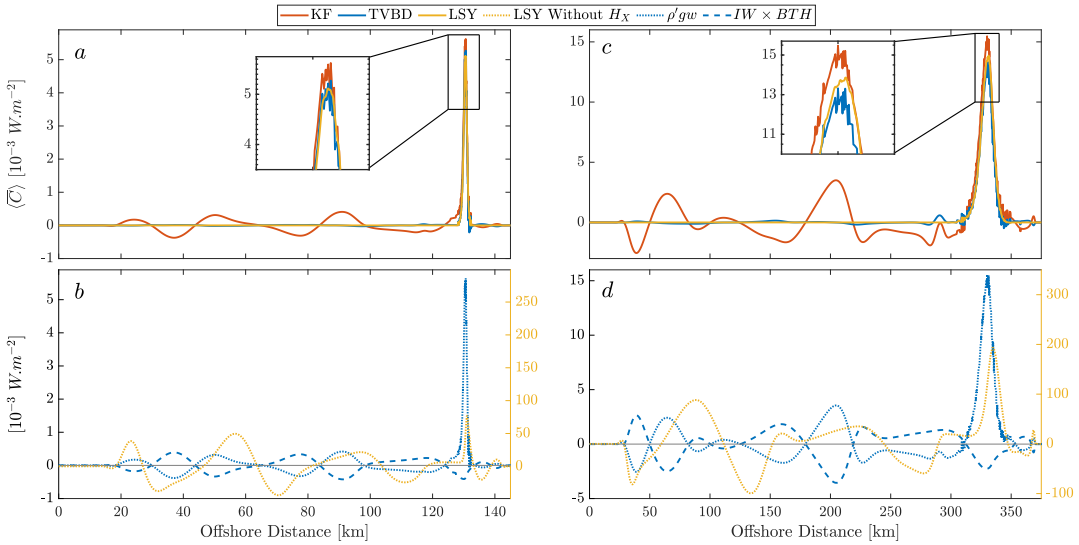

Figure 4.10: Time-averaged depth-integrated conversion rate ($\langle \bar{C} \rangle$) for KF, LSY and TVBD methods for case 2 (left column) and case 3 (right column). The top row shows the comparison between two methods and bottom row provides more details about the two terms of TVBD method as well as the LSY method results discarding the bathymetry gradient H_x.

4.4.1 Negative in C Time-series

The main difference between TVBD and CBD methods is the removal of BTH and, therefore, the $IW \times BTH$ by TVBD. Conversion is the product of W and ρ' in which the density perturbation is induced by density changes due to BTH, vertical acceleration over a sloped bathymetry, and BC oscillations. The conversion due to the unfiltered BTH which can be found by $[\rho_{b\,TVBD} - \rho_{b\,CBD}]gW$ is solely responsible for the observed differences between CBD and TVBD results as shown in Fig 4.6-d and e as well as i and j (2 and 12 $W.m^{-2}$ for shallow and deep cases respectively). Although the LSY method removes the background pressure P_b, this issue persists as it only removes the time-averaged background pressure P_b

and not the BTH. The residual conversion in the C time-series (Fig 4.6-e and j) supports this assertion.

4.4.2 Non-zero C on Flat Bottom

Away from the sloped region, especially at the reflection points, where the IWs bounce from the ocean surface and bottom, there isn't any active IW generation nor energy conversion. However, a non-zero residual C is observed due to the disturbances caused by the unfiltered BTH, which is avoided by the TVBD formulation (Fig 4.8-d and i). Similar patterns have been reported by incoherent remotely generated IWs, which are phase-locked to the surface tides by Kelly and Nash [2010], Zilberman et al. [2011], and Pickering et al. [2015]. Although BTH is fully BT (regulated symmetric sinusoidal density variation), its interaction with IWs is not, and we should seek the reason for non-zero C in the phase lag caused by the IWs. Based on Zilberman et al. [2009], the conversion rate is due to $\cos\left(\widehat{\rho', W}\right)$, which can be affected by perturbation factors such as the presence of IWs. The reflected IWs from the ocean surface and bottom (Fig 4.4) possess w' (BC perturbations) which is not in-phase with W (Fig 4.8-c and g) and therefore, altering the phase of W (Fig 4.11-b and d). The reflection of IWs adversely affects the CBD conversion calculation as it creates residual conversion (positive or negative) away from the generation sites (the alternating shading pattern can be seen in Fig 4.9). In contrast, the TVBD method removes the effects of IW reflection on C through the $IW \times BTH$ term (Fig 4.8). This issue is masked in the LSY method as it depends on the bathymetric slope, which is zero away

from the slope in this study. However, by disregarding the bathymetric slope in LSY formulation, we observe an oscillating pattern similar to the KF method as it suffers from non-zero conversion in the flat part of the domain (the yellow dot lines in Fig 4.10-b and d). Such an issue can occur in real case scenarios as the ocean bottom is not flat near the continental shelf break or ridges. This scrutiny highlights another advantage of TVBD over the LSY and KF methods as it can help differentiate between locally generated IWs and ones developed remotely.

To better understand the role of $IW \times BTH$, I decompose its tidal-average using Leibniz's integral rule, $\langle IW \times BTH \rangle = -g \int_0^T \int_{z-\delta}^{z} \frac{\partial \rho_b}{\partial t} \mathrm{d}z' \mathrm{d}t = g \int_0^T \frac{\partial \delta}{\partial t} \rho_b|_{z-\delta} \mathrm{d}t - g \int_0^T \frac{\partial}{\partial t} \int_{z-\delta}^{z} \rho_b \mathrm{d}z' \mathrm{d}t$ in which the second term is zero, while the first term shows the net conversion over a tidal cycle. In the KF's method, $\frac{\partial \delta}{\partial t} = w$; however, in the TVBD method, $\frac{\partial \delta}{\partial t} = w'$ as W is removed from w (Fig 4.8-c and g). Based on our definition of γ, it can be infered that the $\rho_b|_z$ and $\rho_b|_{z-\delta}$ are in-phase. For gravitational waves (away from their generation site), it can be shown that $\langle \overline{\rho' g W} \rangle$ and $\langle \overline{IW \times BTH} \rangle$ are at complementary angles and therefore, their cosines cancel each other [Cushman-Roisin and Beckers, 2011]:

$$
\begin{aligned}
&Phase_{\rho'} - Phase_{w'} = Phase_{\rho_b} - Phase_W = -\frac{\pi}{2} \rightarrow Phase_{\rho'} - Phase_{w'} \\
&+ Phase_{\rho_b} - Phase_W = -\pi \rightarrow \overbrace{\rho', w'} + \overbrace{\rho_b, W} = \pi
\end{aligned} \tag{4.14}
$$

Therefore, $IW \times BTH$ cancels any conversion induced by $\rho' g W$ over flat bottoms.

In a similar context, Kelly et al. [2010] made an effort to decompose and remove shoaling IWs, which resembles the role of BTH in this study. However,

this requires discerning the unwanted phenomena like shoaling IW or BTH, which is not a trivial task since its phase changes as it propagates in the system. Such a phase variation is evident as the magnitude of W and ρ' does not vary significantly on the flat bottom part of the domain; yet, there is a meaningful conversion gradient due to $\overbrace{\rho', W}$ as shown in Fig 4.10-a and c. Also, it should be noted that this decomposition is utilizing linear superposition of unwanted (shoaling) and wanted (local) phenomena, which may not hold for nonlinear cases. I conclude that although the TVBD method is computationally expensive (especially for field data), it is more convenient to remove the BTH effect versus the decomposition approach used by Kelly et al. [2010].

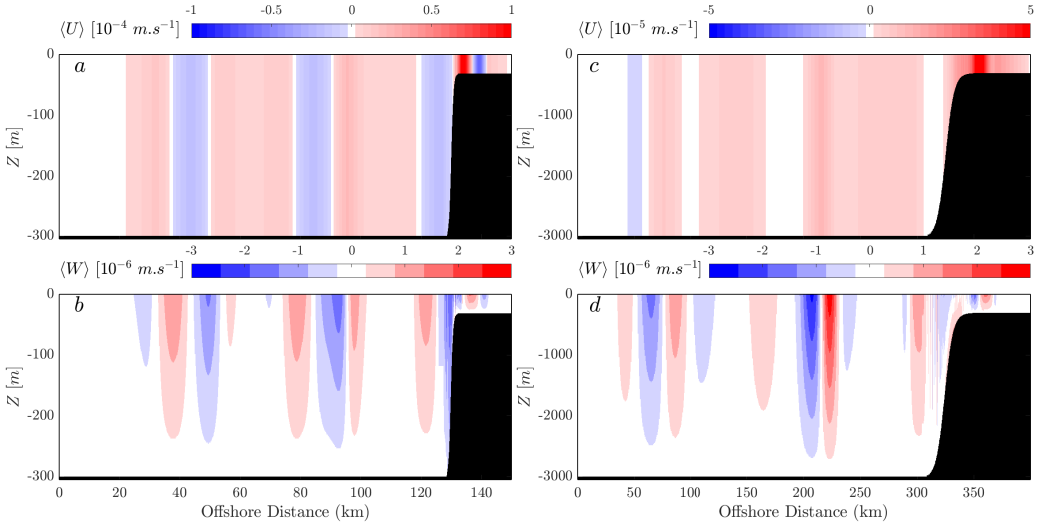

Figure 4.11: Time-averaged horizontal BT velocity $\langle U \rangle$ (top row) and time-averaged vertical BT velocity $\langle W \rangle$ (bottom row) for case 2 (left column) and case 3 (right column). Reflection points can be seen as the intensification of W in bottom panel

4.4.3 Overestimation of C at Generation Points

Although the overestimation of C at the generation points by the LSY and KF methods is minor (less than 5 and 10% respectively), I suspect that it is related to the interaction of BTH with the IWs. This overestimation is compensated by negative C away from the slope as the spatial integrals of C for LSY, KF, and TVBD methods are similar.

4.4.4 Extension to 3D Case

To test the performance of the TVBD method and its extension to a more realistic setup, I compared the CBD and TVBD results for the idealized ridge case. Similar to two-dimensional cases, a good agreement was found between CBD and TVBD patterns (Fig 4.7). In the three-dimensional case, IW reflection and the residual conversion are obvious in the KF method (Fig 4.7-a and e), which are significantly removed by the correction term of $IW \times BTH$ (Fig 4.7-b, d and f). The spatial integral of C over the whole domain of the three-dimensional ridge is equal to 66.5 and 63.5 MW for the KF and TVBD methods, respectively. The TVBD does not remove all negative values of C in the three-dimensional case, especially at the flanks of the ridge likely due to higher-order $IW \times IW$ interactions, yet there is still a significant improvement in estimates of C, especially through time as tidal-averaging is not needed. I believe that the incorporation of IW displacements as a higher-order cross-term would remove these regions of negative conversion as well.

4.5 Summary, Conclusion and Future Work

In this study, I compared BT to BC energy conversion over sloped bottoms using a new TVBD method and compared it to commonly-used methods (LSY and KF) utilizing constant background density. A portion of BT tidal energy is converted to the BC energy over sloped bathymetry due to the phase difference between the BT vertical velocity (W) and the density perturbation (ρ'). The density perturbation is the result of barotropic tidal heaving, local acceleration over the sloped bottom, and BC oscillations. The CBD methods attempt to remove the BTH effects by averaging over tidal cycles. However, these methods suffer because there are 1) residual values in C time-series, which is the interminable conversion of BT to BC and BC to BT with a net tidal-average of zero, 2) negative-positive values in $\langle\overline{C}\rangle$ away from the generation site over the flat bottom region, and 3) overestimation of the $\langle\overline{C}\rangle$ at the generation sites. The TVBD method remedies these issues in CBD methods by removing BTH directly through the new cross-term ($IW \times BTH$), which emerges in the energy budget equation due to using time-varying background density profile. $IW \times BTH$ improves discrimination between IW generation (as an active mechanism of converting BT energy to BC energy) versus incoherent propagating IWs (which are the reflection of generated IWs from ocean bottom and surface) by removing the interaction between IWs and BTH. Moreover, by removing the BTH effect, TVBD allows identification of locations with real negative conversion where the BC energy converts to BT through pressure work or topography features as well as topographies lacking conversions where IWs are generated at one location and absorbed in another one [Maas,

2011, Zilberman et al., 2009]. Removing these interactions also allows for a more efficient evaluation of BT-BC conversion over a tidal cycle, which is not possible using CBD methods since residuals are removed by tidal averaging. The numerical simulations performed in SUNTANS illustrate the improved estimation of BT-BC conversion using the TVBD method. Although the three methods mentioned in this study estimate the BT to BC energy conversion from different perspectives, the value of total conversion over the domain was similar in all of them. The results illustrate the improvement of TVBD over CBD methods; however, TVBD calculations are computationally expensive, and performing such calculations for field data can be significantly time-consuming and costly. Although I recognize the necessity to conduct further tests to study the efficiency of TVBD with nonlinear cases such as solitons, this method provides a step forward in our understanding of internal wave dynamics.

Table 4.2: Variables and symbols used in the paper

Variable	Description	Variable	Description
ρ_0, ρ_b, ρ'	Reference, background and perturbation density	f	Coriolis parameter
P_0, P_b, P'	Reference, background and perturbation pressure	C_B	Bottom drag coeff
κ_H, κ_V	Horizontal and vertical diffusion	ν_H, ν_V	Horizontal & Vertical viscosity
$\eta, -d$	Ocean surface and bottom	H	Water column depth
U, V, W	BT velocity	u', v', w'	BC velocity
E_K	Total kinetic energy	E'_K	BC Kinetic Energy
D'	Drag in kinetic energy budget	ϵ_K	BC Dissipation
ϵ_A	Diffusion in APE budget	ω	Wave frequency
$\overbrace{a, b}$	Phase difference between a and b	A_h	Unclosed term in energy budget
γ	Barotropic vertical displacement	E_P	Perturbed potential energy
E_B	Minimum potential energy	E_A	Available potential energy
$\overline{\phi}$	$\int_{-d}^{\eta} \phi \mathrm{d}z'$	$\langle\phi\rangle$	$\frac{1}{T}\int_0^T \phi \mathrm{d}t'$
θ_{IW}	IW Slope	θ_B	Bottom slope
β_2	Tidal excursion	β_1	Steepness number
δ	IW vertical displacement		

Chapter 5

TIDE-TIDE INTERACTION EFFECTS ON CONVERSION RATE IN THE NEARSHORE AREA[1]

Chapter Overview

Gravitational forces due to the sun and moon generate surface tides whose energy is ultimately dissipated in the ocean in the form of internal waves (IW)s; therefore, it is of importance to study the environmental parameters which affect their

[1]S. Omidvar, M. Fagundes and C.B. Woodson. Effects of environmental forcing on internal wave generation and conversion I: Tide-tide interactions. To be submitted to *Journal of Geophysical Research - Oceans*

generation. IWs are generated as the BT tidal flow accelerates over a sloped topography which results in a phase lag between pressure and vertical velocity. The BT to baroclinic (BC) energy conversion by M_2 tides has received considerable attention in the last century. However, the contribution of other tidal counterparts and their interactions with M_2 have been neglected. Many studies to date have focused on the continental shelf break as a more prominent location of IW generation. In this study, I focus on the IW generation and energy conversion in the nearshore area using southern Monterey Bay as a case study. Monterey Bay is a representative of a highly stratified system that experiences active surface and internal tidal waves. I included the K_1 tidal constituent and analyzed the promotion of conversion at extra frequencies generated by the interaction of M_2 and K_1. Moreover, I studied the role of pycnocline depth and M_2-K_1 phase lag on the total energy converted in the system.

5.1 Introduction

IWs are common features of the ocean [Rainville and Pinkel, 2006] that can affect biophysical processes. IWs are important for 1) dissipating the tidal energy in the deep ocean [Egbert and Ray, 2000, 2001, Munk and Wunsch, 1998], 2) enhancing turbulence diffusion and diapycnal mixing [Klymak and Moum, 2003, Palmer et al., 2015, van Haren et al., 2012, Woodson et al., 2011], 3) transporting nutrients for phytoplankton growth into coastal ocean by upwelling deeper colder nutrient-enriched water [Jantzen et al., 2013, Leichter et al., 1998, McPhee-Shaw et al.,

2007, Shea and Broenkow, 1982, Woodson, 2018], 4) increasing larval recruitment rate by onshore transport [L. Shanks and G. Wright, 1987, Pineda, 1991, 1995, Shanks, 1983, 1986], and 5) augmenting cross-shore (XS) exchange of sediment and contaminants [Boehm et al., 2002, Hosegood and Van Haren, 2004].

Vertical acceleration of tidal currents over sloped bathymetry (i.e., shelf-breaks, banks and ridges) can cause vertical displacement of isopycnals and may lead to IW generation [Baines, 1974, Bell, 1975, Rattray Jr., 1960]. IW generation is a mechanism that converts BT energy to BC mode energy [Klymak et al., 2006, Merrifield and Holloway, 2002]. Such conversion occurs due to the phase lag between density perturbation and BT vertical velocity [Zilberman et al., 2009]. Therefore, it is essential to study the parameters affecting the phasing between vertical flows and density structures.

Tidal and inertial frequencies can significantly affect the IW generation dynamics and the nature of IW propagation in a system. Tidal decomposition of sea surface gauges suggests the existence of several tidal constituents at different frequencies where the most prominent ones are M_2 (principal lunar semidiurnal) and K_1 (lunisolar diurnal). The IW dispersion relation for a rotating frame of reference requirement ($f < \omega < N$ where N and f are Brunt-Vaisala and Coriolis frequencies) holds for the super-inertial ($\omega > f$) [Cushman-Roisin and Beckers, 2011]. On the other hand, for any IW generation site located above 30° latitude, $\omega_{K1} < f$ (sub-inertial range); therefore, the generated wave propagates in the system as a trapped wave [Longuet-Higgins, 1969]. Such a trapped wave propagates as a Kelvin wave, which needs a boundary at its right in the northern hemisphere

(left in the southern one), and its amplitude exponentially decay with offshore distance. This behavior has been studied before as the diurnal wind created fluctuations around islands and density-stratified lakes [Masunaga et al., 2017, Tanaka et al., 2010].

The transferring of energy from a primary frequency (the frequency which rules the system such as M_2, K_1 or inertial) of a system to a secondary one (a new frequency which is generated as the interaction of two primaries) propagates as IWs, and BT energy conversion to turbulence and mixing have been studied before [Hibiya et al., 2002, Klymak et al., 2006, MacKinnon and Winters, 2003]. The coupling of M_2 tidal currents with the wind-induced oscillations at the inertial frequency in the coastal ocean can create new frequencies (fM_2) in the system, which are a function of M_2 and f. This nonlinear interaction gets intensified at the thermocline and is accompanied by strong shear and vertical velocity, which transfers the BT energy to higher frequency BC IWs and eventually to turbulence and mixing [Davies and Xing, 2003, Hall and Davies, 2007, Xing and Davies, 2002]. In this study, I analyze the role of K_1 tidal current in promoting the BT to BC energy conversion in the nearshore area.

5.2 Theoretical framework

The governing equations for incompressible fluid consist of continuity, mass transport and momentum conservation. Under the Boussinesq approximation:

$$\begin{cases} \boldsymbol{\nabla}.\mathbf{u} = 0 \\ \frac{\partial u}{\partial t} + (\mathbf{u}.\boldsymbol{\nabla})u - fv = -\frac{1}{\rho_0}\frac{\partial P}{\partial x} + \boldsymbol{\nabla}.(\nu_h \boldsymbol{\nabla}_h u) + \frac{\partial}{\partial z}(\nu_v \frac{\partial u}{\partial z}) \\ \frac{\partial v}{\partial t} + (\mathbf{u}.\boldsymbol{\nabla})v + fu = -\frac{1}{\rho_0}\frac{\partial P}{\partial y} + \boldsymbol{\nabla}.(\nu_h \boldsymbol{\nabla}_h v) + \frac{\partial}{\partial z}(\nu_v \frac{\partial v}{\partial z}) \\ \frac{\partial w}{\partial t} + (\mathbf{u}.\boldsymbol{\nabla})w = -\frac{1}{\rho_0}\frac{\partial P}{\partial z} + \boldsymbol{\nabla}.(\nu_h \boldsymbol{\nabla}_h w) + \frac{\partial}{\partial z}(\nu_v \frac{\partial w}{\partial z}) - g\frac{\rho}{\rho_0} \\ \frac{\partial \rho}{\partial t} + (\mathbf{u}.\boldsymbol{\nabla})\rho = \boldsymbol{\nabla}.(\kappa_h \boldsymbol{\nabla}_h \rho) + \frac{\partial}{\partial z}(\kappa_v \frac{\partial \rho}{\partial z}) \end{cases} \tag{5.1}$$

where ν_h, ν_v, κ_h and κ_v are Coriolis parameter, horizontal and vertical eddy viscosity, horizontal and vertical eddy diffusion. The pressure and density can be partitioned into reference (ρ_0 and P_0), background (ρ_b and P_b) and perturbation (ρ' and P'). Also, the velocity can be divided to BT ($\mathbf{U}$) and BC ($\mathbf{u}'$) components:

$$\begin{cases} \rho = \rho_0 + \rho_b + \rho' \\ P = P_0 + P_b + P' = g\int_z^\eta \rho_0 + \rho_b(z') + \rho'(z')\, dz' \\ \mathbf{U_h} = \frac{1}{H}\int_{-d}^{\eta} \mathbf{u_h}\, dz = \frac{1}{H}\overline{\mathbf{U_h}} \\ \mathbf{u}' = \mathbf{u} - \mathbf{U} \end{cases} \tag{5.2}$$

where η, $-d$, $H = \eta - (-d)$ are water surface elevation, ocean bottom and water column depth respectively. The bar, angled-bracket and wide-hat operators provide the depth-integrated value of a parameter ($\psi = \int_{-d}^{\eta} \mathrm{d}z$), the time-average value over a tidal cycle ($\langle\psi\rangle = \int_0^T \mathrm{d}t$ where T is the period), and spacial inte-

gral over the XS ($\widehat{\phi} = \int_0^L \phi \mathrm{d}x$) respectively. To satisfy the continuity equation, $W = -\boldsymbol{\nabla}_h.[\mathbf{U_h}(d+z)]$ where $w = W + w'$ and W and w' are BT and BC components of vertical velocity respectively.

Using these definitions, the depth-integrated time-averaged BC kinetic energy ($E'_k = \frac{1}{2}\rho_0[u'^2 + v'^2 + w^2]$) yields to [Kang, 2010]:

$$\boldsymbol{\nabla}_h.\left\langle \overline{\mathbf{u_h} E'_k} + \overline{\mathbf{u'_h}\rho_0(Uu' + Vv')} + \overline{\mathbf{u'_h} P'} \right\rangle = -\left\langle \overline{\rho' g w'} + A_h - D' - \overline{\epsilon_K} \right\rangle \tag{5.3}$$

$$\epsilon_K = \rho_0\nu_H(\boldsymbol{\nabla}_\mathbf{h}\mathbf{u'_h}.\boldsymbol{\nabla}_\mathbf{h}\mathbf{u'_h}) + \rho_0\nu_V\left(\frac{\partial \mathbf{u'_h}}{\partial z}.\frac{\partial \mathbf{u'_h}}{\partial z}\right) + \rho_0\nu_H(\boldsymbol{\nabla}_\mathbf{h} w.\boldsymbol{\nabla}_\mathbf{h} w)$$

$$+ \rho_0\nu_V\left(\frac{\partial w}{\partial z}.\frac{\partial w}{\partial z}\right) + \boldsymbol{\nabla}_\mathbf{h}.(\nu_h \boldsymbol{\nabla}_\mathbf{h} E'_k)$$

$$A_h = \rho_0\left(U\boldsymbol{\nabla}_h.(\overline{\mathbf{u'_h}u'}) + V\boldsymbol{\nabla}_h.(\overline{\mathbf{u'_h}v'})\right)$$

$$D' = \rho_0 C_B\sqrt{u^2+v^2}(u'u + v'v + w^2) \text{ at } z = -d$$

where A_h, D', C_B and ϵ_K are unclosed advection, drag energy, bottom drag coefficient and kinetic dissipation. The available potential energy (E_A) can be defined as the difference between the perturbed water column energy (E_P) and the minimum energy attainable through adiabatic motion (E_B)[Lorenz, 1955, Winters et al., 1995]. Therefore, for an incompressible density-stratified fluid $E_A = E_P - E_B = \int_{z-\delta}^{z}[\rho(z) - \rho_b(z') - \rho_0]\,\mathrm{d}z'$ where δ is the vertical displacement

induced by IWs. The E_A budget can be found as:

$$\left\langle \overline{u\frac{\partial E_A}{\partial x}} \right\rangle + \left\langle \overline{v\frac{\partial E_A}{\partial y}} \right\rangle + \left\langle \overline{w\frac{\partial E_A}{\partial z}} \right\rangle = \left\langle \overline{gw\rho'(z)} \right\rangle + \left\langle \overline{\epsilon_A} \right\rangle \tag{5.4}$$
$$\epsilon_A = g\delta\left(\frac{\partial(K_h \frac{\partial \rho}{\partial x})}{\partial x} + \frac{\partial(K_h \frac{\partial \rho}{\partial y})}{\partial y} + \frac{\partial(K_v \frac{\partial \rho}{\partial z})}{\partial z} \right)$$

where ϵ_A is diffusion term. The total BT to BC energy conversion rate can be found by adding equations 5.3 and 5.4 together: $\langle \overline{C} \rangle = \langle \overline{gw\rho'} - \overline{gw'\rho'} \rangle = \langle \overline{gW\rho'} \rangle$. To better understand the dynamic of BT to BC conversion and study the parameters which affect such a conversion, we can filter the nonlinear high-frequency IWs and assign idealized sinusoidal functions to W and ρ':

$$\begin{cases} \rho' = \sum a_i \sin(\omega_i t + b_i) + c_i + \text{ NT} \\ W = \sum a'_j \sin\big(\omega_j t + b'_j\big) + c'_j + \text{ NT} \end{cases} \tag{5.5}$$

where a_i (a'_i), b_i (b'_i) and c (c') are amplitude, initial phase and constant values of ρ' (W). NT is the nonlinear term due to the phase shift induced by tide-tide interaction which affects the conversion rate. By dismissing the NT term for now (I will analyze it in section 5.4), the total conversion rate equals:

$$C = \sum_{i=1}^{i=n} \sum_{j=1}^{j=n} [a_i \sin(\omega_i t + b_i) + c_i][a'_j \sin\big(\omega_j t + b'_j\big) + c'_j] \tag{5.6}$$

For any i and j ($\omega_i > \omega_j$), we get:

$$[a_i \sin(\omega_i t + b_i) + c_i][a'_j \sin\big(\omega_j t + b'_j\big) + c'_j] = \frac{a_i a'_j}{2}[\cos\big(\omega_i t + b_i + \omega_j t + b'_j\big)$$
$$- \cos(\omega_i t + b_i - \omega_j t - b'_k)] + c'_j a_i \sin(\omega_i t + b_i) + c_i a'_j \sin\big(\omega_j t + b'_j\big) + c_i c'_j \qquad (5.7)$$

If we choose t in a way that $t = n^{(1)}\frac{2\pi}{\omega_i} = n^{(2)}\frac{2\pi}{\omega_j} = n^{(3)}\frac{2\pi}{\omega_i+\omega_j} = n^{(4)}\frac{2\pi}{\omega_i-\omega_j}$ where $n(1)$ to $n(4)$ are integers, the tidal average value of equation 5.7 (where $i \neq j$), is zero (in the absence of active upwelling or buoyant plume $aa' \gg cc'$, so cc' is negligible in comparison to aa'). However, for $i = j$:

$$a_i a'_j \cos\big(\omega_i t + b_i - \omega_j t - b'_j\big) = a_i a'_j \cos(b_i - b'_i) = a_i a'_j \cos\left(\overbrace{\rho', W}\right) \neq 0 \qquad (5.8)$$

where $\overbrace{a, b}$ shows the phase difference between a and b (Fig 5.1). While $\langle C \rangle = \frac{a_i a'_i}{2}\cos(b_i - b'_i)$, the C time-series oscillates with the frequencies of:

$$C = f(\omega_i, \omega_j, |\omega_i - \omega_j|, \omega_i + \omega_j) \qquad (5.9)$$

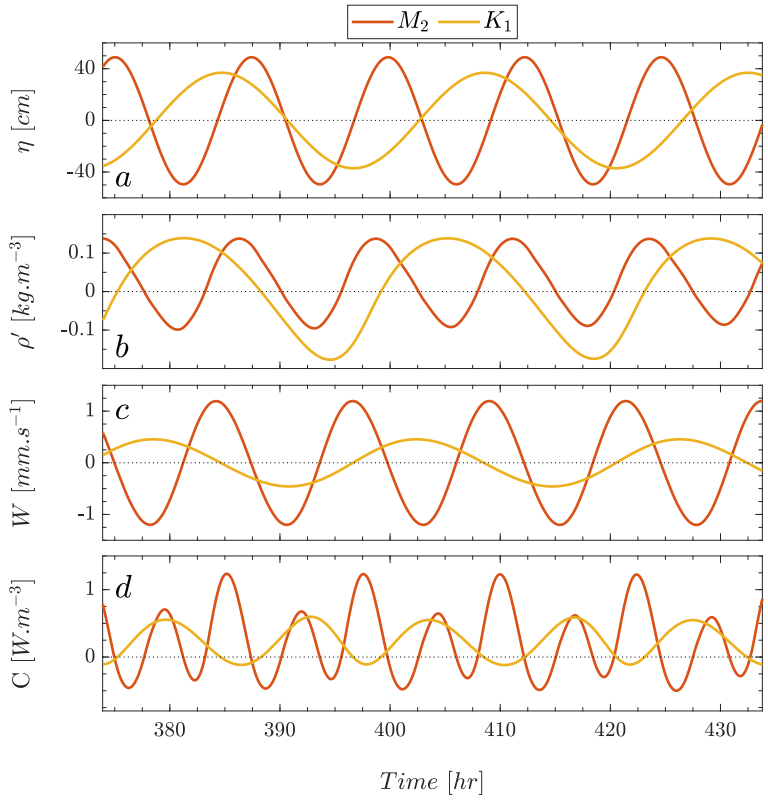

Figure 5.1: Sea surface height (η), density perturbation (ρ'), BT vertical velocity (W), and conversion rate (C) are shown at $x = 44.5$ km and $z = -9.5$ m for the last four tidal cycle of a system perturbed by M_2 tide. The phase lag between ρ' and W is creating positive net conversion rate.

5.3 Numerical Setup

To evaluate the effect of tidal phasing and assess the impact of the NT term on the conversion rate, I simulated a system perturbed by M_2 and K_1 tidal currents (as representatives of semi-diurnal and diurnal tidal constituents). Furthermore, I analyzed the role of pycnocline depth as well as the phase lag between components $(\overbrace{M_2}\ ,\ \overbrace{K_1})$ in the BT to BC conversion process.

For numerical simulations, I used SUNTANS (Stanford Unstructured Non-Hydrostatic Terrain following Averaged Navier-Stokes Simulator [Fringer et al., 2006]). SUNTANS uses a triangular horizontal grid and z-level coordinate system and has been widely used in coastal region studies [Jachec et al., 2006, Kang and Fringer, 2012, Masunaga et al., 2015, Rayson et al., 2018, Wang et al., 2009, 2011] because it can resolve IWs in shallow-water systems accurately with high spatio-temporal resolution.

For the sake of simplification and to avoid the effect of coastal circulation, I used the two-dimensional version of SUNTANS with the following configuration: bottom and side drag coefficient of 0.005; background viscosity of $\nu_H = 1$ and $\nu_v = 0.001\frac{m^2}{s}$ (similar to Kang and Fringer [2012] high values were used to avoid high-frequency nonlinear IWs and to make the model more stable); maximum and minimum horizontal resolution of 4 m (shore-side) and 19.2 m (ocean-side); vertical resolution of 0.25 m (with the exception of first layer=1 m); temporal resolution of 15 sec for runs and 5 minutes for processing. The two-dimensional framework in SUNTANS is capable of handling Coriolis force in IW generation. The tidal current was enforced at the ocean-side boundary ($x = 0$ km) barotropically as:

$$U = K1_{amplitude}\sin\left(\frac{2\pi}{\omega_{K1}}t + Lag_T\right) + M2_{amplitude}\sin\left(\frac{2\pi}{\omega_{M2}}t + \frac{\pi}{2}\right) \tag{5.10}$$

where Lag_T is the initial phase lag enforced on K_1. Also, to avoid IW reflection from shore-side and ocean-side boundaries, two sponge layers (at each side) were applied to relax the BC components of horizontal velocity gradually. It should be

noted that nonlinear, non-hydrostatic, and Mellor-Yamada 2.5 turbulence closure scheme were also employed.

5.3.1 Site of Study

In a coastal region where the pycnocline is shallow (less than 20 meters), the pycnocline does not always meet the steep bathymetry; therefore, it is of importance to choose a site where this interaction happens, and strong tidal flows occur. Without the loss of generality, I chose the structure (tidal height and density stratification) of southern Monterey Bay (Fig 5.2) in June 2018 (upwelling season) for this study as it 1) observes strong M_2 and K_1 surface tides [Petruncio et al., 1998]; and 2) is known for dominant semi-diurnal IW activity [Walter et al., 2012, 2014, Woodson, 2013]. The M_2 and K_1 tidal currents (0.056 and 0.022 $m.s^{-1}$) are enforced at the ocean-side boundary uniformly (in-depth) resulting in a tidal height of 0.98 and 0.72 meter at the shore (Fig 5.2-d). The total length of the model is 50 km with the typical southern Monterey Bay topography (using bathymetry provided by Walter et al. [2012] cut at 5 and 75 meters deep) and an idealized highly stratified water column (Fig 5.3). Monterey Bay is located at the 36° latitude with $f \sim 8.7 * 10^{-5}$ $\frac{1}{s}$ which is bigger than K_1 frequency $7.3 * 10^{-5}$ $\frac{1}{s}$; therefore, the IWs generated by K_1 tidal flow will propagate as Kelvin waves in the system. To avoid such circulation in our two-dimensional model, I used $f = 7.25 * 10^{-5}$ $\frac{1}{s}$ which corresponds to 30°. Such a minimal modification does not affect the results of IW generation and its conversion significantly.

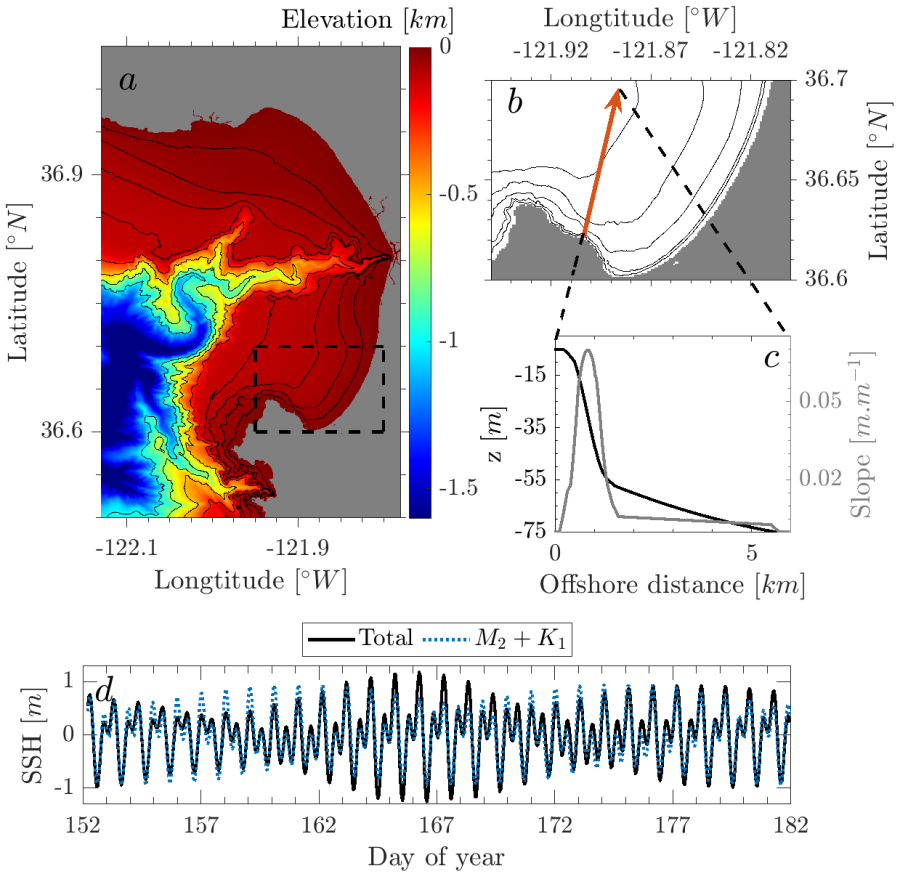

Figure 5.2: a) Monterey Bay bathymetry map with contours at 25, 50, 75, 100, 250, 750 and 1000 meters. b) The southern Monterey Bay with the contours at 5, 10, 25, 50 and 75 meters deep, c) The bathymetry profile and its slope along the orange arrow in the panel b which is taken from Walter et al. [2012]. The topography presented in panel c can be used as a representative for the southern Monterey Bay area. d) NOAA tidal gauge 9413450 sea surface height during June 2017.

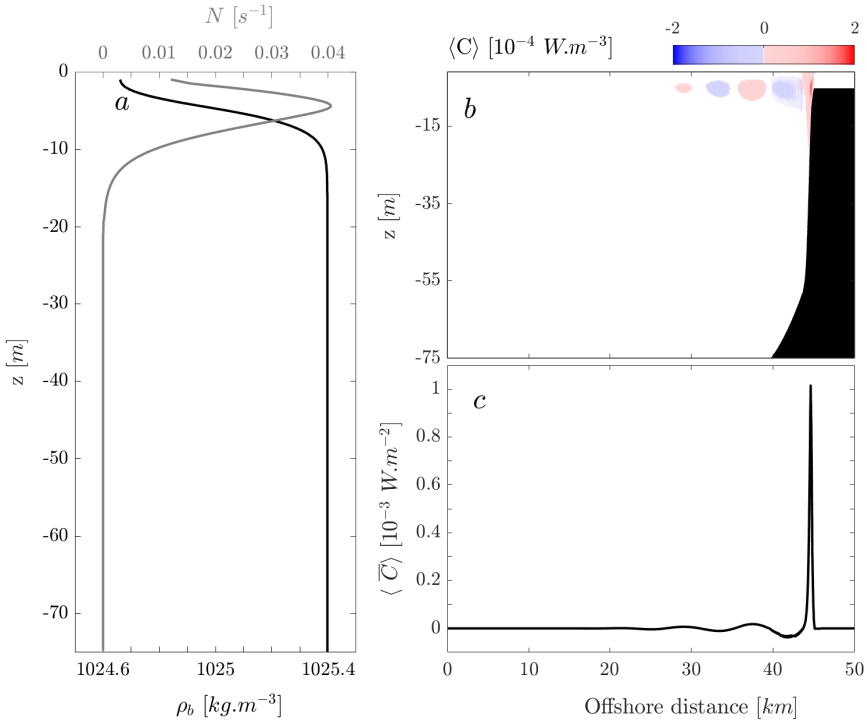

Figure 5.3: a) An idealized density stratification for a highly stratified system during the summer with $N_{max} = 0.04$ in the southern Monterey Bay with the pycnocline depth of 5 m. Time-averaged conversion rate $\langle C \rangle$ and time-averaged depth-integrated conversion rate $\langle \overline{C} \rangle$ are shown for one of the cases in panel b and c respectively.

5.3.2 Parameters

BT to BC conversion, which is a function of $\cos\left(\widetilde{\rho', W}\right)$, can be affected by perturbation factors such as tidal current frequency and velocity as well as the environmental characteristics (i.e., pycnocline depth). To study the role of each of these parameters on the conversion rate, I ran 63 case scenarios with different settings including pycnocline depth= 5: 2.5: 20 meters (in which the first and last numbers are the minimum and maximum of the range, and the middle one

indicates the step); variation of tidal constituents: no tide, M_2, K_1 and M_2K_1; $\overbrace{M_2, K_1} = -54°$: $30°$: $124°$ (this range covers the whole span, and after that, the pattern repeats itself).

As discussed in the theoretical framework, the time t should be chosen in a way that for any i and j: $\omega_i \pm \omega_j = n\frac{2\pi}{T}$ in which n is an integer. Therefore, I chose $T = [8 \text{ (spin-up)} + 27 \text{ (processing)}] * 12.4$ [hour] so that $T = 27T_{M2}(12.4[hr]) = 14T_{K1}(23.9[hr]) \approx 41T_{M2+K1}(8.16[hr]) \approx 13T_{M2-K1}(25.77[hr])$ to eliminate any residual conversion.

5.3.3 IW Generation and Reflection Behavior

Dimensionless numbers can be used to categorize and predict the behavior of phenomena. I utilize the steepness ratio (Γ_1) to differentiate supercritical ($\Gamma_1 > 1$) from subcritical ($\Gamma_1 < 1$) ocean topographies. Generated IWs at a supercritical topography are reflected as internal tidal beams down the slope, while for subcritical cases, we expect to observe the propagation of IWs toward the shore [Garrett and Kunze, 2007]. Moreover, we can benefit from the tidal excursion parameter Γ_2:

$$\begin{cases} \Gamma_1 = \frac{S_{Topo}}{S_{IW}} \\ S_{Topo} = \sqrt{(\frac{\partial d}{\partial x})^2 + (\frac{\partial d}{\partial y})^2} \\ S_{IW} = \sqrt{\frac{\omega^2 - f^2}{N^2 - \omega^2}} \\ \Gamma_2 = \frac{U_0 k_B}{\omega} \\ k_B = \frac{S_{Topo}}{H_0 - d} \end{cases} \tag{5.11}$$

where U_0, ω, k_B^{-1}, H_0 and d are characteristic BT tidal velocity, frequency, topography scale, maximum and local depth of the domain [Kang and Fringer, 2012, Zhang et al., 2011]. Tidal excursion provides an insight into the frequency of the system response where $\Gamma_2 > 1$ suggests the generation of lee waves; while, $\Gamma_2 < 1$ gives IWs with the same frequency of perturbation Garrett and Kunze [2007]. Finally, the Froude number ($Fr = \frac{U_0}{c}$), which is the ratio of BT tidal current speed (U_0) to wave phase speed (c) informs us about the linearity of the wave; where nonlinearity terms become important for cases with $Fr \simeq 1$ or $Fr > 1$.

5.4 Results and Interpretation

The conversion rate, which is the result of $g\rho' W$, can be affected by several parameters, including the depth of pycnocline, the presence of tidal constituents, and their phase lag. In this section, I analyze the effects of each parameter by studying the generated phase lag between ρ' and W at the conversion site as well as the total energy conversion $\widehat{\langle \overline{C} \rangle}$.

5.4.1 Pycnocline Depth

The pycnocline depth is a key component in the energy conversion process as it controls 1) the maximum conversion location and 2) the governing dimensionless parameters of Γ_1 and Γ_2. The vertical displacement at the pycnocline depth where the density varies abruptly is accompanied by considerable ρ', which promotes E_A and C noticeably. Therefore, we expect to observe an enhancement in the

conversion rate when the pycnocline is deepened enough to meet the supercritical bathymetry [Chen et al., 2014, Xie et al., 2015]. Such a situation can often be seen in the mid-ocean ridges or at the continental shelf breaks. On the other hand, in the nearshore area, the bathymetry is extended almost to the water surface (up to 5 meters); hence, regardless of the pycnocline depth, a strong interaction between the topography and pycnocline is often observed (especially for the Monterey Bay area as it has a supercritical bathymetry in the nearshore region).

As the pycnocline deepens, the conversion becomes more concentrated to a more focused block near the ocean bottom (panel c versus h in Fig 5.4). Most of the conversion occurs in a block of 5 to 10 meters above the bottom in a shallow-water system where W and ρ' are maximum (Fig 5.4). The pycnocline depth affects the location of maximum conversion (both the depth and offshore distance).

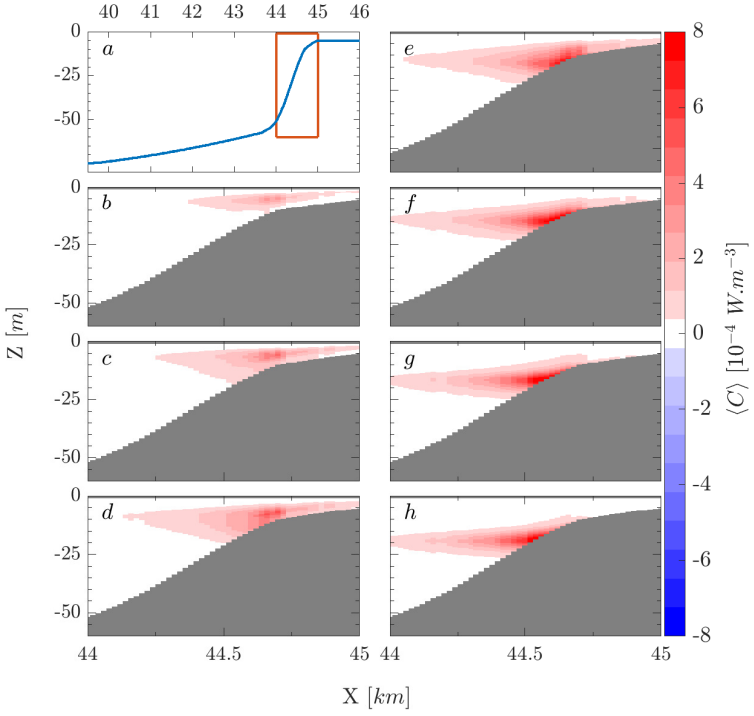

Figure 5.4: The effects of pycnocline depth on location and the intensity of maximum conversion rate for cases perturbed by M_2K_1 tidal currents. Panel a shows the topography of the nearshore area, while b to h show the $\langle C \rangle$ of the orange box. The time-averaged conversion rate $\langle C \rangle$ for cases with various pycnocline depth of 5, 7.5, 10, 12.5, 15, 17.5 and 20 meters are shown in panels b to h respectively.

For supercritical regions, the energy conversion increases as the ratio of local depth to the maximum depth declines ($d/H \rightarrow 0$) [Kang and Fringer, 2010]. Considering the steep topography of the Monterey bay nearshore area, a slight variation in the offshore distance results in a significant alteration in the water column depth, which in turn affects the profile of W and ρ'. W has a linear vertical profile with the maximum and minimum at the ocean bottom and surface. The deeper a system becomes, the slower the W decays with depth (it has a slope

proportional to $1/H$); therefore, the block might experience a higher W when the H is higher (the maximum conversion occurs at 4.5 and 19.5 meters deep for cases with pycnocline of 5 and 20 meters which corresponds to W of 0.69 and 0.77 $mm.s^{-1}$ in Fig 5.5-e). On the other hand, for shallow-water systems (where the sea surface elevation gradient is small), the shallower parts of the model experience higher vertical velocity near the bottom in comparison to deeper parts, as shown in Fig 5.5-e (W depends on $(z+d)$). Considering both factors, a balance between them is expected, as can be seen in Fig 5.5-b where the cases with pycnocline of 10 meters have higher W in comparison to the ones with pycnocline=5 or 20 meters. The ρ' structure has a different story where cases with pycnocline of 5, 7.5, 15 and 20 meters have a sharp bump, while other cases (pycnocline=10 and 12.5 meters) have a lower wider block of density perturbations which are extended to a bigger portion of the water column. Although these two categories (5, 7.5, 15 and 20 in comparison to 10 and 12.5) are not intrinsically different, I suspect such a variation is caused by the IW beam reflection, which is explained next, using the dimensionless numbers.

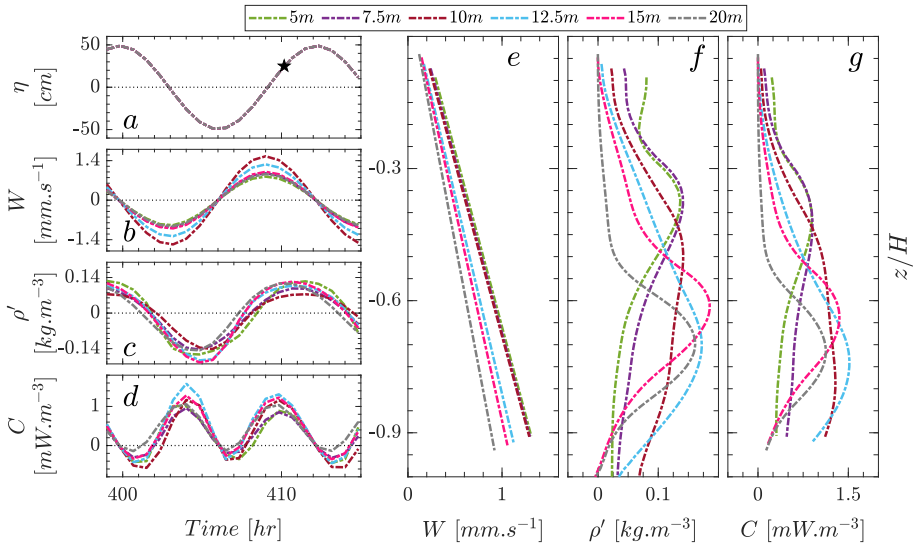

Figure 5.5: Sea surface, BT vertical velocity, density perturbation and conversion rate time-series are shown in panel a to d for cases perturbed by M_2 tides with pycnocline at various depths. Panels e, f and g show the vertical structure of BT vertical velocity, density perturbation and conversion rate respectively. All data are reported at the maximum location of $\widehat{\langle \overline{C} \rangle}$ where x =44.688, 44.628, 44.628, 44.588, 44.508 and 44.448 km, z =4.5, 7, 12.5, 13.75, 15 and 19.5 meters and the water column depth is 9.75, 12.5, 12.5, 14.75, 19.5, and 23.5 meters.

Analyzing the relationship between pycnocline depth and time-averaged spatially-integrated conversion rate, $\widehat{\langle \overline{C} \rangle}$, is a challenging task which is of interest [Chen et al., 2014, Kang and Fringer, 2012, Xie et al., 2015]. Supercritical topographies have shown their efficiency in converting energy from BT to BC mode in the literature [Chen et al., 2014, Kang and Fringer, 2012, Kelly and Nash, 2010, Zhang et al., 2011]. Kang and Fringer [2012] suggested that conversion rate depends on Γ_1, where the relation is convex (small conversion in high and low values of Γ_1). Therefore, to better interpret the results, I utilize the dimensionless parameters of Γ_1 and Γ_2. The results (linear IWs with $Fr \ll 1$, $\Gamma_1 > 1$ and $\Gamma_2 < 1$ as shown in

Fig 5.6) suggest a pattern similar to Kang's study both for M_2 and K_1; however, the maximum conversion in this study occurs around $\Gamma_1 = 7.5$ and 95 for M_2 and K_1 tides (Fig 5.6-a and 5.7-a), while Kang and Fringer [2012] reported $\Gamma_1 = 1.5$ for M_2. The source of such discrepancy can be the different nature of the topography modeled by Kang and Fringer [2012], where most of the conversion occurs at continental shelf break with the pycnocline around 250 meters deep and $\Gamma_1 = 1$ to 2. On the other hand, the topography used in this study is much steeper with shallow pycnocline varying from 5 to 20 meters deep. Moreover, I reported the weighted-average of Γ_1 (the weights are the conversion value at any location) in comparison to Kang and Fringer [2012], which reported all of the domain cells (in the Monterey Bay). Other studies such as Xie et al. [2015] employed different techniques to represent a weighted mean density stratification. It should be noted that the frequency and BT tidal velocity for a combination of tidal elements are not well defined; therefore, the Γ_1 and Γ_2 for M_2K_1 are not provided. Also, K_1 and M_2 have similar patterns while the K_1 has a higher range due to the small difference between ω_{K1} and f (Fig 5.6-a). Finally, the tidal excursion (using the details of maximum conversion location) is not sensitive to the pycnocline depth (k_b varies slightly as the depth of maximum conversion does not change remarkably).

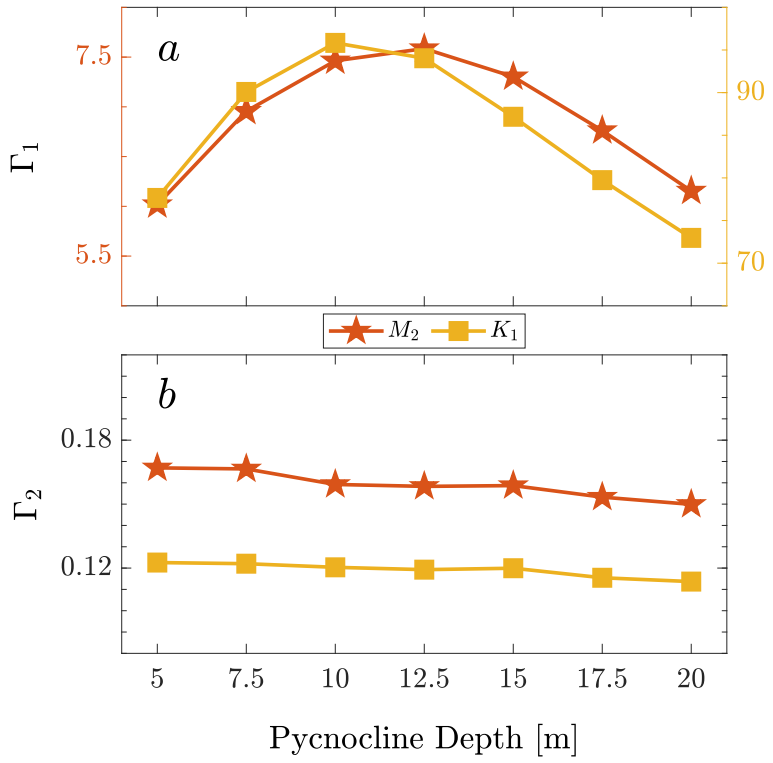

Figure 5.6: The relation between Γ_1, Γ_2 and pycnocline for cases perturbed by M_2 and K_1 is shown in panel a and b respectively. The M_2K_1 data is not plotted as ω and U_0 is not well defined in Γ_1, Γ_2 for a case perturbed by various tidal constituents. The panel a has two different vertical axis to accommodate the high range for K_1 (ω_{K1} is close to f which causes a significant amplification of Γ_1, while its behavior is similar to M_2). The initial phases of the M_2 and K_1 tidal currents are 90° and 144°. The bathymetry slope at the reported locations is increasing with deepening of the pycnocline as 0.0275, 0.0500, 0.0500, 0.0550, 0.0625 and 0.0675 for 5, 7.5, 10, 12.5, 15 and 20 respectively.

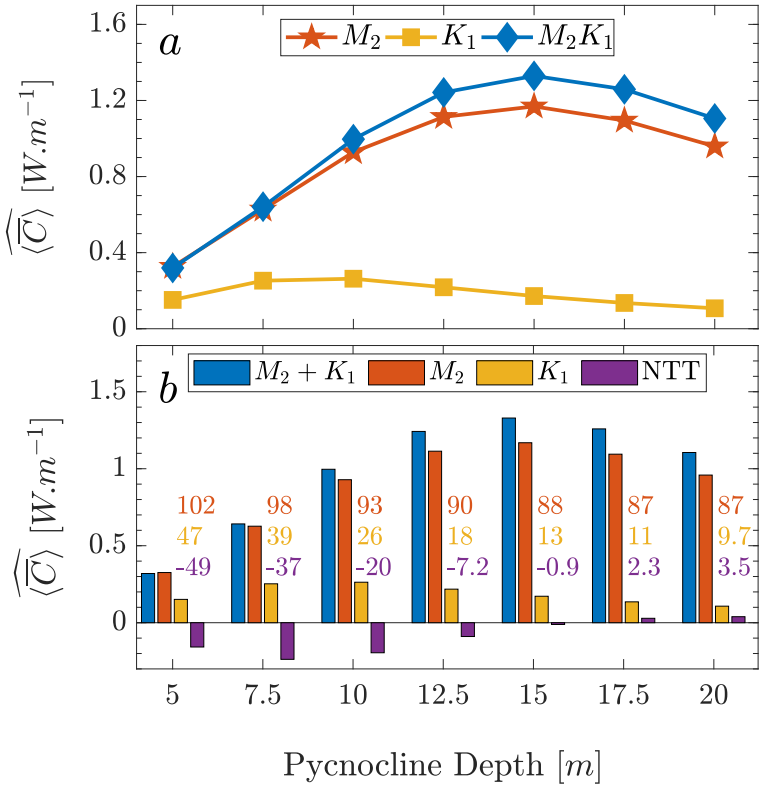

Figure 5.7: The effects of pycnocline depth on $\widehat{\langle\overline{C}\rangle}$ for cases perturbed by M_2K_1, M_2 and K_1. The initial phases of the M_2 and K_1 tidal currents are 90° and 144°. The contribution of M_2, K_1 and NT respective to M_2K_1 is shown in percentage in panel b.

5.4.2 Tidal Constituents

Due to the prominent role of M_2 tide in the BT to BC energy conversion and associated dissipation processes, the M_2 internal tide has received a great amount of attention, while other tidal constituents have been dismissed until recently [Carter, 2010, Carter et al., 2008, Jachec et al., 2007, Kang and Fringer, 2012, Merrifield and Holloway, 2002, Müller, 2013, Niwa and Hibiya, 2001, Rainville

and Pinkel, 2006]. The contribution of other tidal constituents in converting BT to BC energy can be up to 33% (the global energy conversion by M_2, S_2, K_1 and O_1 are estimated to be 1.11 (66%), 0.19 (11%), 0.24 (14%) and 0.13 (8%) TW) [Müller, 2013]. In other studies, the contribution of K_1 diurnal tide has been reported from 8% to 50% in comparison to M_2 in various places such as the Luzan strait and the Hawaiian ridge [Liu et al., 2017, Smith et al., 2017]. In this subsection, I discuss 1) the contribution of diurnal tides in the energy conversion process, 2) the interaction of two tides which excites other frequencies, and 3) the nonlinear tide-tide interaction in the nearshore area ($H < 100$ m).

The energy conversion, which correlates with the potential energy of linear IWs, is a function of IW amplitude ($E_A = \rho_0 N^2 \delta^2 / s$) and is governed by the BT tidal flow velocity and surface tidal height. The presence of strong surface M_2 and K_1 tides are reported in the southern Monterey Bay with the amplitude of 0.49 and 0.36 meters [Petruncio et al., 1998]. Considering M_2 and K_1 amplitudes and periods, the BT tidal velocity ratio is about 2.5 in favor of M_2, which makes M_2 IWs several times stronger than K_1. This pattern holds for the results of this study as K_1 conversion is 10% and 50% of M_2 when the pycnocline is at 5 and 20 meters (Fig 5.7-b). Deepening the pycnocline up to 10 meters intensifies K_1 energy conversion (up to 100 %), and after that, it declines (similar to M_2, which is discussed in the previous subsection). The lower BT velocity of K_1 tide not only generates a smaller conversion (W is half), but also causes the density perturbation to decay faster with the depth, which limits the conversion to a smaller region (Fig 5.9-f).

As discussed earlier (equation 5.9), the interaction of two waves, creates secondary frequencies in addition to the primary ones. We expect to see the period of 6.2 hr ($2M_2 \equiv 2\omega_{M2}$), 11.95 hr ($2K_1 \equiv 2\omega_{K1}$), 25.77 hr ($K_1 - M_2 \equiv 1/\omega_{K1} - 1/\omega_{M2}$) and 8.16 hr ($K_1 + M_2 \equiv 1/\omega_{K1} + 1/\omega_{M2}$) in a system perturbed by M_2K_1 where I call the $K_1 - M_2$ and $K_1 + M_2$ secondary, while $2K_1$ and $2M_2$ are primary frequencies (as they are the perturbation frequencies). Also, IWs generated at supercritical bathymetry can resonate with the frequency of $n\omega$ (other secondary frequencies) where n is an integer [Bell, 1975, Thorpe, 1997]. The primary, secondary, and resonance frequencies can be seen in the Fig 5.8. Although K_1 conversion is smaller than M_2, its presence creates two secondary frequencies (25.77 hr and 8.16 hr in Fig 5.8-a) with total conversion more than itself because the conversion amplitudes of the secondary frequencies are the average of primary's (equation 5.8). Therefore, the existence of K_1 in the system not only promotes the conversion at the frequency of $2K_1$, but also it creates strong conversion at hybrid frequencies. It should be noted that above the 30° latitude, IWs with frequencies greater than inertial's (24 hours) propagate as trapped Kelvin waves until they fully dissipate in the system. Therefore, I propose that K_1 enhances the conversion through generating mid-frequency waves as well as dissipating diurnal trapped Kelvin waves.

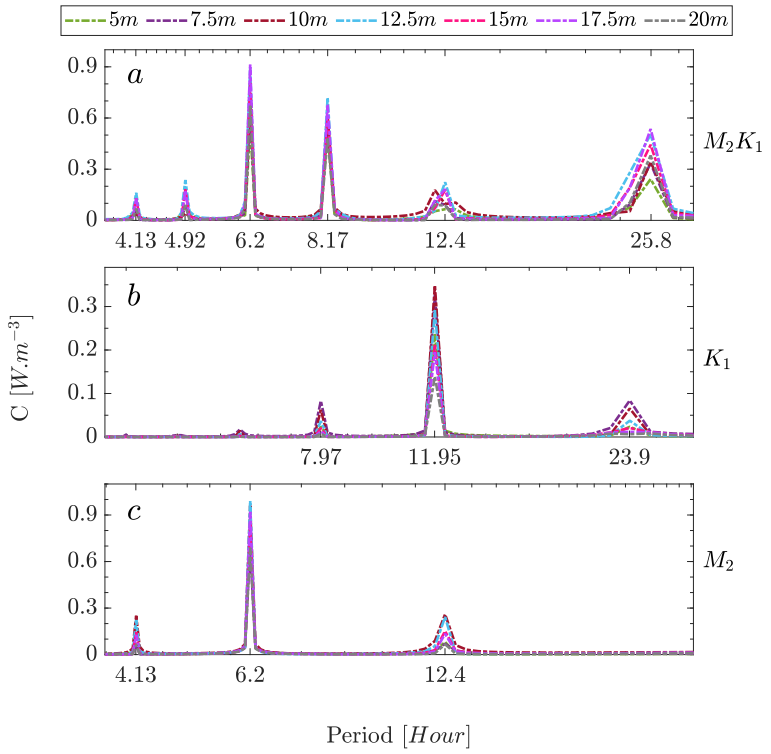

Figure 5.8: The Fourier decomposition of C at its the maximum location is shown for M_2K_1, K_1 and M_2 cases in the panel a, b and c respectively. Each panel shows the data for various pycnocline depth (5, 7.5, 10, 12.5, 15, 17.5 and 20 meters). The period peaks in the Fourier represent $T_{K1} = 23.9$, $T_{K1}/2 = 11.95$ and $T_{K1}/3 = 7.97$; $T_{M2} = 12.4$, $T_{M2}/2 = 6.2$ and $T_{M2}/3 = 4.13$ for panels b and c. For Panel a, the primary and secondary periods are $T_{M2}/2 = 6.2$, $T_{M2}/3 = 4.13$, $T_{K1} * T_{M2}/(T_{K1} - T_{M2}) = 25.8$ as well as some of the periods which are close together and the the decomposition did not separate them out clearly such as $T_{K1} * T_{M2}/(T_{K1} + T_{M2}) = 8.17$ and $T_{K1} = 23.9$ as well as $T_{M2} = 12.4$ and $T_{K1}/2 = 11.95$. There is an extra peak (4.92 hr) for $M2K1$ which is result of third order (in addition to primary and secondary) interaction between 8.17 and 12.4 (8.17*12.4)/(8.17+12.4).

The coupling of M_2 tidal IWs with near-inertial oscillations (such as winds) has been known for a long time as an effective mechanism of energy dissipation and cascade through higher frequency modes [Davies and Xing, 2003, Van Haren et al.,

1999, van Haren et al., 2003, Xing and Davies, 2002]. This study is more focused on investigating the immediate effects of K_1 presence on the energy conversion rather than its dissipation through the cascade. The conversion of M_2K_1 is mainly dominated by M_2 and the presence of K_1 only creates a phase shift in $\overbrace{\rho', W}$ (Fig 5.9-b). While such a phase shift barely exists for cases with pycnocline at 5 meters (M_2K_1 and M_2 are equal), deepening the pycnocline intensifies the phase difference leading to an increase in M_2K_1 in comparison to M_2. Another interesting point is that the NT term starts negative at pycnocline=5 meters and becomes positive. Based on Fig 5.9, it can be concluded that the NT term is significant for systems with extensive shallow pycnocline; however, the NT term can get discarded as the pycnocline becomes deeper than 12.5 meters by accepting 7% error. Therefore, as expected, the linear superposition holds valid for studies dealing with linear IWs, which are the common features of the continental shelf breaks.

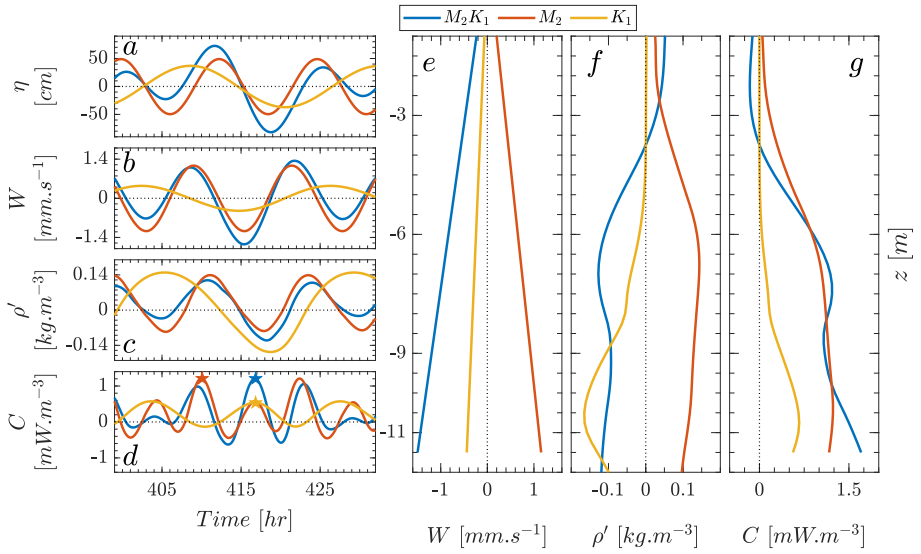

Figure 5.9: The time-series of various attributes (sea surface level, BT vertical velocity, density perturbation, and conversion rate) for different tidal constituents (M_2K_1, M_2 and K_1) are provided in panels a to d, while e, f and g are showing the vertical structure (BT vertical velocity, density perturbation and conversion rate) at the location of maximum conversion rate (x=44.648 km, z=9.75 meters and d = 11.5 meters) at different times (the blue, red and yellow stars denotes t =416.8, 410.1 and 416.8 hr).

5.4.3 Tidal Phase Lag

The tidal phase lag of M_2 and K_1, which is a function of time, can be an important parameter regarding the estimation of conversion rate in any active site such as Monterey Bay. Because M_2 and K_1 move in and out of phase throughout the year, it is significant to study the conversion rate sensitivity to their phase lag. Data suggests that although there is nonlinear interaction attributed to the M_2K_1 coupling, it is not sensitive to the tidal phase lag as the total conversion varies less than 5% for different phase lag values. Therefore, I reject the dependency of

nonlinear effects (NT) on the tidal phase lag regardless of the pycnocline depth (Fig 5.10).

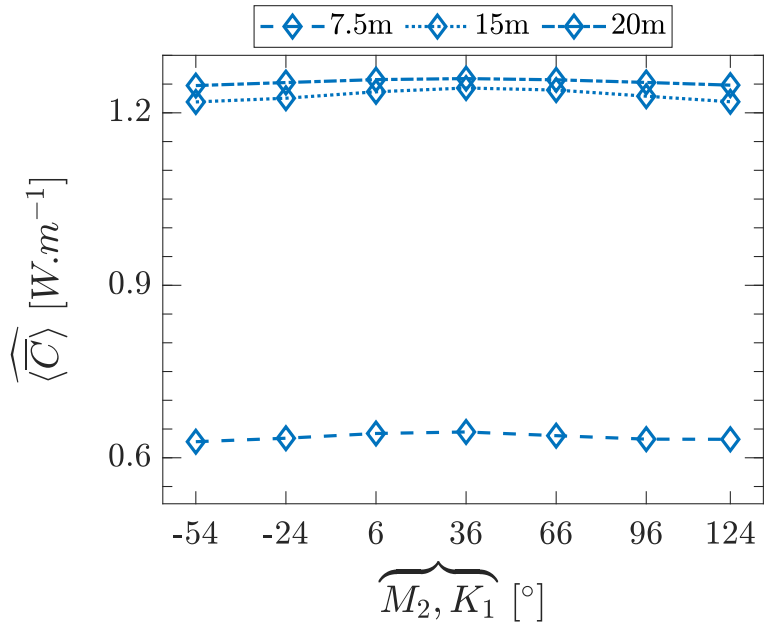

Figure 5.10: The relation between $\widehat{\langle\overline{C}\rangle}$ and the phase lag for cases with pycnocline at 7.5, 12.5 and 17.5 meters deep which are perturbed by M_2K_1 tidal current where the $\widehat{M_2, K_1} = Phase_{K1} - Phase_{M2}$ varies from $-54°$ to $124°$.

5.5 Conclusion & Future Work

The promotion of BT to BC energy conversion by tidal constituents other than M_2 in highly density-stratified nearshore regions has not received a lot of attention. In this paper, I included the K_1 BT tidal flow as a representative of diurnal constituents as well as considered the tidal interaction between K_1 and M_2 in the Monterey Bay. The southern Monterey bay with supercritical nearshore area experiences strong tidal flows and a considerable amount of IW activities as

well as prominent density stratification due to the upwelling during the summer; therefore, it is a perfect candidate for studying the M_2K_1 tidal interaction.

The conversion process, which is due to the phase lag between density perturbation and BT vertical velocity, gets affected by environmental parameters including the pycnocline depth, tidal constituent combination at play, and the phase lag between tidal elements. The fact that the inertial frequency is bigger than K_1 frequency at the Monterey Bay (and any location above 30° latitude) should not dissuade us considering its role as it can stimulate noticeable conversion at other frequencies higher than inertial's in combination with M_2. The $K1$ tide also converts BT energy to BC energy and dissipates it as trapped Kelvin waves. The data suggests that the optimum pycnocline depth for the maximum conversion is around 10 to 15 meters based on the active tidal constituents. The pycnocline controls the location of the maximum conversion block (which is 5 to 10 meters above the ocean bottom) as well as its concentration (the deeper the pycnocline, the narrower the conversion block becomes). Moreover, the linear superposition of M_2 and K_1 may become impaired by the nonlinear interaction term when the pycnocline is very shallow ($< 10m$). However, such a term approaches zero as the water column, and pycnocline become deeper. The dependency of conversion in a multi-tidal scenario can be an important parameter as M_2 and K_1 are not phase-locked [Kelly and Nash, 2010]; however, a such reliance was rejected by accepting 5% of error.

This study provides insight into the energy conversion in the nearshore area due to tide-tide interactions. However, there are more parameters affecting the

conversion, which should be considered. For example, the Monterey Bay and many other locations are profoundly affected by sea breezes, which can influence the conversion rate, vertical structure, and dynamics of the nearshore area. Moreover, the internal bores and asymmetric IWs should be considered because the IWs become nonlinear as they approach the shore.

5.6 Acknowledgments

This work was funded by NSF-OCE grant 1416837 to C. Brock Woodson. All model setup files and analysis scripts are available at `https://github.com/somidvar/suntans/tree/master/TideWindPaperSourceCode`.

Chapter 6

WIND-TIDE INTERACTION EFFECTS ON CONVERSION RATE[1]

Chapter Overview

The presence of the sea breeze and its impacts on the coastal dynamics have been studied extensively over the past several decades. In particular, the efficiency of cross-shore (XS) wind in XS transport has received considerable attention. However, the coupling of XS diurnal sea breeze and tidal currents requires further investigation. For example, the acceleration of tidal currents over a sloped topog-

[1]S. Omidvar, M. Fagundes and C.B. Woodson. Effects of environmental forcing on internal wave generation and conversion II: Tide-wind interactions. To be submitted to *Journal of Geophysical Research - Oceans*

raphy results in the generation of internal waves (IWs) and energy conversion from barotropic (BT) to baroclinic (BC) mode. In the coastal zone, sea breezes have the potential to alter the phasing and acceleration of these flows. Here, I analyze the factors which affect the dynamics of XS wind on tidal energy conversion. The results suggest an 1) intensification in the velocity gradient due to the presence of the wind, 2) the BT to BC conversion by wind solely, and 3) a strong (weak) correlation between the tide-wind phase lag and energy conversion for (semi-) diurnal tidal constituents, which affects the accuracy of linear superposition of wind and tide conversion.

6.1 Introduction

The coastal ocean connects the land to the open ocean and consequently, its biological, chemical, and physical processes and characteristics can affect how human impacts are translated to the larger ocean. The physical dynamics of the coastal ocean are complex, with high spatiotemporal variation due to a wide range of processes including tidal currents, XS and alongshore (AS) sea breeze and regional winds, shallow-water circulation, trapped Kelvin and IWs. In the past few decades, a great effort has been made to understand how these processes interact to determine coastal ocean circulation patterns. Here, I look at how the coupling of these two processes, tides and winds, affects the generation and dynamics of IWs.

The acceleration of tidal currents over the sloped topography can generate

IWs, which contribute significantly to biophysical conditions and energy budgets [Baines, 1974, Bell, 1975, Rattray Jr., 1960]. IWs are an integral part of the ocean which help to mix particles, to replenish nutrients, to diffuse energy through turbulence, to increase larval recruitment, to augment XS transport and most importantly to convert BT energy to BC mode [Boehm et al., 2002, Klymak and Moum, 2003, L. Shanks and G. Wright, 1987, Leichter et al., 1998, Munk and Wunsch, 1998, Pineda, 1995, Woodson, 2018]. While the role of IWs in converting the BT energy to BC mode has been studied extensively on the continental slope [Jan et al., 2008, Kang and Fringer, 2012, Kelly and Nash, 2010, Kelly et al., 2010, Merrifield et al., 2001, Moum et al., 2007, Niwa and Hibiya, 2001, 2004, Simmons et al., 2004], such a conversion is less understood in the coastal region where the dynamics can be affected by surface winds.

Recent studies help to understand the dynamics of AS wind and IW coupling in the mid-shelf region [Davies and Xing, 2003, Kurapov et al., 2009, Osborne et al., 2011, Suanda et al., 2011, Xing and Davies, 1997, 2002]. The role of AS wind can be seen in 1) promoting the spatiotemporal intermittency of IWs and increasing the turbulence as well as, 2) generation of IWs with near-inertial frequencies. The presence and relaxation of upwelling/downwelling AS wind adds to the fluctuation and turbulence observed over the shelf. Also, AS winds affect the dynamics of IW generation through altering the density stratification (Brunt-Vaisala frequency), which is a key element in the reflection behavior of IWs. Subcritical topographies allow onshore propagation of IWs, whereas supercritical ones reflect IWs back to the deep ocean. The coupling of M_2 tidal flow and near-inertial wind-induced

currents can be an effective process in the generation of $f-M_2$ IWs (the frequency is a function of inertial frequency of f and M_2), turbulent mixing and the energy transfer to higher modes [Davies and Xing, 2003, Xing and Davies, 1997, 2002].

In the inner shelf regions, where the Ekman spiral does not fully develop as the water column is not deep enough and the pycnocline suppresses the vertical diffusion of momentum, the AS wind is not efficient in driving XS transport [Austin and Lentz, 2002, Tilburg, 2003]. In such systems, the surface and bottom boundary layers usually overlap and interact with each other. The result of which is the XS transport by XS wind where offshore wind creates an offshore flow in the surface layer and it is compensated by the onshore flow in the bottom layer where the zero crossing of the velocity occurs at half of the water-column depth [Fewings et al., 2008, Tilburg, 2003]. In this paper, I analyze the role of XS wind on the BT to BC energy conversion due to tidal flows over the topography.

6.2 Theoretical framework

Under the Boussinesq approximation, the governing equations for incompressible fluid consist of continuity ($\boldsymbol{\nabla}.\mathbf{u}$=0), momentum conservation ($\frac{\partial \mathbf{u}}{\partial t} + \mathbf{u}\boldsymbol{\nabla}.\mathbf{u} + \mathbf{f} = \frac{1}{\rho_0}\boldsymbol{\nabla}\mathbf{P} + \nu\boldsymbol{\nabla}^{\mathbf{2}}\mathbf{u} - \frac{\rho}{\rho_0}\mathbf{g}$), and density transport ($\frac{\partial \rho}{\partial t} + \mathbf{u}\boldsymbol{\nabla}\rho = \kappa\boldsymbol{\nabla}^{\mathbf{2}}\rho$) where $\mathbf{g}$, $\mathbf{f}$, ν, κ are gravity vector ($-g\ \hat{k}$), Coriolis vector ($fv\ \hat{i}$-$fu\ \hat{j}$), eddy viscosity and diffusion. The density (pressure) can be partitioned into $\rho = \rho_0 + \rho_b + \rho'$ ($P = P_0 + P_b + P'$) where the terms are reference, background, and perturbation constituents. Also, the velocity can be divided to BT ($U, V = \frac{1}{H}\overline{u}, \frac{1}{H}\overline{v}$) and

BC parts$(u', v', w' = u - U, v - V, w - W)$ where the bar operator provides the depth-integrated value of a parameter ($\overline{\psi} = \int_{-d}^{\eta} \ dz$) and η, $-d$, H are water surface elevation, ocean bottom and water-column depth. To satisfy the continuity equation the BT vertical velocity W must satisfy $W = -\boldsymbol{\nabla}_h.[\mathbf{U_h}(d+z)]$ where h subscript denotes the horizontal direction [Kang and Fringer, 2012].

Using these definitions, the depth-integrated time-averaged BT to BC energy conversion (including the kinetic and potential) becomes $\langle\overline{\rho' g W}\rangle$ where the angled-bracket provide the time-average ($\langle\psi\rangle = \frac{1}{T}\int_0^T \ \mathrm{d}t$) [Kang and Fringer, 2012]. It should be noted that the conversion can also be calculated as a function of pressure perturbation felt at the ocean bottom, which has been used in many studies $C = \vec{\boldsymbol{\nabla}} H.UP'|_{z=-H}$ [Carter et al., 2008, Gerkema et al., 2004, Kelly and Nash, 2010, Kelly et al., 2010, Kurapov et al., 2003, Llewellyn Smith and Young, 2002, Pickering et al., 2015]. However, $C = \rho' g W$ gives a better representation as it shows the conversion through depth.

Similar to part I, considerig the IWs are linear in this study, I assign idealized sinusoidal functions to BT vertical velocity and density perturbation as $W = \sum a'_j \sin\left(\omega_j t + b'_j\right) + c'_j + \text{NTW}$ and $\rho' = \sum a_i \sin(\omega_i t + b_i) + c_i + \ \text{NTW}$ where a_i (a'_i), b_i (b'_i), and c (c') are amplitude, initial phase and constant values of the functions. The time-averaged conversion due to the tidal current and wind effect is $\langle C\rangle = \cos\overbrace{W, \rho'} + NTW$ where the over brace operator shows the phase difference ($\overbrace{a, b}$ is the phase difference between variables a and b) and NTW is the nonlinear effect of the wind (similar to NTT in part I).

6.3 Numerical Setup

I used SUNTANS (Stanford Unstructured Non-Hydrostatic Terrain following Averaged Navier-Stokes Simulator [Fringer et al., 2006]) to study the role of XS diurnal sea breeze in the energy conversion process in the southern part of Monterey Bay. SUNTANS utilizes an unstructured triangular z-level grid system and has been extensively employed in studying nonlinear, non-hydrostatic hydrographic studies in the coastal ocean [Chua and Fringer, 2011, Fringer and Zhang, 2008, Kang and Fringer, 2012, Liu and Chua, 2016, Masunaga et al., 2015, Ming and Chua, 2014, Walter et al., 2012, Xu and Chua, 2017].

6.3.1 Model Configurations

Studying the role of wind in a shallow water system is an arduous task that can be simplified by using two-dimensional models. Such a simplification is necessary at this point as it allows to unfold the governing process and identify patterns [Kurapov et al., 2009, Osborne et al., 2011]. Many of the 2-D models use the periodic boundary condition, which loops the model in the AS direction [Kang, 2010, Kurapov et al., 2009]. However, in this study, I avoided using such a technique as it can cause issues because of the significantly large AS currents created by the wind over the time. Instead, I used a 2.5-D configuration for SUNTANS, which is essentially a two-dimensional model capable of comprehending and simulating some of the intrinsically three-dimensional processes such as Ekman spiral in a two-dimensional setup with closed boundaries (no-flow) in the AS direction.

I used a smoothed bathymetry (Fig 2 in part I) and idealized density stratification (Fig 3 in part I) of the southern Monterey Bay during the upwelling season (summer) accompanied by the moderate to strong (3 and 6 $m\ s^{-1}$) diurnal shoreward sea breeze as well as the major BT tides. The bottom drag, horizontal (vertical) eddy viscosity, run (processing) time-step, minimum (maximum) horizontal spatial resolution and layer thickness are 0.005, 1 $m^2.s^{-1}$ (0.001 $m^2.s^{-1}$), 5 s (300 s), 4 m (19.2 m) and 0.25 m. The IWs are damped at the both sides (ocean-side and shore-side boundaries) of the model by relaxing the BC elements (u', v').

To get better results, the time-average span should be chosen in a way to avoid any residual value generated at the secondary frequencies. Considering the three primary frequencies of M_2, K_1 and wind, several low and high secondary frequencies are expected. Hence, I chose the total time of 13.5 days to get almost no residual as the prefect time-averaging requires significantly long runs. $T = [8\ \text{(spin-up)} + 27\ \text{(processing)}] * 12.4hr = 27\ M_2$ [12.42 hr]=14 K_1 [23.9 hr]=13.95 Wind [24 hr]= 41 ($K_1 + M_2$) [8.16 hr]= 13 ($K_1 - M_2$) [25.77hr]= 40.9 (Wind+M_2) [8.18 hr]= 13 (wind-M_2) [25.74 hr]= 27.96 (wind+K_1) [11.97 hr]= 0.05 (wind-K_1) [5,736 hr]). Therefore, taking average over $\approx$ 13.5 days washes out most of these residual conversion.

6.3.2 Tidal Flow & Wind

The most prominent tidal constituents in the southern Monterey Bay are the semi-diurnal M_2 and diurnal K_1 with the tidal range of 0.98 and 0.72 m [Carter, 2010,

Petruncio et al., 1998]. The regional-scale wind pattern suggests northwesterly wind during the summer, which is upwelling favorable on the west coast [Beardsley et al., 1987, Woodson, 2013]. The prevailing upwelling wind induces a southward jet of cold deep water at the Point Ano Nuevo, which surrenders the water inside the bay. The trapped water inside the bay which remains there for a significant time (8 to 17 days Woodson et al. [2007]) becomes warm and forms shallow lenses (4 to 7 meters) of warm water which is significantly more buoyant (up to 10° Celsius) than the rest of water column [Graham and Largier, 1997, Paduan and Rosenfeld, 1996, Rosenfeld et al., 1994]. Such a system is highly stratified and is favorable for the generation and propagation of IWs.

In addition to the upwelling-favorable regional wind, the diurnal sea breeze is present due to a pressure gradient between Salinas Valley and Monterey Bay water in the afternoon during the upwelling season [Banta et al., 1993, Woodson, 2013]. The wind record at the Hopkins Marine Station (HMS) during June 2017 suggests the shoreward diurnal oscillations rather than an onshore-offshore pattern with the major axis aligned with XS (Fig 6.1).

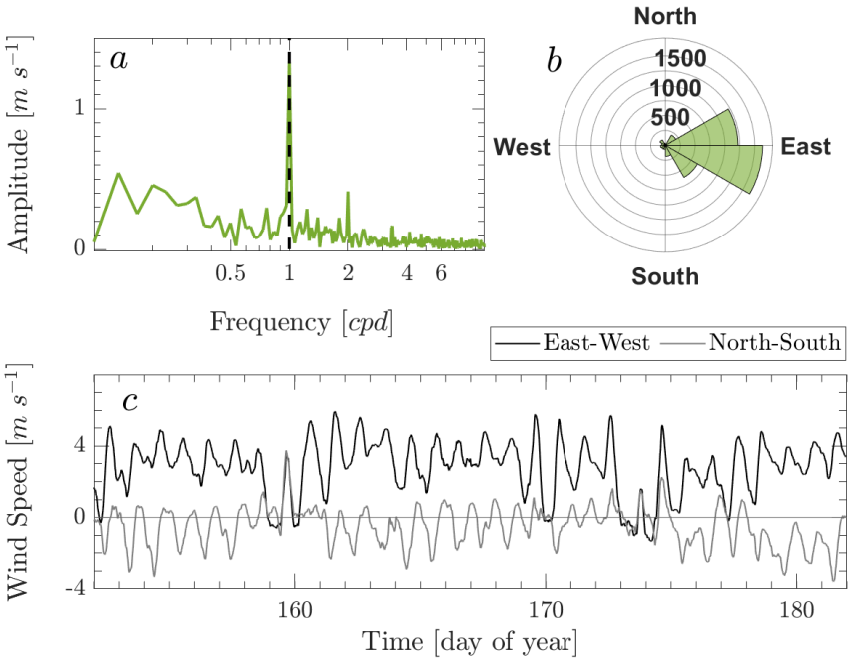

Figure 6.1: The figure provides the wind record for HMS during June of 2017. Panels show the oscillation amplitude at the primary frequency (a), 10-minute wind polar histogram (b) and XS-AS wind constituents (c).

6.3.3 Parameters

In part I, I analyzed the tide-tide interaction, while in this part, I examine the wind-tide coupling as well as the role of wind in tide-tide interaction. To examine these interactions, I consider different pycnocline depths of 5: 2.5: 20, where the colon notation denotes minimum, step and maximum values of a parameter. I cover the different tidal combination of M_2, K_1, M_2K_1 with and without wind. The diurnal sea breeze records suggested a moderate to strong shoreward wind; hence, I chose 0, 3, and 6 $m.s^{-1}$ which corresponds to the shear stress of 0, 0.013, and 0.05 Pa [Large and Pond, 1981]. As the dependency of energy conversion of

M_2K_1 on initial phase lag ($\overbrace{M_2, K_1}$) was rejected in part I, I discarded the tide-tide phase lag effects in this study. Such a realization avoids the exponential growth in the number of cases required.

6.4 Results and Interpretation

As mentioned in section 2, the conversion rate, which is the result of $\rho' gW$, can get affected by several parameters, including the depth of pycnocline, the combination of tidal constituents, wind speed and direction as well as tide-wind phase lag. In this section, I analyze the effects of each parameter on linear IWs by studying the vertical structure of the water column, density and velocity perturbation time-series and the phase lag between ρ' and W which affects the total energy conversion $\widehat{\langle \overline{C} \rangle}$ where the wide-hat operator denotes an integral over the XS ($\widehat{\phi} = \int_0^L \phi \mathrm{d}x$).

The presence of XS wind can affect the dynamics of a shallow water system by strengthening the shear velocity which might result in upwelling and downwelling over a sloped bathymetry. In the inner-shelf region, where the boundary layers overlap, the XS transport is dominated by the XS wind rather than AS wind [Fewings et al., 2008, Tilburg, 2003]. The onshore wind creates a shear flow where the upper layer transports materials shoreward and the compensating offshore current occurs in the bottom layer [Fewings et al., 2008]. Tilburg [2003] proposed an empirical-analytical relation of $2.3\sqrt{\frac{\tau}{\rho_0}}\frac{1}{f(1+N^2/f^2)^{0.25}}$ to estimate the thickness of the top layer which gives the zero-crossing of 10 meters for the severe wind of 6 $m.s^{-1}$. Fewings et al. [2008] suggested the thickness of $\frac{H}{2}$ to $\frac{H}{3}$, which is equal to

6 meters over the slope. Our results agree well with these findings as the density-stratified system forms a two-layered flow where the offshore and onshore velocity magnitudes are almost equal (symmetric) and the zero-crossing occurs at the half of the water column depth (Fig 6.2-e and d). On the other hand, for the mid-shelf region, where the bottom and surface boundary layers have more space to develop, the velocity is more intensified in the surface layer (asymmetric); therefore, the surface layer thickness is closer to $\frac{H}{3}$ (Fig 6.2-b and c). A small intensification can be seen in Fig 6.2-e near the ocean bottom part during the ebb tide which can be counted toward the acceleration of the flow over a sloped bottom or a fully BT response due to the presence of the bottom drag; therefore, the cases with wind behaves similar to the ones without wind [Edwards and Seim, 2008].

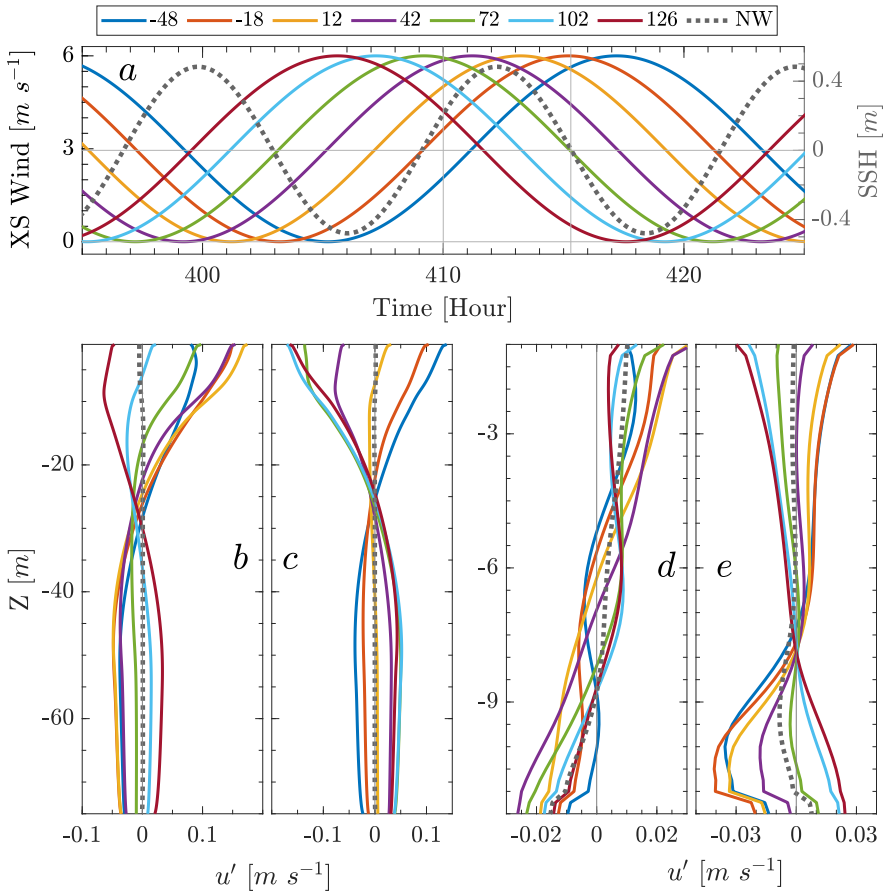

Figure 6.2: The figure provides the horizontal velocity perturbation due to the presence of IWs and XS wind. The left vertical axis in panel a shows the wind speed, while the right one provides the sea surface height. Panels b-c and d-e provide the vertical structure at $x = 37.058$ km (offshore) and $x = 44.668$ km (at the slope) respectively. The system responses during the ebb ($t = 402.8$ hr) and flood ($t = 410$ hr) are shown in b-d and c-e.

Although the wind does not affect the BT constituents remarkably, it can alter the vertical structure, which affects the conversion and circulation dynamics (Fig 6.3). To better understand the effects of wind and the role of its initial phase on the system dynamics, I simulated a case perturbed only by wind (no tidal currents).

As expected, even a strong wind of 6 $\frac{m}{s}$ does not cause water accumulation as the net XS is almost zero (η and W are negligible in Fig 6.3-b and c); however, it creates ρ' and C which are comparable to ones induced by tidal currents (compare Fig 6.3-d with 6.4-d and 6.4-d). As mentioned, the top (bottom) layer moves onshore (offshore) during the wind intensification. The bottom layer response easily extends over the slope to satisfy the continuity equation, which results in a negative (positive) u during the wind intensification (relaxation) corresponding to a downwelling (upwelling) regime with negative (positive) vertical velocity (Fig 6.5). Such behavior can significantly increase the shear velocity and actively circulate the water and materials in the inner-shelf.

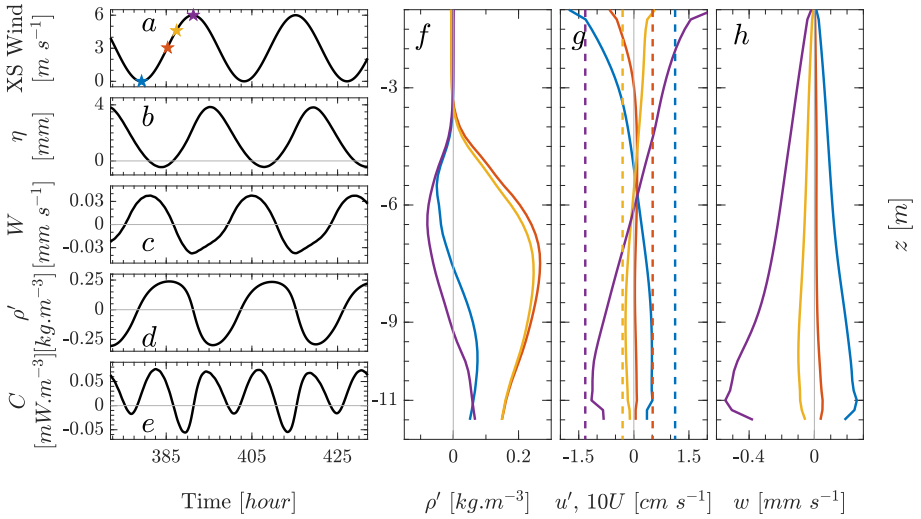

Figure 6.3: The time-series and vertical structure of the nearshore area are shown for cases perturbed only by wind (pycnocline=7.5 meters). The panels a to e are showing the time-series at $x = 44.668$ km and $z = -9$ meters. Panels f to h are showing the vertical structure of density perturbation, horizontal velocity perturbation and ten-times of horizontal mean velocity (dashed lines in panel g) as well as the vertical velocity at various time which are shown with blue, red and yellow stars in panel a.

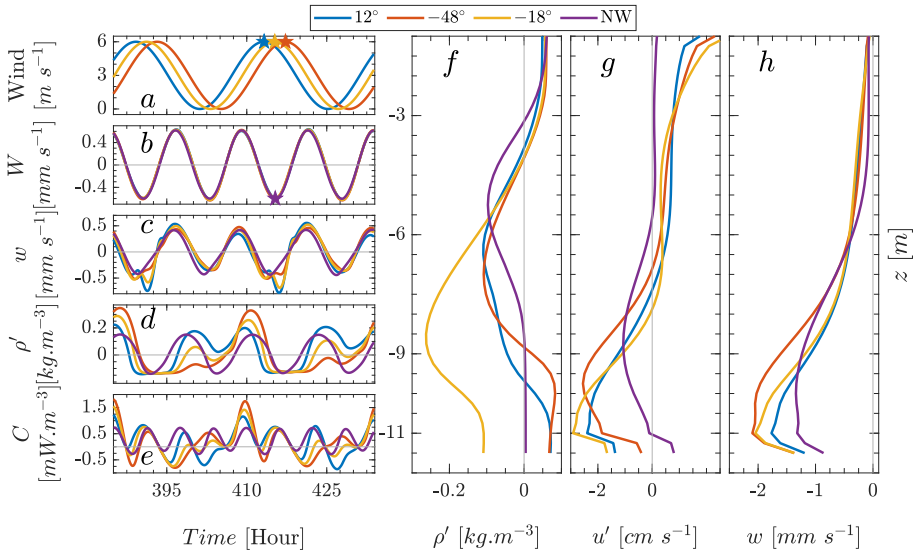

Figure 6.4: Similar to Fig 6.3 where $z = -6$ meters and the model is perturbed by M_2 tide and wind (blue, yellow and red curves) as well as only by tide (purple). The wind initial phases are shown in the top panel. Panel f to h shows the vertical structure at the time= 413.25 (blue), 415.25 (yellow) and 417.25 hours (red) when the wind speed is at maximum (the purple corresponds to 415.33 hours) which is shown in panel a by stars.

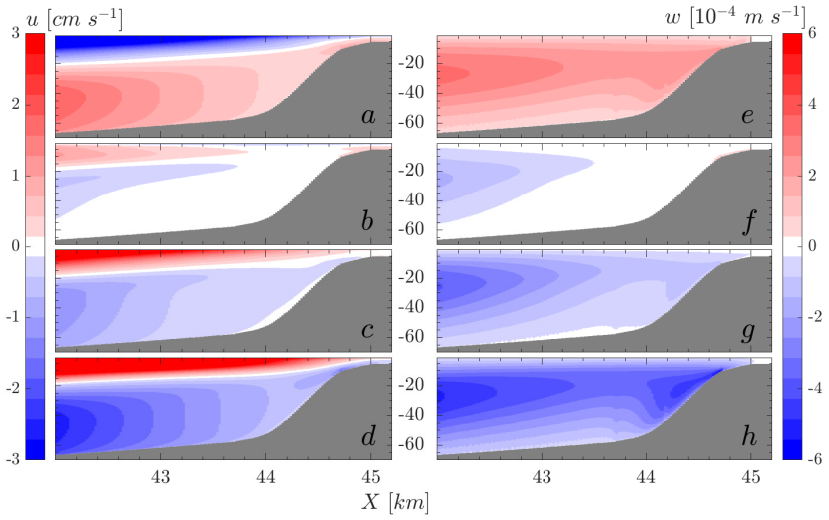

Figure 6.5: Horizontal (left panels) and vertical velocity (right panels) for a case perturbed only by the wind with the pycnocline depth of 7.5 meters. The timing of the panels are 379.25, 385.33, 387.42 and 391.33 hours from top to bottom respectively.

6.4.1 Initial Wind Phase

The relative phasing of BT and BC constituents is of importance as it governs the system dynamics. The time-series in Fig 6.3 over the slope suggest that wind speed and W are off-phase by 180°, while the $\overbrace{\rho', W}$ is 5 hours which corresponds to 75° resulting in a positive conversion ($< 90°$). This realization can be a significant help in the interpretation of wind and its initial phase roles in the energy conversion process as constructive interaction is expected when the ebb flow coincides with the maximum wind speed. Similarly, the synchronization of flood flow and wind results in a destructive reaction. The amplification and attenuation of ρ' and w amplitudes by the wind for K_1 cases can be seen in Fig 6.6-c and d (red versus to

blue curve). The wind dominance over the tide can be seen in the u' and w records over the slope as the wind outweighs the K_1 tidal flow (although the red star has the minimum tidal velocity, the red curves (u, w) are significantly bigger than no-wind purple counterpart). Not only are the amplitudes of BC constituents (ρ' and u') affected by the wind, but also the wind can retard or advance the phasing of such components for K_1 tidal cases based on $\overbrace{\text{tide, wind}}$. In the absence of wind, $\overbrace{\rho', W} \approx 61°$ (purple curve in Fig 6.6), while the wind changes this to $\approx 55°$ for the red curve which counted toward a constructive interaction ($\cos 55° > \cos 61°$).

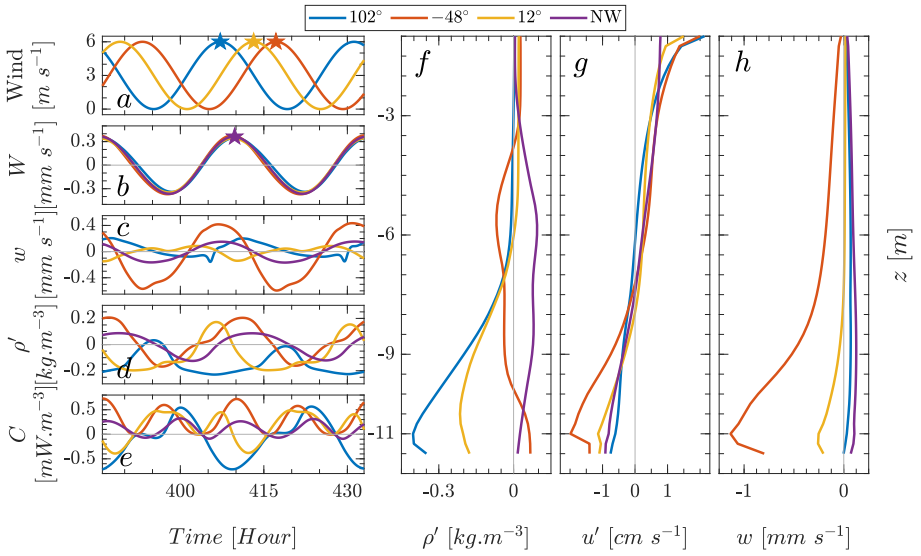

Figure 6.6: Similar to Fig 6.4 where $z = -9.25$ meters and the model is perturbed by K_1 tide and wind (blue, yellow and red curves) as well as only by tide (purple). Panel f to h shows the vertical structure at the time= 40.17 (blue), 413.17 (yellow) and 417.17 hours (red) when the wind speed is at maximum (the purple corresponds to 409.75 hours) which is shown in panel a by stars.

The story is a bit more complex for the M_2 tidal cases as M_2 is not phase-locked with the wind as K_1 is. The big gap between K_1 and wind periods makes

their interaction intrinsically different from M_2-wind as the wind perturbation time-scale is closer to K_1 in comparison to M_2 (24 and 23.9 hours are closer than 24 and 12.4 hours). Such a difference slows down the M_2 perturbations and flattens the tips of ρ' minimums (Fig 6.4-d). The flattening of ρ' can be physically interpreted as the resistance induced by the wind forcing against gravity (the restoration force). The upwelling-downwelling generated by the wind is slower than the tidal ones; therefore, it seems that the wind is freezing the particles both during the ebb and flood tides for a small period of time (Fig-6.4-d). Such an alteration in the shape of a sinusoidal signal can be translated as the work done by NTW which corresponds to a net variation in $\overbrace{W, \rho'}$.

There is an unfiltered secondary frequency (5,736 hours) perturbation affecting the $\langle C \rangle$ results. Although I don't deny the contribution of such a term, I don't believe it can be responsible for the dependency of wind contribution (in the conversion process) on its initial phase (as longer simulations suggested the same pattern). Instead, I propose that the variation of conversion by wind is due the wind-induced deformation of ρ' time-series. Moreover, taking the time-average over such a long time does not provide a realistic conclusion as some of other physical configurations are changing in the time span of eight months, including the presence of onshore diurnal see breeze (as they are only strong during spring and summer) as well as the the strong density stratification (which will be altered by the intensification and relaxation of upwelling jets at the point Ano Nuevo Woodson [2013]). Therefore, the initial $\overbrace{\text{wind, tide}}$ can be counted as a characteristic of the system. Last but not least, filtering such a frequency requires

a tremendous amount of computational resources as the simulation of each case (with the duration of $\approx$ 18 days) took 6 hours using 48 cores, 700 GB of hard disk and 100 GB of RAM on the SAPELO supercomputer at the University of Georgia. Extending the run-time to remove the aforementioned period demands ten times higher processing and storage resources.

It can be concluded that K_1 (M_2) tidal flow, which is (is not) phase-locked with the wind, has a conversion rate that is sensitive (insensitive) to the initial wind-tide phase lag. The M_2 conversion is remarkably amplified by the presence of wind up to 40%. and its on the initial phase is as small as 5% which is insignificant. On the other hand, the contribution of wind in cases perturbed by K_1 can increase or decrease the conversion by 700% (middle and right columns in Fig 6.7). Therefore, K_1-wind conversion depends heavily on the $\overbrace{\text{wind, tide}}$ and dismissing the K_1 tide in the energy budget calculation can cause a serious overestimation (due to its negative conversion for some cases) or underestimation based on the initial wind phase.

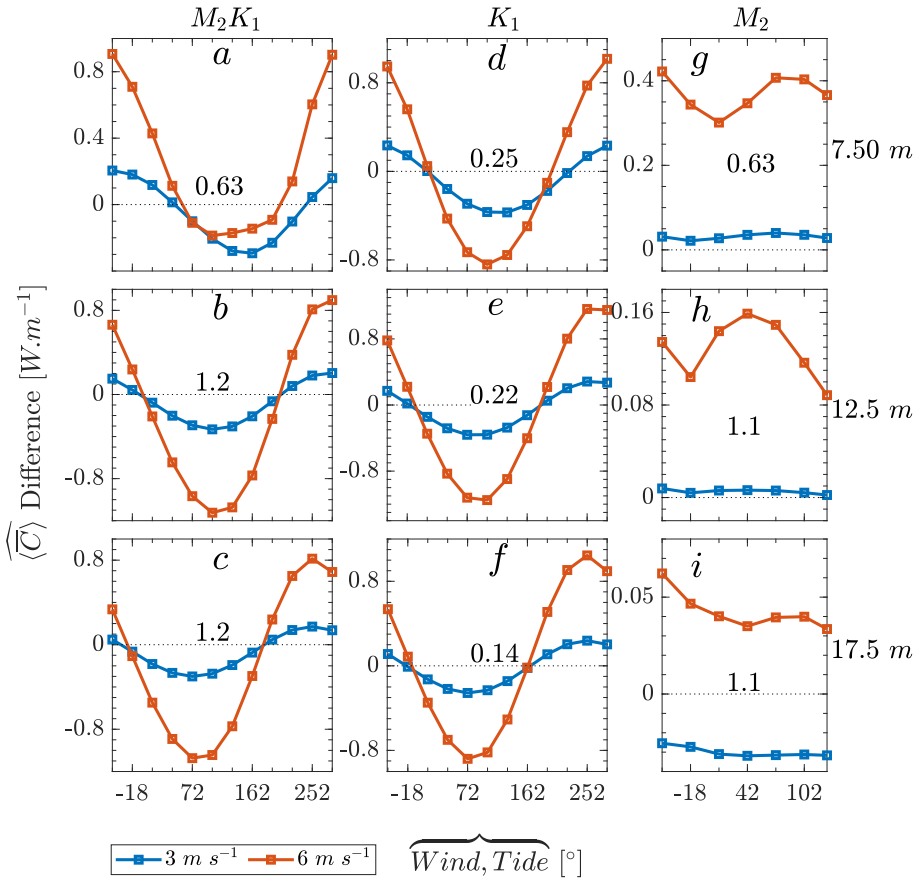

Figure 6.7: The contribution of XS wind in XS-integrated depth-integrated tidal-averaged conversion rate, $\widehat{\langle \overline{C} \rangle}$, is shown for various cases as the difference with the baseline values (the value printed inside each panel). The columns show the $\widehat{\langle \overline{C} \rangle}$ for M_2K_1, K_1 and M_2 from left to right, while the rows provides the details for pycnocline at 7.5, 12.5 and 17.5 meters. The severe and moderate wind (6 and 3 $m.s^{-1}$) are shown with red and blue curves. The initial phases of M_2 and K_1 tidal currents are 90° and 36°.

To be assured that such a dissimilarity can be fully explained by the tidal period, I ran cases perturbed by a hypothetical tidal constituent of 20 hours whose conversion results are similar to M_2 rather than K_1 as it is not sensitive to the initial tide-wind phase lag (Fig 6.8).

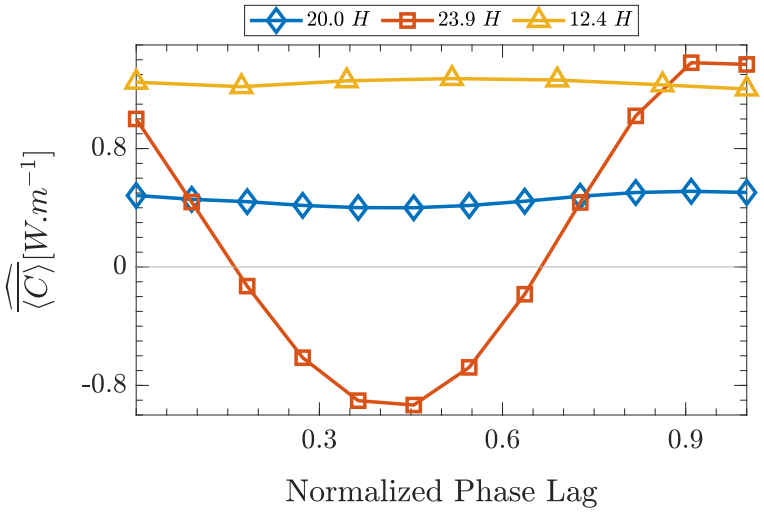

Figure 6.8: Similar to Fig 6.7 where the sensitivity of conversion on wind-tide phase lag is evaluated with a hypothetical tidal constituent with 20 hours period for cases with pycnocline depth of 12.5 meters. The M_2 and K_1 data are plotted in a normalized format (the whole phase lag span is normalized between 0 to 1) for the sake of comparison.

6.4.2 Pycnocline Depth

As discussed in part I, the pycnocline depth is an important parameter in shallow-water systems as it governs the coastal dynamics through dimensionless numbers such as steepness ratio and tidal excursion to examine the reflection and nonlinearity of IWs respectively [Garrett and Kunze, 2007, Kang and Fringer, 2012, St. Laurent and Garrett, 2002]. Moreover, the pycnocline depth governs the wind-tide interaction as the pycnocline, where the maximum of density gradients occur, acts as a guideline for IWs. The wind forcing declines with depth; therefore, with shallow pycnocline, the wind can create more potential energy (higher $\Delta\rho$) in the system. On the other hand, the bottom slope where the oscillations happen and

the ratio of the water column which contributes to the energy conversion process, are other important parameters that affect the conversion (refer to part I for more details). Therefore, even without the presence of wind, we expect to see a balance between these parameters with an optimum pycnocline depth (conversion values in the first column of Fig 6.9). For the cases perturbed by both tidal flow and wind, the same pattern (the $\overbrace{\text{wind, tide}}$ used for all panels of Fig 6.9 invokes a destructive interaction) is observed for all wind speed and pycnocline depth except the cases with pycnocline of 5 meters. However, the story is different for cases with a pycnocline of 5 meters as the destructive wind stress promotes conversion. For cases with extremely shallow pycnocline, there might be a lack of interaction between the stratified water and the bathymetry, the result of which is a low conversion. In such a situation, the presence of wind promotes the bottom-tide interaction, which elevates the conversion in the system. The translation of the maximum conversion toward the bathymetry by wind can be seen in the last row of Fig 6.9. Due to such a different pattern, I discarded the cases with 5 meters pycnocline for the rest of the study.

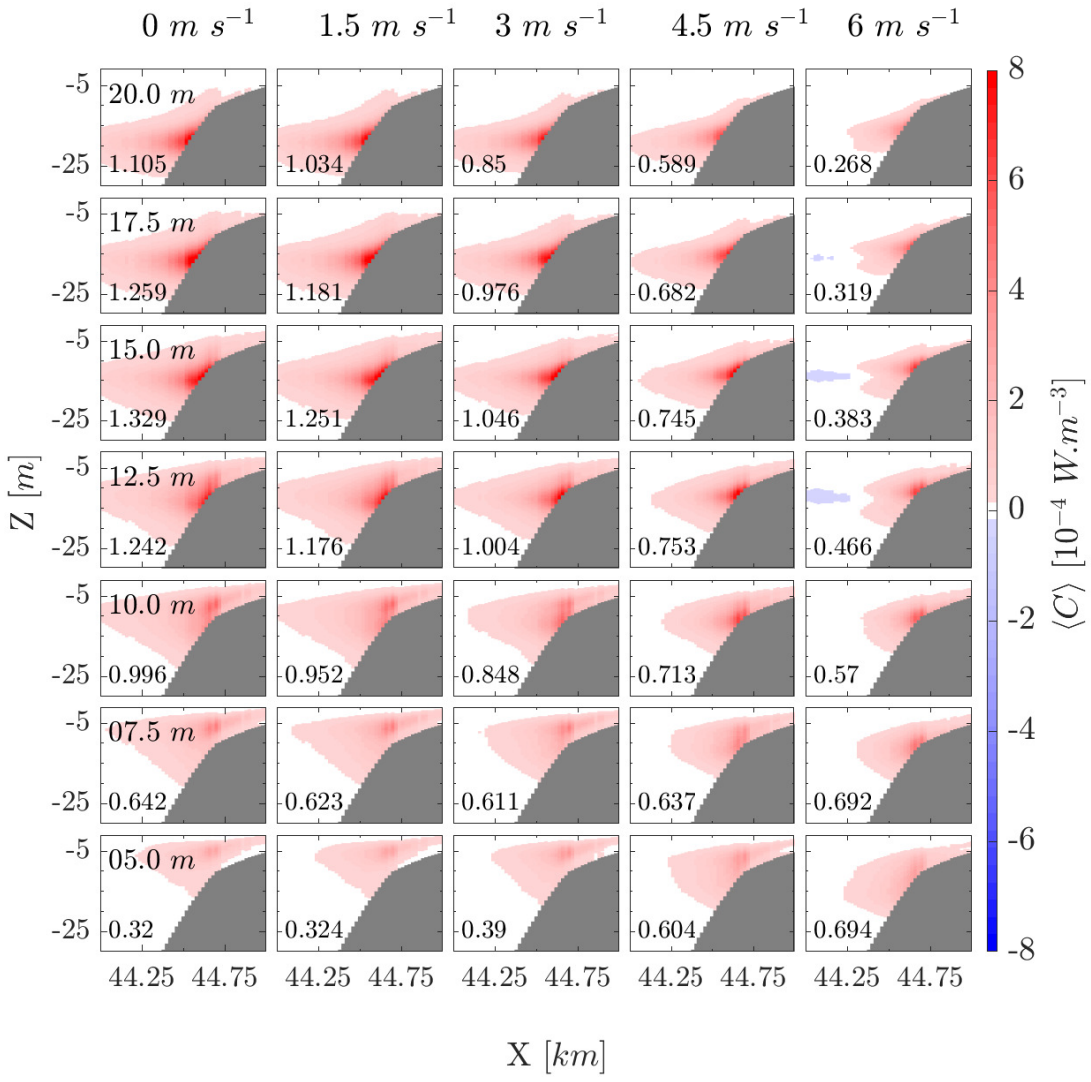

Figure 6.9: The $\langle C \rangle$ structure in the nearshore area is shown for cases perturbed by M_2K_1 tide and XS wind (with a wind speed of 0, 1.5, 3, 4.5 and 6 $m.s^{-1}$) with pycnocline at 5, 7.5, 10, 12.5, 15, 17.5 and 20 meters deep. The total conversion $\widetilde{\overline{\langle C \rangle}}$ values are shown inside each panel.

6.4.3 Wind Speed

The wind speed effect on the conversion is consistent for all pycnocline depth, tidal constituents, and wind-tide phase lag as it does not change the nature of wind-induced perturbations. As shown in Fig 6.10, increasing the wind stress extends the penetration of perturbations caused by wind (especially ρ' as the vertical displacement created by wind is comparable to ones generated by tidal flows) in the water column which results in higher (lower) conversion for cases with constructive (destructive) wind-tide phase lag. The wind speed of 3 m/s enhances the M_2 and K_1 conversion by 10 % and $\pm$ 100 %, while for 6 m/s this contribution exceeds 40 % and $\pm$ 700 % for M_2 and K_1 respectively (Fig 6.7).

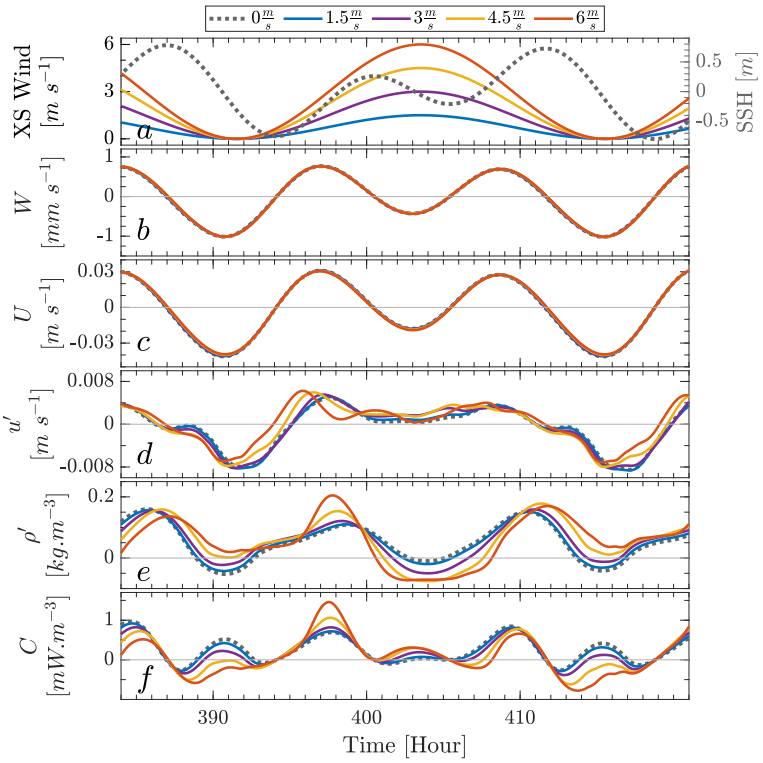

Figure 6.10: The wind speed, BT vertical and horizontal velocities, BC horizontal velocity, density perturbation and conversion rate time-series are shown in the nearshore area for cases perturbed by M_2K_1 tide and XS wind (with a wind speed range of 0, 1.5, 3, 4.5 and 6 $m.s^{-1}$) with pycnocline at 12.5 meters deep. The initial phases of M_2, K_1 and wind are 90°, 144° and 157°.

6.4.4 Nonlinear Interaction

Although most of the complex natural phenomena can be studied by combining simple cases through linear superposition, such a technique might introduce error in a system where nonlinearity is of importance (i.e., coastal shallow water). As an example, as discussed in part I, the tide-tide nonlinear interaction can introduce some error to the linear superposition especially when the pycnocline is shallow

(green bars in Fig 6.11-c). The NTT contribution in comparison to NTW is benign and limited particularly for K_1 and M_2K_1 tidal flow due to their dependency on wind-tide initial phase lag (Fig 6.11-b and c). On the other hand, the NTW for wind-M_2 is significantly smaller especially for cases with pycnocline deeper than 10 meters; yet, discarding the NTW introduces 20 % of error to wind-M_2 conversion (Fig 6.11-a). Moreover, the NTW contribution is negative for all of the tidal constituents when the pycnocline is deeper than 10 meters which emphasizes on the overestimation of conversion using the linear superposition (Fig 6.11). The negative nature of NTW might be due to the double counting of the wind and tide perturbations.

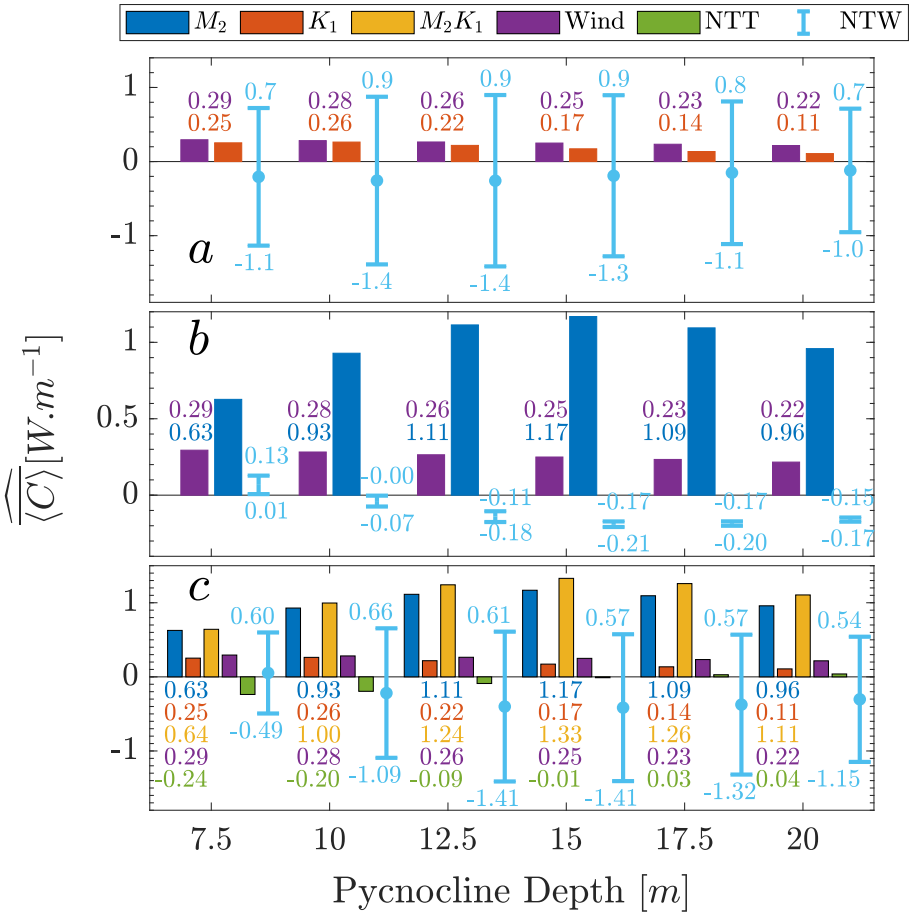

Figure 6.11: The $\widehat{\overline{\langle C \rangle}}$ values for cases perturbed by K_1 (a), M_2 (b) and M_2K_1 (c) as a function pycnocline depth are shown above. The value of nonlinear tide-tide and tide-wind interactions are shown in green bars and light blue error bar (the center is shown with dot) respectively. The initial M_2 and K_1 phases are 90° and 36°.

6.4.5 Mixing & Stability

One of the challenges of modeling and studying the effects of different parameters on the conversion rate is to keep the major configurations steady after each tidal cycle (i.e., the density stratification at the beginning and end of the simulation).

The IW generation in a shallow water system is accompanied by a high amount of mixing and dissipation, which results in modification of the density profile. Given enough time, the stratification in the nearshore area will be weakened, and the strong two-layered dynamics of southern Monterey Bay (strong two-layered system) will be washed away by the repetitive wave overturning. To avoid such mixing, I relaxed the eddy mixing coefficient. Although this decision helps to sustain the configuration, it may impair our results and interpretations for some of the cases. To analyze the tendency of mixing in the system, I employed the Richardson number (Ri), which is beneficial as it compares stabilizing and destabilizing forces ($Ri = N^2/(\frac{\partial u}{\partial z})^2$). Fig 6.12 suggests potential mixing at the generation site for cases with destructive XS wind (fig 6.12-c). On the other hand, for cases with the constructive or neutral wind, the story is different, and the mixing does not necessarily occur on the slope as shown in Fig 6.12-b (the low Ri away from the generation site doesn't affect the generation dynamics over the slope). The negative conversion can be translated as mixing (which agrees well with the Ri or BC to BT energy conversion through pressure-work) [Carter, 2010, Jachec et al., 2006, Kang and Fringer, 2012, Masunaga et al., 2017, Zilberman et al., 2009]). Such realization helps us to understand that the cases with destructive wind might need a re-consideration as these cases suffer from the lack of mixing despite having $Ri < 0.25$. Therefore, I conclude that all the interpretations above hold for cases with positive conversion; yet, the negative conversion might need a revisit and re-modeling. Such a re-modeling is an arduous task as it should keep the density stratification more or less constant after each tidal cycle and allow

for eddy mixing and overturning. Injecting fresh river water at the ocean side boundary and using solar exposure might be a way to resolve this situation. This configuration requires an extensive amount of calibration and testing to ensure stability and accuracy in the model.

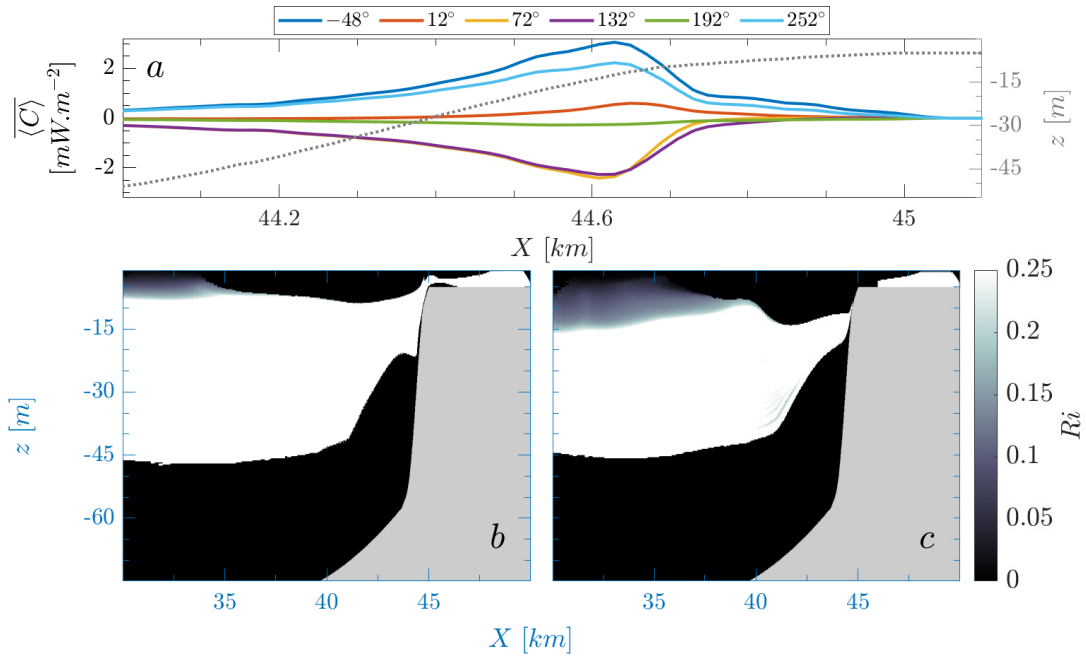

Figure 6.12: The total conversion in the domain as a function of offshore distance is shown in panel a for various cases perturbed by K_1 tidal currents and 6 $m.s^{-1}$ wind with pycnocline at 7.5 meters. Panel b and c show the minimum Richardson number (during the whole process time) for the $\overbrace{\text{wind, tide}} = -48°$ and 72° which has a positive and negative total conversion rate (panel a) respectively.

6.5 Conclusion & Future Work

In this study, I analyzed the different factors affecting the BT to BC energy conversion in the nearshore area for a system governed by XS wind and tidal currents.

The presence of XS wind in the nearshore area promotes the formation of a two-layered shear flow with the zero-crossing of $H/2$ (over the slope) where w and wind are 180° off-phase. The period of M_2 and K_1 governs their interactions with the wind where M_2-wind cases are not sensitive to $\overbrace{\text{tide, wind}}$; while, the K_1-wind conversion highly depends on the phase lag. The pycnocline depth has a manifold effect on the conversion rate as it controls the conversion through steepness ratio, the portion of the water column which contributes to the conversion process, and the wind contribution (as the wind perturbations decline with depth). These factors balance each other at an optimum depth (between 12.5 and 15 meters) where the maximum conversion occurs. The pycnocline effect is not sensitive to the wind speed; in other words, all cases behave similarly despite the wind speed. Increasing the wind speed does not change the system behaviors, and it only exaggerates wind-induced perturbations as it enhances the wind penetration depth. The cases perturbed by M_2K_1 tidal currents show a response, which is a combination of M_2 and K_1 as deepening the pycnocline increases the conversion (M_2 characteristics) and its conversion depends on the wind-tide phase lag (K_1 characteristic). Despite the small nonlinear interaction between K_1 and M_2, the wind-tide nonlinear interaction, NTW, can be significant especially in the presence of K_1 (its a function of wind-tide phase lag) which discourages the linear superposition of wind and tide. To sustain the density stratification in the nearshore area over the processing time, I turned off the eddy mixing, which might negatively impact the cases with the negative conversion rate as their $Ri < 0.25$ (other cases didn't show any tendency to mix over the slope). Therefore, I propose to reconsider these cases using a

model that considers eddy mixing as well as endure the density stratification.

6.6 Acknowledgments

This work was funded by NSF-OCE grant 1416837 to C. Brock Woodson. This study was supported by resources from the Georgia Advanced Computing Resource Center, a partnership between the University of Georgia's Office of the Vice President for Research and Office of the Vice President for Information Technology. All model setup files and analysis scripts are available on Sorush Omidvar GitHub account `https://github.com/somidvar/suntans/tree/master/TideWindPaperSourceCode`

Chapter 7

CONCLUSIONS & FUTURE WORK

This dissertation analyzes barotropic to baroclinic energy conversion in the nearshore area using a robust novel formulation and considers the contribution of diurnal tidal flow as well as the cross-shore diurnal sea breeze in the conversion process. While the first three chapters provide a literature review for internal waves and energy conversion, the other three ones focus on providing an effective conversion formulation using time-variant background density to filter the barotropic tidal heaving, examining the effects of tidal flow (with different periods) interaction on energy conversion, and elucidating the coupling of barotropic tidal flow with the shoreward sea breeze in the inner-shelf region of southern Monterey Bay.

7.1 Contributions

As the statistician George Box says, "*all models are wrong, but some are useful*", I realize the differences between the complex internal wave which are observed in nature and the simplified models that I utilized. However, my formulations and results can shed insight into the dynamics of internal wave generation and interaction in the nearshore area.

The formulations offered by Llewellyn Smith and Young [2002] and Kang and Fringer [2012] suffer from ineffective partitioning of barotropic and baroclinic components, which I addressed in chapter 4. The current formulation offers non-zero energy conversion through time (while its time-average is zero) for a case perturbed by tidal flows with flat topography, while the new method mitigates this issue. Moreover, failure to filter the barotropic tidal heaving of isopycnals (barotropic vertical movements of isopycnals due to surface tides) results in the emergence of residual conversion over the slope (positive) and away from the generation sites (can be positive or negative). The residual conversion is caused by the interaction of internal waves and barotropic vertical movements. Positive conversion is often employed as an indicator to recognize the presence of internal bores and waves as well as their time of arrival (or generation) in the system. Therefore, filtering such residual conversion (under and over-estimation) addresses the beach energy-budget closure problem as well as it allows us to study the energy conversion through time more effectively. My simulations suggest that filtering the barotropic tidal heaving through applying a time-variant background density (which heaves up and down with the barotropic components) can alleviate this issue. Using my

new method removes virtually all of the residual conversion (both positive and negative) at the generation site and away from it. The total conversion in the domain, which can be found through taking time-average and spatial-integral (both depth and cross-shore), gives similar values for all three methods. Therefore, I concluded that the residual conversion, which contains negative values observed away from the generation sites (in this study and others such as Kang and Fringer [2012]), and the overestimation (extra positive conversion) at the slope is mainly due to inefficient partitioning of the energy and can be resolved by using a proper background density function.

Although the semi-diurnal tidal flow has the biggest share in barotropic to baroclinic energy conversion, my results agree with the literature emphasizing the importance of other tidal constituents. The importance of K_1, O_1, and S_2 in the converting energy from barotropic to baroclinic mode has been highlighted by Müller [2013]; however, their interaction in the nearshore area requires more attention. My simulations suggested an energy conversion from 10 % to 50 % by K_1 (in comparison to M_2), and they raise doubt upon the accuracy and validity of linear superposition to study the conversion induced by several linear internal waves (i.e., M_2 and K_1). The energy conversion for a combination of tidal flows (such as M_2K_1) is subjected to not only the primary frequencies (the initial perturbation frequency such as M_2 or K_1), but also the secondary ones which are a combination of primaries. Therefore, the time-averaging process should be done in a way to assure no-residual conversion. Moreover, the data suggests that the tide-tide interaction is not purely linear (especially for cases with a pycnocline

shallower than 10 meters); however, this nonlinear interaction does not depend on tide-tide initial phase lag. The M_2 conversion rate correlates with the wave steepness ratio (rather than the pycnocline depth), while K_1 is not sensitive to this number.

Despite of the Ekman cross-shore transport by the alongshore wind in the mid to outer shelf regions, the cross-shore transport in the inner shelf is driven by the cross-shelf component as the surface and bottom boundaries overlap. Such a realization raises questions about whether or not the onshore wind can affect the energy conversion process. The presence of onshore diurnal sea breeze is documented in the southern Monterey Bay during the summer, which promotes a strong shear velocity in the nearshore area. My results suggest that the M_2 conversion is improved by the wind (discarding the initial wind-tide phase lag), whereas the K_1 tidal flow behavior depends heavily on the wind-tide phase lag. The maximum conversion happens when the tidal flow (U) and the onshore wind stress are 180° off-phase (i.e., when the flood tide and the relaxation of onshore wind coincide), while the minimum happens when they are on-phase (i.e., when the flood tide and maximum onshore wind occur simultaneously). Further analysis showed that this pattern holds for cases with the pycnocline depth of 7.5 to 20 meters. The wind speed does not change the dynamics of the system, and wind intensification only improves the penetration depth of the perturbations, which results in the exaggeration of the wind effects on the conversion.

The presence of internal waves affects the system dynamics and infrastructure installed in the nearshore area. Internal waves can promote instability and over-

turning which results in a significant turbulent mixing and high velocity gradients. Therefore, engineers should avoid building structures susceptible to vibrations and turbulence in the areas which are known for internal wave generation. Moreover, the safety of ocean outfalls that transport the wastewater from land to coasts can be affected by internal waves as they can mix the water and transport the toxic materials shoreward. Hence, accounting for internal wave generation by siting outfalls further offshore where the pycnocline does not interact with the ocean bottom and mixing is relatively lower will reduce the chances of beach contamination and closure.

7.2 Future Work

Although this study deepens our understanding of the tide-tide and wind-tide interactions in converting barotropic to baroclinic energy conversion, further steps are required to take. 1) Upgrading the two-dimensional (and idealized three-dimensional) models used for the time-variant background density to test its efficiency with more realistic topographies and density stratification. 2) Testing the time-variant background density method with the cases perturbed by the wind to examine its efficiency and accuracy in such situations. 3) Combining the first two scenarios and make a robust three-dimensional model of southern Monterey Bay with the presence of cross-shore sea breeze to study the interactions and effects of more complex features on the conversion process such as coastal circulation, surface, and internal waves as well as wind-driven flows.

Bibliography

J. A. Austin and S. J. Lentz. The Inner Shelf Response to Wind-Driven Upwelling and Downwelling*. *Journal of Physical Oceanography*, 32(7):2171–2193, 2002. ISSN 0022-3670. doi: 10.1175/1520-0485(2002)032<2171:tisrtw>2.0.co;2.

P. Baines. The generation of internal tides by flat-bump topography. *Deep Sea Research and Oceanographic Abstracts*, 20(2):179–205, 1973. ISSN 00117471. doi: 10.1016/0011-7471(73)90050-8.

P. Baines. On internal tide generation models. *Deep Sea Research Part A. Oceanographic Research Papers*, 29(3):307–338, 1982. ISSN 01980149. doi: 10.1016/0198-0149(82)90098-X.

P. G. Baines. The reflexion of internal/inertial waves from bumpy surfaces. Part 2. Split reflexion and diffraction. *Journal of Fluid Mechanics*, 49(01):113, 1971a. ISSN 0022-1120. doi: 10.1017/S0022112071001952.

P. G. Baines. The reflexion of internal/inertial waves from bumpy surfaces. *Journal of Fluid Mechanics*, 46(2):273–291, 1971b. ISSN 1469-7645.

P. G. Baines. The generation of internal tides over steep continental slopes. *Philosophical Transactions of the Royal Society of London A: Mathematical, Physical and Engineering Sciences*, 277(1263):27–58, 1974. ISSN 1364-503X.

R. M. Banta, L. D. Olivier, and D. H. Levinson. Evolution of the Monterey Bay Sea-Breeze Layer As Observed by Pulsed Doppler Lidar, 1993. ISSN 0022-4928.

R. T. Barber and F. P. Chavez. Biological consequences of el nino. *Science*, 222 (4629):1203–1210, 1983. ISSN 0036-8075.

R. C. Beardsley, C. E. Dorman, C. A. Friehe, L. K. Rosenfeld, and C. D. Winant. Local atmospheric forcing during the Coastal Ocean Dynamics Experiment: 1. A description of the marine boundary layer and atmospheric conditions over a northern California upwelling region. *Journal of Geophysical Research: Oceans*, 92(C2):1467–1488, 1987. ISSN 2156-2202. doi: 10.1029/JC092iC02p01467.

T. H. Bell. Topographically generated internal waves in the open ocean. *Journal of Geophysical Research*, 80(3):320, 1975. ISSN 0148-0227. doi: 10.1029/JC080i003p00320.

A. B. Boehm, B. F. Sanders, and C. D. Winant. Cross-shelf transport at Huntington Beach. Implications for the fate of sewage discharged through an offshore ocean outfall. *Environmental Science and Technology*, 36(9):1899–1906, 2002. ISSN 0013936X. doi: 10.1021/es0111986.

R. E. Britter and J. E. Simpson. Experiments on the dynamics of a gravity current head. *Journal of Fluid Mechanics*, 88(2):223–240, 1978. ISSN 1469-7645.

J. A. Businger. Turbulence transfer in the atmospheric surface layer. *Workshop on micrometeorology*, pages 67–100, 1973.

G. S. Carter. Barotropic and Baroclinic M 2 Tides in the Monterey Bay Region. *Journal of Physical Oceanography*, 40(8):1766–1783, 2010. ISSN 0022-3670. doi: 10.1175/2010JPO4274.1. URL http://dx.doi.org/10.1175/2010JPO4274.1{%}5Cnhttp://journals.ametsoc.org/doi/abs/10.1175/2010JPO4274.1.

G. S. Carter, M. A. Merrifield, J. M. Becker, K. Katsumata, M. C. Gregg, D. S. Luther, M. D. Levine, T. J. Boyd, and Y. L. Firing. Energetics of M 2 barotropic-to-baroclinic tidal conversion at the Hawaiian Islands. *Journal of Physical Oceanography*, 38(10):2205–2223, 2008. ISSN 1520-0485.

F. P. Chavez, J. T. Pennington, C. G. Castro, J. P. Ryan, R. P. Michisaki, B. Schlining, P. Walz, K. R. Buck, A. McFadyen, and C. A. Collins. Biological and chemical consequences of the 1997-1998 El Niño in central California waters. *Progress in Oceanography*, 54(1-4):205–232, 2002. ISSN 00796611. doi: 10.1016/S0079-6611(02)00050-2.

Z. Chen, J. Xie, D. Wang, J. Zhan, J. Xu, and S. Cai. Density stratification influences on generation of different modes internal solitary waves. *Journal of Geophysical Research: Oceans*, 119(10):7029–7046, 2014. ISSN 2169-9291.

V. P. Chua and O. B. Fringer. Sensitivity analysis of three-dimensional salinity simulations in North San Francisco Bay using the unstructured-grid SUNTANS model. *OCEAN MODELLING*, 39(3-4):332–350, 2011. ISSN 1463-5003. doi: 10.1016/j.ocemod.2011.05.007.

C. Cox and H. Sandstrom. Coupling of internal and surface waves in water of variable depth. *J. Oceanogr. Soc. Japan*, 18:499–513, 1962.

J. P. Crimaldi. The role of structured stirring and mixing on gamete dispersal and aggregation in broadcast spawning. *Journal of Experimental Biology*, 215 (6):1031–1039, 2012. ISSN 00220949. doi: 10.1242/jeb.060145.

J. P. Crimaldi and H. S. Browning. A proposed mechanism for turbulent enhancement of broadcast spawning efficiency. *Journal of Marine Systems*, 49 (1-4):3–18, 2004. ISSN 09247963. doi: 10.1016/j.jmarsys.2003.06.005.

B. Cushman-Roisin and J.-M. Beckers. *Introduction to geophysical fluid dynamics: physical and numerical aspects*. Academic press, 2011. ISBN 0080916783.

A. M. Davies and J. Xing. On the interaction between internal tides and wind-induced near-inertial currents at the shelf edge. *Journal of Geophysical Research C: Oceans*, 108(3):44–1, 2003. ISSN 01480227. doi: 10.1029/2002jc001375.

A. Defant. Die Gezeiten und inneren gezeitenwellen des atlantischen ozeans: ergebenisse der strom und serienmessungen auf den ankerstationen des meteor. 1932.

Y. Dossmann, F. Pollet, P. Odier, and T. Dauxois. Mixing and Formation of Layers by Internal Wave Forcing. *Journal of Geophysical Research: Oceans*, 122(12):9906–9917, 2017. ISSN 21699291. doi: 10.1002/2017JC013309.

C. R. Edwards and H. E. Seim. Complex EOF analysis as a method to sepa-

rate barotropic and baroclinic velocity structure in shallow water. *Journal of Atmospheric and Oceanic Technology*, 25(5):808–821, 2008. ISSN 1520-0426.

G. D. Egbert and R. D. Ray. Significant dissipation of tidal energy in the deep ocean inferred from satellite altimeter data. *Nature*, 405(6788):775–778, 2000. ISSN 00280836. doi: 10.1038/35015531.

G. D. Egbert and R. D. Ray. Estimates of M ₂ tidal energy dissipation from TOPEX/Poseidon altimeter data. *Journal of Geophysical Research: Oceans*, 106(C10):22475–22502, 2001. ISSN 01480227. doi: 10.1029/2000JC000699. URL http://doi.wiley.com/10.1029/2000JC000699.

V. W. Ekman. On the influence of the earth's rotation on ocean-currents. 1905.

C. B. Embling, J. Sharples, E. Armstrong, M. R. Palmer, and B. E. Scott. Fish behaviour in response to tidal variability and internal waves over a shelf sea bank. *Progress in Oceanography*, 117:106–117, 2013. ISSN 00796611. doi: 10.1016/j.pocean.2013.06.013. URL http://dx.doi.org/10.1016/j.pocean.2013.06.013.

M. Fewings, S. J. Lentz, and J. Fredericks. Observations of Cross-Shelf Flow Driven by Cross-Shelf Winds on the Inner Continental Shelf. *Journal of Physical Oceanography*, 38(11):2358–2378, 2008. ISSN 0022-3670. doi: 10.1175/2008jpo3990.1.

O. B. Fringer and Z. Zhang. High-resolution simulations of nonlinear internal gravity waves in the South China Sea. In *DoD HPCMP Users Group Confer-*

ence, 2008. DOD HPCMP UGC, pages 43–46. IEEE, 2008. ISBN 1424433231. doi: 10.1109/DoD.HPCMP.UGC.2008.46.

O. B. Fringer, M. Gerritsen, and R. L. Street. An unstructured-grid, finite-volume, nonhydrostatic, parallel coastal ocean simulator. *Ocean Modelling*, 14(3):139–173, 2006. ISSN 1463-5003.

C. Garrett and E. Kunze. Internal tide generation in the deep ocean. *Annu. Rev. Fluid Mech.*, 39:57–87, 2007. ISSN 0066-4189.

C. Garrett and W. Munk. Internal waves in the ocean. *Annual Review of Fluid Mechanics*, 11(1):339–369, 1979. ISSN 0066-4189.

T. Gerkema, F. P. a. Lam, and L. R. M. Maas. Internal tides in the Bay of Biscay: Conversion rates and seasonal effects. *Deep-Sea Research Part II: Topical Studies in Oceanography*, 51(25-26 SPEC. ISS.):2995–3008, 2004. ISSN 09670645. doi: 10.1016/j.dsr2.2004.09.012.

A. Gill. Atmospheric-ocean dynamics. *Int. Geophys. Ser.*, 30:662, 1982.

W. M. Graham and J. L. Largier. Upwelling shadows as nearshore retention sites: The example of northern Monterey Bay. *Continental Shelf Research*, 17(5): 509–532, 1997. ISSN 02784343. doi: 10.1016/S0278-4343(96)00045-3.

A. T. Greer, R. K. Cowen, C. M. Guigand, J. A. Hare, and D. Tang. The role of internal waves in larval fish interactions with potential predators and prey. *Progress in Oceanography*, 127:47–61, 2014. ISSN 00796611. doi: 10.1016/j.

pocean.2014.05.010. URL http://dx.doi.org/10.1016/j.pocean.2014.05.010.

P. Hall and A. M. Davies. Internal tide modelling and the influence of wind effects. *Continental Shelf Research*, 27(9):1357–1377, 2007. ISSN 02784343. doi: 10.1016/j.csr.2006.09.008.

B. Haurwitz. Internal waves of tidal character. *Eos, Transactions American Geophysical Union*, 31(1):47–52, 1950. ISSN 2324-9250.

T. Hibiya, M. Nagasawa, and Y. Niwa. Nonlinear energy transfer within the oceanic internal wave spectrum at mid and high latitudes. *Journal of Geophysical Research C: Oceans*, 107(11):28–1, 2002. ISSN 01480227. doi: 10.1029/2001jc001210.

B. Hickey, S. Geier, N. Kachel, and A. MacFadyen. A bi-directional river plume: The Columbia in summer. *Continental Shelf Research*, 25(14):1631–1656, 2005. ISSN 02784343. doi: 10.1016/j.csr.2005.04.010.

P. M. Holligan, R. D. Pingree, and G. T. Mardell. Oceanic solitons, nutrient pulses and phytoplankton growth. *Nature*, 314(6009):348–350, 1985. ISSN 1476-4687.

P. E. Holloway and M. A. Merrifield. Internal tide generation by seamounts, ridges, and islands. *Journal of Geophysical Research: Oceans*, 104(C11):25937–25951, 1999. ISSN 2156-2202.

P. Hosegood and H. Van Haren. Near-bed solibores over the continental slope in the Faeroe-Shetland Channel. *Deep-Sea Research Part II: Topical Studies*

in Oceanography, 51(25-26 SPEC. ISS.):2943–2971, 2004. ISSN 09670645. doi: 10.1016/j.dsr2.2004.09.016.

M. E. Inall, T. P. Rippeth, and T. J. Sherwin. Impact of nonlinear waves on the dissipation of internal tidal energy at a shelf break. *Journal of Geophysical Research: Oceans*, 105(C4):8687–8705, apr 2000. ISSN 01480227. doi: 10.1029/1999JC900299. URL http://doi.wiley.com/10.1029/1999JC900299.

S. M. Jachec, O. B. Fringer, M. G. Gerritsen, and R. L. Street. Numerical simulation of internal tides and the resulting energetics within Monterey Bay and the surrounding area. *Geophysical Research Letters*, 33(12):2–5, 2006. ISSN 00948276. doi: 10.1029/2006GL026314.

S. M. Jachec, O. B. Fringer, R. L. Street, and M. G. Gerritsen. Effects of grid resolution on the simulation of internal tides. *International Journal of Offshore and Polar Engineering*, 17(02):432–438, 2007. ISSN 1053-5381.

S. Jan, R. C. Lien, and C. H. Ting. Numerical study of baroclinic tides in Luzon Strait. *Journal of Oceanography*, 64(5):789–802, 2008. ISSN 09168370. doi: 10.1007/s10872-008-0066-5.

C. Jantzen, G. M. Schmidt, C. Wild, C. Roder, S. Khokiattiwong, and C. Richter. Benthic reef primary production in response to large amplitude internal waves at the Similan Islands (Andaman Sea, Thailand). *PLoS ONE*, 8(11):1–15, 2013. ISSN 19326203. doi: 10.1371/journal.pone.0081834.

K. S. Johnson, F. P. Chavez, and G. E. Friederich. Continental-shelf sediment as

a primary source of iron for coastal phytoplankton. *Nature*, 398(6729):697–700, 1999. ISSN 1476-4687.

S. Kaartvedt, T. A. Klevjer, and D. L. Aksnes. Internal wave-mediated shading causes frequent vertical migrations in fishes. *Marine Ecology Progress Series*, 452:1–10, 2012. ISSN 01718630. doi: 10.3354/meps09688.

D. Kang. *Energetics and Dynamics of Internal Tides in Monterey Bay Using Numerical Simulations a Dissertation Submitted To the Department of Civil and Environmental Engineering and the Committee on Graduate Studies of Stanford University in Partial Fulfillment of*. PhD thesis, Stanford university, 2010.

D. Kang and O. Fringer. On the Calculation of Available Potential Energy in Internal Wave Fields. *Journal of Physical Oceanography*, 40(11):2539–2545, 2010. ISSN 0022-3670. doi: 10.1175/2010JPO4497.1.

D. Kang and O. Fringer. Energetics of Barotropic and Baroclinic Tides in the Monterey Bay Area. *Journal of Physical Oceanography*, 42(2):272–290, feb 2012. ISSN 0022-3670. doi: 10.1175/JPO-D-11-039.1.

S. M. Kelly and J. D. Nash. Internal-tide generation and destruction by shoaling internal tides. *Geophysical Research Letters*, 37(23):1–5, 2010. ISSN 00948276. doi: 10.1029/2010GL045598.

S. M. Kelly, J. D. Nash, and E. Kunze. Internal-tide energy over topography. *Journal of Geophysical Research: Oceans*, 115(6):1–13, 2010. ISSN 21699291. doi: 10.1029/2009JC005618.

A. R. Kirincich, J. A. Barth, B. A. Grantham, B. A. Menge, and J. Lubchenco. Wind-driven inner-shelf circulation off central Oregon during summer. *Journal of Geophysical Research C: Oceans*, 110(10):1–17, 2005. ISSN 01480227. doi: 10.1029/2004JC002611.

J. M. Klymak and J. N. Moum. Internal solitary waves of elevation advancing on a shoaling shelf. *Geophysical Research Letters*, 30(20):8–11, 2003. ISSN 00948276. doi: 10.1029/2003GL017706.

J. M. Klymak, J. N. Moum, J. D. Nash, E. Kunze, J. B. Girton, G. S. Carter, C. M. Lee, T. B. Sanford, and M. C. Gregg. An Estimate of Tidal Energy Lost to Turbulence at the Hawaiian Ridge. *Journal of Physical Oceanography*, 36 (6):1148–1164, 2006. ISSN 0022-3670. doi: 10.1175/JPO2885.1. URL `http://journals.ametsoc.org/doi/abs/10.1175/JPO2885.1`.

P. Kundu, I. Cohen, and D. Dowling. *Fluid Mechanics*. Elsevier, 5 edition, 2012. ISBN 978-0123821003.

E. Kunze, L. K. Rosenfeld, G. S. Carter, and M. C. Gregg. Internal Waves in Monterey Submarine Canyon. *Journal of Physical Oceanography*, 32(6): 1890–1913, 2002. ISSN 0022-3670. doi: 10.1175/1520-0485(2002)032<1890: IWIMSC>2.0.CO;2.

A. L. Kurapov, G. D. Egbert, J. S. Allen, R. N. Miller, S. Y. Erofeeva, and P. M. Kosro. The M2 internal tide off Oregon: Inferences from data assimilation. *Journal of Physical Oceanography*, 33(8):1733–1757, 2003. ISSN 00223670. doi: 10.1175/2397.1.

A. L. Kurapov, J. S. Allen, and G. D. Egbert. Combined Effects of Wind-Driven Upwelling and Internal Tide on the Continental Shelf. *Journal of Physical Oceanography*, 40(4):737–756, 2009. ISSN 0022-3670. doi: 10.1175/2009jpo4183.1.

A. L. Shanks and W. G. Wright. Internal-wave-mediated shoreward transport of cyprids, megalopae, and gammarids and correlated longshore differences in the settling rate of intertidal barnacles. *Journal of Experimental Marine Biology and Ecology*, 114(1):1–13, 1987. ISSN 00220981. doi: 10.1016/0022-0981(87)90135-3.

L. B. Ladah, F. J. Tapia, J. Pineda, and M. López. Spatially heterogeneous, synchronous settlement of Chthamalus spp. larvae in northern Baja California. *Marine Ecology Progress Series*, 302(May):177–185, 2005. ISSN 01718630. doi: 10.3354/meps302177.

Z. Lai, C. Chen, G. W. Cowles, and R. C. Beardsley. A nonhydrostatic version of FVCOM: 1. Validation experiments. *Journal of Geophysical Research: Oceans*, 115(11):1–23, 2010. ISSN 21699291. doi: 10.1029/2009JC005525.

K. G. Lamb. Energy and pseudoenergy flux in the internal wave field generated by tidal flow over topography. *Continental Shelf Research*, 27(9):1208–1232, 2007. ISSN 02784343. doi: 10.1016/j.csr.2007.01.020.

W. G. Large and S. Pond. Open ocean momentum flux measurements in moderate to strong winds. *Journal of physical oceanography*, 11(3):324–336, 1981. ISSN 1520-0485.

J. J. Leichter, S. R. Wing, S. L. Miller, and M. W. Denny. Pulsed delivery of subthermocline water to Conch Reef (Florida Keys) by internal tidal bores. *Limnology and Oceanography*, 41(7):1490–1501, 1996. ISSN 00243590. doi: 10.4319/lo.1996.41.7.1490.

J. J. Leichter, G. Shellenbarger, S. J. Genovese, and S. R. Wing. Breaking internal waves on a Florida (USA) coral reef: A plankton pump at work? *Marine Ecology Progress Series*, 166:83–97, 1998. ISSN 01718630. doi: 10.3354/meps166083.

S. J. Lentz. The Influence of Stratification on the Wind-Driven Cross-Shelf Circulation over the North Carolina Shelf*. *Journal of Physical Oceanography*, 31 (9):2749–2760, 2002. ISSN 0022-3670. doi: 10.1175/1520-0485(2001)031<2749: tiosot>2.0.co;2.

S. J. Lentz and J. Largier. The Influence of Wind Forcing on the Chesapeake Bay Buoyant Coastal Current*. *Journal of Physical Oceanography*, 36(7):1305–1316, 2006. ISSN 0022-3670. doi: 10.1175/jpo2909.1.

R.-C. Lien, F. Henyey, B. Ma, and Y. J. Yang. Large-Amplitude Internal Solitary Waves Observed in the Northern South China Sea: Properties and Energetics. *Journal of Physical Oceanography*, 44(4):1095–1115, 2014. ISSN 0022-3670. doi: 10.1175/JPO-D-13-088.1. URL `http://journals.ametsoc.org/doi/abs/10.1175/JPO-D-13-088.1`.

K. Lim, G. N. Ivey, and R. I. Nokes. The generation of internal waves by tidal flow over continental shelf/slope topography. *Environmental Fluid Mechanics*, 8(5-6):511–526, 2008. ISSN 15677419. doi: 10.1007/s10652-008-9085-4.

G. Liu and V. P. Chua. A SUNTANS-based unstructured grid local exact particle tracking model. *OCEAN DYNAMICS*, 66(6-7):811–821, jul 2016. ISSN 1616-7341. doi: 10.1007/s10236-016-0952-0.

K. Liu, Z. Xu, and B. Yin. Three-dimensional numerical simulation of internal tides that radiated from the Luzon Strait into the Western Pacific. *Chinese journal of oceanology and limnology*, 35(6):1275–1286, 2017. ISSN 0254-4059.

S. G. Llewellyn Smith and W. R. Young. Conversion of the barotropic tide. *Journal of Physical Oceanography*, 32(5):1554–1566, 2002. ISSN 00223670. doi: 10.1175/1520-0485(2002)032<1554:COTBT>2.0.CO;2.

M. S. Longuet-Higgins. On the trapping of long-period waves round islands. *Journal of Fluid Mechanics*, 37(4):773–784, 1969. ISSN 1469-7645.

E. N. Lorenz. Available potential energy and the maintenance of the general circulation. *Tellus*, 7(2):157–167, 1955. ISSN 0040-2826.

Y. Lu, D. G. Wright, and D. Brickman. Internal tide generation over topography: Experiments with a free-surface z-level ocean model. *Journal of Atmospheric and Oceanic Technology*, 18(6):1076–1091, 2001. ISSN 07390572. doi: 10.1175/1520-0426(2001)018<1076:ITGOTE>2.0.CO;2.

L. R. Maas. Topographies lacking tidal conversion. *Journal of Fluid Mechanics*, 684:5–24, 2011. ISSN 00221120. doi: 10.1017/jfm.2011.245.

P. MacCready and S. N. Giddings. The Mechanical Energy Budget of a Regional Ocean Model. *Journal of Physical Oceanography*, 46(9):2719–2733, 2016. ISSN

0022-3670. doi: 10.1175/JPO-D-16-0086.1. URL http://journals.ametsoc.org/doi/10.1175/JPO-D-16-0086.1.

J. A. MacKinnon and K. B. Winters. Spectral evolution of bottom-forced internal waves. *Proceedings of the 13th'Aha Huliko'a Hawaiian Winter Workshop on Near Boundary Processes and their Parameterization*, pages 73–83, 2003.

E. Masunaga, O. B. Fringer, and H. Yamazaki. An observational and numerical study of river plume dynamics in Otsuchi Bay, Japan. *Journal of Oceanography*, 72(1):1–19, feb 2015. ISSN 0916-8370. doi: 10.1007/s10872-015-0324-2.

E. Masunaga, O. B. Fringer, Y. Kitade, H. Yamazaki, and S. M. Gallager. Dynamics and energetics of trapped diurnal internal Kelvin waves around a Midlatitude Island. *Journal of Physical Oceanography*, 47(10):2479–2498, oct 2017. ISSN 15200485. doi: 10.1175/JPO-D-16-0167.1.

E. E. McPhee-Shaw, D. A. Siegel, L. Washburn, M. A. Brzezinski, J. L. Jones, A. Leydecker, and J. Melack. Mechanisms for nutrient delivery to the inner shelf: Observations from the Santa Barbara Channel. *Limnology and Oceanography*, 52(5):1748–1766, 2007. ISSN 00243590 (ISSN). doi: 10.4319/lo.2007.52.5.1748. URL http://doi.wiley.com/10.4319/lo.2007.52.5.1748.

M. A. Merrifield and P. E. Holloway. Model estimates of M2 internal tide energetics at the Hawaiian Ridge. *Journal of Geophysical Research: Oceans*, 107(C8), 2002. ISSN 2156-2202.

M. A. Merrifield, P. E. Holloway, and T. M. S. Johnston. The generation of internal

tides at the Hawaiian ridge. *Geophysical Research Letters*, 28(4):559–562, 2001. ISSN 00948276. doi: 10.1029/2000GL011749.

X. Ming and V. P. Chua. Three-Dimensional Hydrodynamic Modeling of Singapore Coastal Waters on an Unstructured- Grid SUNTANS Model. In *OCEANS 2014 - TAIPEI*, OCEANS-IEEE, 2014. ISBN 978-1-4799-3646-5.

J. N. Moum, J. M. Klymak, J. D. Nash, A. Perlin, and W. D. Smyth. Energy Transport by Nonlinear Internal Waves. *Journal of Physical Oceanography*, 37 (7):1968–1988, 2007. ISSN 0022-3670. doi: 10.1175/JPO3094.1.

M. Müller. On the space-and time-dependence of barotropic-to-baroclinic tidal energy conversion. *Ocean Modelling*, 72:242–252, 2013. ISSN 1463-5003.

W. Munk and C. Wunsch. Abyssal recipes II: Energetics of tidal and wind mixing. *Deep-Sea Research Part I: Oceanographic Research Papers*, 45(12):1977–2010, 1998. ISSN 09670637. doi: 10.1016/S0967-0637(98)00070-3.

F. Nansen. *The Norwegian North Polar Expedition, 1893-1896: Scientific Results*, volume 6. Longmans, Green and Company, 1905.

J. D. Nash and J. N. Moum. River plumes as a source of large-amplitude internal waves in the coastal ocean. *Nature*, 437(7057):400–403, 2005. ISSN 1476-4687. doi: 10.1038/nature03936. URL `http://dx.doi.org/10.1038/nature03936`.

J. D. Nash, S. M. Kelly, E. L. Shroyer, J. N. Moum, and T. F. Duda. The Unpredictable Nature of Internal Tides on the Continental Shelf. *Journal of*

Physical Oceanography, page 120627081124007, 2012. ISSN 0022-3670. doi: 10.1175/JPO-D-12-028.1.

Nash, J.D., E.L. Shroyer, S.M. Kelly, M.E. Inall, T.F. Duda, M.D. Levine, N.L. Jones and R. Musgrave. Are any coastal internal tides predictable? *Oceanography*, 2012.

V. Nelko, A. Saha, and V. P. Chua. On the tidally driven circulation in the South China Sea: modeling and analysis. *OCEAN DYNAMICS*, 64(3):413–428, mar 2014. ISSN 1616-7341. doi: 10.1007/s10236-013-0687-0.

Y. Niwa and T. Hibiya. Numerical study of the spatial distribution of the M2 internal tide in the Pacific Ocean. *Journal of Geophysical Research: Oceans*, 106(C10):22441–22449, 2001. ISSN 2156-2202.

Y. Niwa and T. Hibiya. Three-dimensional numerical simulation of M2 internal tides in the East China Sea. *Journal of Geophysical Research*, 109(C4):C04027, 2004. ISSN 0148-0227. doi: 10.1029/2003JC001923. URL http://doi.wiley.com/10.1029/2003JC001923{%}5Cnhttp://onlinelibrary.wiley.com/doi/10.1029/2003JC001923/full.

T. R. Osborn. Estimates of the Local Rate of Vertical Diffusion from Dissipation Measurements, 1980. ISSN 0022-3670.

J. J. Osborne, A. L. Kurapov, G. D. Egbert, and P. M. Kosro. Spatial and temporal variability of the M 2 internal tide generation and propagation on the

Oregon shelf. *Journal of Physical Oceanography*, 41(11):2037–2062, 2011. ISSN 0022-3670.

J. D. Paduan and L. K. Rosenfeld. Remotely sensed surface currents in Monterey Bay from shore-based HF radar (Coastal Ocean Dynamics Application Radar). *Journal of Geophysical Research: Oceans*, 101(C9):20669–20686, 1996. ISSN 01480227. doi: 10.1029/96JC01663. URL `http://doi.wiley.com/10.1029/96JC01663`.

M. R. Palmer, G. R. Stephenson, M. E. Inall, C. Balfour, A. Düsterhus, and J. A. M. Green. Turbulence and mixing by internal waves in the Celtic Sea determined from ocean glider microstructure measurements. *Journal of Marine Systems*, 144:57–69, 2015.

E. T. Petruncio, L. K. Rosenfeld, and J. D. Paduan. Observations of the Internal Tide in Monterey Canyon. *Journal of Physical Oceanography*, 28(10):1873–1903, 1998. ISSN 0022-3670. doi: 10.1175/1520-0485(1998)028<1873:OOTITI>2.0.CO;2.

A. Pickering, M. Alford, J. Nash, L. Rainville, M. Buijsman, D. S. Ko, and B. Lim. Structure and variability of internal tides in Luzon Strait. *Journal of Physical Oceanography*, 45(6):1574–1594, 2015. ISSN 15200485. doi: 10.1175/JPO-D-14-0250.1.

J. Pineda. Predictable upwelling and the shoreward transport of planktonic larvae by internal tidal bores. *Science (New York, N.Y.)*, 253(5019):548–549, 1991. ISSN 0036-8075. doi: 10.1126/science.253.5019.548.

J. Pineda. Internal tidal bores in the nearshore: Warm-water fronts, seaward gravity currents and the onshore transport of neustonic larvae. *Journal of Marine Research*, 52(3):427–458, 1994. ISSN 00222402. doi: 10.1357/0022240943077046.

J. Pineda. An internal tidal bore regime at nearshore stations along western U.S.A.: Predictable upwelling within the lunar cycle. *Continental Shelf Research*, 15(8):1023–1041, 1995. ISSN 02784343. doi: 10.1016/0278-4343(95)80007-Z.

J. Pineda. Circulation and larval distribution in internal tidal bore warm fronts. *Limnology and Oceanography*, 44(6):1400–1414, 1999. ISSN 00243590. doi: 10.4319/lo.1999.44.6.1400.

F. Pollmann, J. Nycander, C. Eden, and D. Olbers. Resolving the horizontal direction of internal tide generation. *Journal of Fluid Mechanics*, 864:381–407, 2019. ISSN 14697645. doi: 10.1017/jfm.2019.9.

L. Rainville and R. Pinkel. Propagation of Low-Mode Internal Waves through the Ocean. *Journal of Physical Oceanography*, 36(6):1220–1236, 2006. ISSN 0022-3670. doi: 10.1175/JPO2889.1. URL `http://journals.ametsoc.org/doi/abs/10.1175/JPO2889.1`.

K. A. Raskoff. The impact of El Niño events on populations of mesopelagic hydromedusae BT - Jellyfish Blooms: Ecological and Societal Importance. pages 121–129, Dordrecht, 2001. Springer Netherlands. ISBN 978-94-010-0722-1.

M. Rattray, J. G. Dworski, and P. E. Kovala. Generation of long internal waves at continental slope. *Deep-Sea Research*, page 179, 1969.

M. Rattray Jr. Propagation and dissipation of long internal waves. *Eos, Transactions American Geophysical Union*, 38(4):495–500, 1957. doi: 10.1029/TR038i004p00495. URL https://agupubs.onlinelibrary.wiley.com/doi/abs/10.1029/TR038i004p00495.

M. Rattray Jr. On the Coastal Generation of Internal Tides. *Tellus A*, 1(232), 1960. ISSN 0280-6495. doi: 10.3402/tellusa.v12i1.9344.

M. D. Rayson, G. N. Ivey, N. L. Jones, and O. B. Fringer. Resolving high-frequency internal waves generated at an isolated coral atoll using an unstructured grid ocean model. *OCEAN MODELLING*, 122:67–84, feb 2018. ISSN 1463-5003. doi: 10.1016/j.ocemod.2017.12.007.

L. K. Rosenfeld, F. B. Schwing, N. Garfield, and D. E. Tracy. Bifurcated flow from an upwelling source: a cold water source for Monterey Bay. *Cont. Shelf Res.*, 14(9):931–964, 1994.

H. Sandstrom. Effect of topography on propagation of waves in stratified fluids. In *Deep Sea Research and Oceanographic Abstracts*, volume 16, pages 405–410. Elsevier, 1969. ISBN 0011-7471.

A. Scotti, R. Beardsley, and B. Butman. On the interpretation of energy and energy fluxes of nonlinear internal waves: An example from Massachusetts Bay.

Journal of Fluid Mechanics, 561:103–112, 2006. ISSN 00221120. doi: 10.1017/S0022112006000991.

A. Shanks. Surface slicks associated with tidally forced internal waves may transport pelagic larvae of benthic invertebrates and fishes shoreward . *Marine Ecology Progress Series*, 13:311–315, 1983. ISSN 0171-8630. doi: 10.3354/meps013311.

A. L. Shanks. Tidal periodicity in the daily settlement of intertidal barnacle larvae and an hypothesized mechanism for the cross-shelf transport of cyprids. *The Biological Bulletin*, 170(3):429–440, 1986. ISSN 0006-3185.

J. Sharples, J. F. Tweddle, J. A. Green, M. R. Palmer, Y.-N. Y. N. Kim, A. E. Hickman, P. M. Holligan, C. M. Moore, T. P. Rippeth, J. H. Simpson, V. Krivtsov, J. A. Mattias Green, M. R. Palmer, Y.-N. Y. N. Kim, A. E. Hickman, P. M. Holligan, C. M. Moore, T. P. Rippeth, J. H. Simpson, and V. Krivtsov. Spring-neap modulation of internal tide mixing and vertical nitrate fluxes at a shelf edge in summer. *Limnology and Oceanography*, 52(5):1735–1747, 2007. ISSN 00243590. doi: 10.4319/lo.2007.52.5.1735.

R. E. Shea and W. W. Broenkow. The role of internal tides in the nutrient enrichment of Monterey Bay, California. *Estuarine, Coastal and Shelf Science*, 15(1):57–66, 1982. ISSN 02727714 (ISSN). doi: 10.1016/0272-7714(82)90036-1. URL `http://www.scopus.com/inward/record.url?eid=2-s2.0-0020336021{&}partnerID=40{&}md5=d7630c2acccd646e9578fc3c994419d0`.

E. L. Shroyer, J. N. Moum, and J. D. Nash. Energy transformations and dissipation of nonlinear internal waves over New Jersey's continental shelf. *Nonlinear Processes in Geophysics*, 17(4):345–360, 2010. ISSN 10235809. doi: 10.5194/npg-17-345-2010.

H. L. Simmons, R. W. Hallberg, and B. K. Arbic. Internal wave generation in a global baroclinic tide model. *Deep-Sea Research Part II: Topical Studies in Oceanography*, 51(25-26 SPEC. ISS.):3043–3068, 2004. ISSN 09670645. doi: 10.1016/j.dsr2.2004.09.015.

J. E. Smith, C. M. Smith, P. S. Vroom, K. L. Beach, and S. Miller. Nutrient and growth dynamics of Halimeda tuna on Conch Reef, Florida Keys: Possible influence of internal tides on nutrient status and physiology. *Limnology and Oceanography*, 49(6):1923–1936, 2004. ISSN 00243590. doi: 10.4319/lo.2004.49.6.1923.

K. A. Smith, M. A. Merrifield, and G. S. Carter. Coastal-trapped behavior of the diurnal internal tide at O'ahu, H awai'i. *Journal of Geophysical Research: Oceans*, 122(5):4257–4273, 2017. ISSN 2169-9275.

R. K. Smith, G. Roff, and N. Crook. The Morning Glory: An extraordinary atmospheric undular bore. *Quarterly Journal of the Royal Meteorological Society*, 108(458):937–956, 1982. ISSN 1477870X. doi: 10.1002/qj.49710845813.

L. C. St. Laurent and C. Garrett. The role of internal tides in mixing the deep ocean. *Journal of Physical Oceanography*, 32(10):2882–2899, 2002. ISSN 00223670. doi: 10.1175/1520-0485(2002)032<2882:TROITI>2.0.CO;2.

S. H. Suanda, J. A. Barth, and C. B. Woodson. Diurnal heat balance for the northern Monterey Bay inner shelf. *Journal of Geophysical Research: Oceans*, 116(9):1–13, 2011. ISSN 21699291. doi: 10.1029/2010JC006894.

Y. Tanaka, T. Hibiya, Y. Niwa, and N. Iwamae. Numerical study of K1 internal tides in the Kuril straits. *Journal of Geophysical Research: Oceans*, 115(9): 1–13, 2010. ISSN 21699291. doi: 10.1029/2009JC005903.

S. A. Thorpe. On the interactions of internal waves reflecting from slopes. *Journal of Physical Oceanography*, 27(9):2072–2078, 1997. ISSN 00223670. doi: 10.1175/1520-0485(1997)027<2072:OTIOIW>2.0.CO;2.

C. E. Tilburg. Across-Shelf Transport on a Continental Shelf: Do Across-Shelf Winds Matter? *Journal of Physical Oceanography*, 33(12):2675–2688, 2003. ISSN 0022-3670. doi: 10.1175/1520-0485(2003)033<2675:atoacs>2.0.co;2.

H. Van Haren, L. Maas, J. T. Zimmerman, H. Ridderinkhof, and H. Malschaert. Strong inertial currents and marginal internal wave stability in the central North Sea. *Geophysical Research Letters*, 26(19):2993–2996, 1999. ISSN 00948276. doi: 10.1029/1999GL002352.

H. van Haren, L. Maas, and H. van Aken. Correction to "On the nature of internal wave spectra near a continental slope". *Geophysical Research Letters*, 30(7):57–59, 2003. ISSN 00948276. doi: 10.1029/2003gl016952.

H. van Haren, L. Gostiaux, M. Laan, M. van Haren, E. van Haren, and L. J.

Gerringa. Internal wave turbulence near a texel beach. *PLoS ONE*, 7(3):3–7, 2012. ISSN 19326203. doi: 10.1371/journal.pone.0032535.

S. K. Venayagamoorthy and O. B. Fringer. Nonhydrostatic and nonlinear contributions to the energy flux budget in nonlinear internal waves. *Geophysical Research Letters*, 32(15):1–5, 2005. ISSN 00948276. doi: 10.1029/2005GL023432.

V. Vlasenko, N. Stashchuk, and K. Hutter. *Baroclinic tides: theoretical modeling and observational evidence*. Cambridge University Press, 2005. ISBN 113944607X.

R. K. Walter, C. B. Woodson, R. S. Arthur, O. B. Fringer, and S. G. Monismith. Nearshore internal bores and turbulent mixing in southern Monterey Bay. *Journal of Geophysical Research: Oceans*, 117(C7), 2012. ISSN 2156-2202.

R. K. Walter, M. E. Squibb, C. B. Woodson, J. R. Koseff, and S. G. Monismith. Stratified turbulence in the nearshore coastal ocean: Dynamics and evolution in the presence of internal bores. *Journal of Geophysical Research: Oceans*, 119 (12):8709–8730, 2014. ISSN 2169-9291.

B. Wang, O. B. Fringer, S. N. Giddings, and D. A. Fong. High-resolution simulations of a macrotidal estuary using SUNTANS. *OCEAN MODELLING*, 26 (1-3, SI):60–85, 2009. ISSN 1463-5003. doi: 10.1016/j.ocemod.2008.08.008.

B. Wang, S. N. Giddings, O. B. Fringer, E. S. Gross, D. A. Fong, and S. G. Monismith. Modeling and understanding turbulent mixing in a macrotidal salt

wedge estuary. *JOURNAL OF GEOPHYSICAL RESEARCH-OCEANS*, 116, feb 2011. ISSN 0148-0227. doi: 10.1029/2010JC006135.

J. G. Weigand, H. G. Farmer, S. J. Prinsenberg, and M. Rattray. Effects of friction and surface tide angle of incidence on the coastal generation of internal tides. 1969.

K. B. Winters, P. N. Lombard, J. J. Riley, and E. A. D'Asaro. Available potential energy and mixing in density-stratified fluids. *Journal of Fluid Mechanics*, 289: 115–128, 1995. ISSN 1469-7645.

C. B. Woodson. Spatiotemporal Variation in Cross-Shelf Exchange across the Inner Shelf of Monterey Bay, California. *Journal of Physical Oceanography*, 43 (8):1648–1665, 2013. ISSN 0022-3670. doi: 10.1175/JPO-D-11-0185.1.

C. B. Woodson. The fate and impact of internal waves in nearshore ecosystems. *Annual review of marine science*, 10:421–441, 2018. ISSN 1941-1405.

C. B. Woodson, D. I. Eerkes-Medrano, A. Flores-Morales, M. M. Foley, S. K. Henkel, M. Hessing-Lewis, D. Jacinto, L. Needles, M. T. Nishizaki, J. O'Leary, C. E. Ostrander, M. Pespeni, K. B. Schwager, J. A. Tyburczy, K. A. Weersing, A. R. Kirincich, J. A. Barth, M. A. McManus, and L. Washburn. Local diurnal upwelling driven by sea breezes in northern Monterey Bay. *Continental Shelf Research*, 27(18):2289–2302, 2007. ISSN 02784343. doi: 10.1016/j.csr.2007.05.014.

C. B. Woodson, J. A. Barth, O. M. Cheriton, M. A. McManus, J. P. Ryan,

L. Washburn, K. N. Carden, B. S. Cheng, J. Fernandes, and L. E. Garske. Observations of internal wave packets propagating along-shelf in northern Monterey Bay. *Geophysical Research Letters*, 38(1), 2011. ISSN 1944-8007.

J. Xie, J. Pan, and D. A. Jay. Multimodal internal waves generated over a subcritical ridge: Impact of the upper-ocean stratification. *Journal of Physical Oceanography*, 45(3):904–926, 2015. ISSN 0022-3670.

J. Xing and A. M. Davies. The influence of wind effects upon internal tides in shelf edge regions. *Journal of Physical Oceanography*, 27(10):2100–2125, 1997. ISSN 1520-0485.

J. Xing and A. M. Davies. Processes influencing the non-linear interaction between inertial oscillations, near inertial internal waves and internal tides. *Geophysical Research Letters*, 29(5):11–1–11–4, 2002. ISSN 0094-8276. doi: 10.1029/2001gl014199.

M. Xu and V. P. Chua. A numerical study on circulation and volume transport in Singapore coastal waters. *JOURNAL OF HYDRO-ENVIRONMENT RESEARCH*, 12:70–90, sep 2016. ISSN 1570-6443. doi: 10.1016/j.jher.2015.11.005.

M. Xu and V. P. Chua. A numerical study on land-based pollutant transport in Singapore coastal waters with a coupled hydrologic-hydrodynamic model. *JOURNAL OF HYDRO-ENVIRONMENT RESEARCH*, 14:119–142, mar 2017. ISSN 1570-6443. doi: 10.1016/j.jher.2016.09.002.

L. D. Zeidberg, W. M. Hamner, N. P. Nezlin, and A. Henry. The fishery for

California market squid (Loligo opalescens) (Cephalopoda: Myopsida), from 1981 through 2003. *Fishery Bulletin*, 104(1):46–59, 2006. ISSN 00900656.

Y. Zhang, J. G. Bellingham, J. P. Ryan, B. Kieft, and M. J. Stanway. Autonomous Four-Dimensional Mapping and Tracking of a Coastal Upwelling Front by an Autonomous Underwater Vehicle. *Journal of Field Robotics*, 33(1):67–81, 2016. ISSN 1556-4967. doi: 10.1002/rob.21617.

Z. Zhang, O. B. Fringer, and S. R. Ramp. Three-dimensional, nonhydrostatic numerical simulation of nonlinear internal wave generation and propagation in the South China Sea. *Journal of Geophysical Research: Oceans*, 116(C5), may 2011. ISSN 2156-2202. doi: 10.1029/2010JC006424.

N. V. Zilberman, J. M. Becker, M. a. Merrifield, and G. S. Carter. Model Estimates of M 2 Internal Tide Generation over Mid-Atlantic Ridge Topography. *Journal of Physical Oceanography*, 39(10):2635–2651, 2009. ISSN 0022-3670. doi: 10.1175/2008JPO4136.1. URL `http://journals.ametsoc.org/doi/abs/10.1175/2008JPO4136.1`.

N. V. Zilberman, M. A. Merrifield, G. S. Carter, D. S. Luther, M. D. Levine, and T. J. Boyd. Incoherent nature of M 2 internal tides at the Hawaiian Ridge. *Journal of Physical Oceanography*, 41(11):2021–2036, 2011. ISSN 00223670. doi: 10.1175/JPO-D-10-05009.1.